UNIVERSITY
OF MICHIGAN
OCT 18 1950
ENGINEERING
LIBRARY

JOURNAL OF THE
AERONAUTICAL
SCIENCES

VOLUME 17 OCTOBER, 1950 NUMBER 10

CONTENTS

The Quasi-Steady Air Forces for Use in Low-Frequency Stability Calculations.... MARTIN GOLAND 601

A Method of Determining Some Aerodynamic Coefficients from Supersonic Free-Flight Tests of a Rolling Missile..... RAY E. BOLZ AND JOHN D. NICOLAIDES 609

Base Drag and Thick Trailing Edges..... SIGHARD F. HOERNER 622

Lateral-Control Devices Suitable for Use with Full-Span Flaps..... FRANCIS M. ROGALLO, JOHN G. LOWRY, AND JACK FISCHEL 629

An Initial Approach to the Overall Structural Problems of Swept Wings Under Static Loads..... E. E. SECHLER, M. L. WILLIAMS, AND Y. C. FUNG 639

Transient Loading of Supersonic Rectangular Airfoils..... JOHN W. MILES 647

The Gyroscopic Effect of a Rigid Rotating Propeller on Engine and Wing Vibration Modes..... R. H. SCANLAN AND JOHN C. TRUMAN 653

Approximate Solution of Compressible Fluid-Flow Problems by Galerkin's Method..... CHI-TEH WANG AND R. F. BRODSKY 660

Readers' Forum: "On Boundary-Layer Growth in a Compressible Flow Between Radial Walls," by J. Conrad Crown; "On Virtual Mass and Wave Drag at Subsonic Speeds," by John W. Miles; "Effect of Wing Parameters on Load Intensity in Wing Skin," by B. E. Gatewood; "The Basic Theorems in the Plastic Theory of Structures," by P. S. Symonds; "Note on Plastic Column Behavior," by George Gerard; "Some Relations Between Harmonic and Transient Loading of Airfoils," by John W. Miles..... 667–672

Published by the

INSTITUTE OF THE AERONAUTICAL SCIENCES, INC.

JOURNAL OF THE AERONAUTICAL SCIENCES

Editor: HUGH L. DRYDEN, *Director, N.A.C.A.*

Associate Editor: ROBERT R. DEXTER *Managing Editor:* BERNEICE H. JARCK

Editorial Committee

Aerodynamics

Francis Clauser
Howard Emmons
R. Paul Harrington
R. T. Jones
Carl Kaplan
W. B. Klemperer
John G. Lee
H. W. Liepmann
C. C. Lin
H. F. Ludloff
John R. Markham
Clark B. Millikan
Shatswell Ober
W. Bailey Oswald
Allen E. Puckett
Elliott G. Reid
H. J. F. Reid
Russell Robinson
G. B. Schubauer
W. R. Sears
John Stack
Th. von Kármán
Richard von Mises

Flight Testing

W. K. Ebel
R. R. Gilruth
Melvin N. Gough
Robert Stanley
E. G. Stout

Meteorology

C. F. Brooks
D. M. Little
E. J. Minser
F. W. Reichelderfer
H. C. Willett

Structures and Materials

W. B. Bleakney
E. W. Conlon
J. P. Den Hartog
L. H. Donnell
E. C. Hartmann
N. J. Hoff
E. E. Lundquist
C. F. Nagel, Jr.
J. S. Newell
Alfred S. Niles
W. Ramberg
E. Reissner
F. R. Shanley
H. W. Sibert
C. R. Strang
S. Timoshenko
H. S. Tsien
Chi-Teh Wang

Rotating Wing Aircraft

Robert Coleman
K. H. Hohenemser
Bartram Kelley
Ralph McClarren
R. H. Miller
R. H. Prewitt
Igor I. Sikorsky

Physiologic Problems

H. G. Armstrong
Louis H. Bauer
Eugene Du Bois
W. Randolph Lovelace, II
Ross A. MacFarland
A. D. Tuttle

Flight Propulsion

George W. Brady
Frank W. Caldwell
L. S. Hobbs
E. E. Johnson
Joseph Keenan
R. P. Kroon
Arthur Nutt
Hans Reissner
Abe Silverstein
C. Fayette Taylor
E. S. Taylor
P. Taylor
E. S. Thompson
H. S. Tsien

Aircraft Design

W. E. Beall
W. K. Ebel
Hall L. Hibbard
Richard Hutton
C. L. Johnson
I. M. Laddon
C. J. McCarthy
Fred E. Weick
Robert J. Woods

Air Transport

Charles Froesch
J. A. Herlihy
R. D. Kelly
Otto E. Kirchner
Jerome Lederer
John C. Leslie
R. Dixon Speas

Instruments

Allan G. Binnie
W. G. Brombacher
Charles H. Colvin
B. M. Craig
B. Del Mar
C. S. Draper
O. E. Esval
W. L. Howland
J. E. Lindberg
David W. Moore
George H. Purcell
W. A. Reichel
C. F. Savage
O. Hugo Schuck
C. L. Seward, Jr.
R. Sylvander
D. K. Warner
P. F. Weber

Vibration and Flutter

Lee Arnold
M. A. Biot
William Bollay
Chieh-Chien Chang
Martin Goland
J. P. Den Hartog

Fuels and Oils

D. P. Barnard
J. H. Doolittle
Graham Edgar
R. T. Goodwin
S. D. Heron
A. M. Rothrock

SUBSCRIPTION RATES

JOURNAL OF THE AERONAUTICAL SCIENCES, Published Monthly.—United States and Possessions: 1 Year, $12.00; Single Copies, $1.50. Foreign Countries Including Canada (American Currency Rate): 1 Year, $13.00; Single Copies, $1.50.

AERONAUTICAL ENGINEERING REVIEW, Published Monthly.—United States and Possessions: 1 Year, $3.00; Single Copies, $0.50. Foreign Countries Including Canada (American Currency Rates): 1 Year, $3.50; Single Copies, $0.50.

Notices of change of address should be sent to the Institute at least 30 days prior to actual change of address.

Manuscripts for publication, proofs, and all correspondence should be addressed to the Editorial Office of the JOURNAL.

Correspondence regarding subscriptions may be addressed to Publication Office, 20th and Northampton Sts., Easton, Pa., or to the Editorial Office of the JOURNAL OF THE AERONAUTICAL SCIENCES, 2 East 64th Street, New York 21, New York.

Copyright, 1950, by the Institute of the Aeronautical Sciences, Inc.

Entered as Second Class Matter at the Post Office, Easton, Pa., May 1, 1937. Acceptance for mailing at a special rate of Postage provided for in the Act of August 24, 1912. Authorized April 29, 1937.

JOURNAL OF THE AERONAUTICAL SCIENCES

VOLUME 17 OCTOBER, 1950 NUMBER 10

The Quasi-Steady Air Forces for Use in Low-Frequency Stability Calculations

MARTIN GOLAND*

Midwest Research Institute

SUMMARY

Simple, approximate expressions are derived for the air forces acting on an airfoil executing oscillatory motions with arbitrary damping. These expressions are in forms convenient for use in analyses of aircraft stability and response. The derivations are of a simple character, consisting merely of power series approximations for the known results from unsteady aerodynamic theory. It is shown that the present approach enables the evaluation of aircraft stability derivatives with better theoretical accuracy than do the methods now conventionally employed, while not appreciably increasing the labor associated with their use. In the present paper, detailed attention is concentrated on the determination of the stability derivatives for low-frequency motions; preliminary consideration is also given to methods for dealing with the higher frequency range.

INTRODUCTION

IN A RECENT STABILITY and response investigation of a special nature conducted by the author,† it was found that the value of the stability derivative $c_{m_{D\delta}}$, the total moment on the craft due to the elevator rotational velocity, entered into the analysis in a most critical fashion. In particular, if this derivative were assigned a negative value (presuming the usual N.A.C.A. sign conventions, to be given in detail later), the aircraft displayed a static divergence that is contrary to physical experience. Furthermore, the $c_{m_{D\delta}}$ calculated for the system by means of the techniques in current use, such as those described by Jones and Cohen[1] and White and Klampe,[2] *does* show such a negative value. This, of course, suggested that the conventional methods for calculating the $c_{m_{D\delta}}$ derivative might require some modification.

It readily became apparent that this is actually the case. This can be seen as follows: The total aircraft moment arising from motion of the elevator is, to a very good approximation, equal to the negative of the product of the tail length of the craft and the tail force due to elevator motion. The tail lift coefficient arising from elevator motions is given by White and Klampe[2] in their Eq. (21) as

$$m\frac{T_{10}}{\pi}\delta + \left[-T_4 + m\frac{T_{11}}{2\pi}\right]\frac{b}{v}\frac{d\delta}{dt} \qquad (1)$$

where m is the slope of the tail lift coefficient vs. angle of attack, and the various T terms are defined by Theodorsen.[3] Theodorsen points out in his Table 1 that both T_{10} and T_{11} are positive, while the value of T_4 is negative. Hence, for elevator oscillations of the type $e^{j\omega t}$, it follows from Eq. (1) that both the real and imaginary parts of the tail lift due to elevator motion are positive in value. This amounts to the statement that both c_{m_δ} and $c_{m_{D\delta}}$ are always negative.

The lift coefficient given by Eq. (1) is presumably an approximation of the coefficient calculated exactly by Theodorsen.[3] However, if Theodorsen's Eq. (XVIII) is used and if the lift coefficient due to elevator motion is computed for values $\omega b/v$ in the range from 0 to 0.1, which is of interest in stability problems, it is found that the real and imaginary parts of the coefficient have *opposite* signs, the real part being positive but the imaginary part having a *negative* value. This is confirmed by a glance at the table of oscillating airfoil coefficients published by Smilg and Wasserman;[4] at $v/b\omega$ values of 10 and 16.67, the real and imaginary parts of the co-

Received January 19, 1950. Revised and received April 3, 1950.

* Chairman, Engineering Mechanics Division.

† The study reported here was undertaken in connection with two research programs being sponsored by the Aircraft Laboratory, Air Materiel Command, U.S. Air Forces, Dayton, Ohio. The first of these deals with aircraft stability and is being done under the direction of the Aerodynamics Branch; the second is concerned with gust loads and is sponsored by the Structures Branch. Particular thanks is due Dr. G. W. Braun, W. Boccius, M. Shorr, and C. B. Westbrook, all of the Aircraft Laboratory, for their many suggestions and helpful advice during the course of the work.

efficient L_β are of opposite sign for all elevator configurations.

This contradiction between the signs of the imaginary parts of the lift coefficients calculated by the exact procedure and from Eq. (1) leads to the conclusion that Eq. (1) requires modification. Hence, the methods used to calculate $c_{m_{D\delta}}$ in such sources as references 1 and 2 are also in need of alteration.

The source of the discrepancy in Eq. (1) will now be explored, and a more suitable expression will be derived. It will further be shown that the procedures in current use for calculation of other stability derivatives should also be modified, and appropriate forms for these cases will also be given.

The Derivatives c_{L_δ} and $c_{LD\delta}$ for Low-Frequency Oscillations

It is instructive to continue consideration of the airfoil lift due to control surface motion on a more rigorous basis. Consideration is restricted here to configurations where the elevator has no aerodynamic balance. For an airfoil of semichord b and an infinite aspect ratio, Theodorsen,[3] in his Eq. (XVIII), finds the lift per unit span due to oscillation of the elevator to be

$$L_\delta = -\rho b^2 \left(v T_4 \frac{d\delta}{dt} + b\, T_1 \frac{d^2\delta}{dt^2} \right) + 2\pi\rho v b C \left(v \frac{T_{10}}{\pi} \delta + b \frac{T_{11}}{2\pi} \frac{d\delta}{dt} \right) \quad (2)$$

where δ represents the elevator deflection, positive for a depressed trailing edge; all other notations are taken directly from Theodorsen. Note that the elevator configuration determines the values of the various T parameters. By conversion from physical units of time to the dimensionless time τ, where

$$\tau = (v/b)t$$

Eq. (2) becomes

$$L_\delta = \rho v^2 b \left[-T_4 \dot{\delta} - T_1 \ddot{\delta} + 2\pi C \left(\frac{T_{10}}{\pi} \delta + \frac{T_{11}}{2\pi} \dot{\delta} \right) \right] \quad (3)$$

where a dot denotes differentiation with respect to τ. The term $2\pi C$ represents the slope of the lift coefficient vs. angle of attack for the airfoil under the dynamic conditions of oscillation; Theodorsen shows that C is, in general, a complex number and is a function of the dimensionless frequency $k = \omega b/v$, where ω is the frequency of oscillation in physical units.

It should be noted that expressions equivalent to Eq. (3), but for control surfaces with aerodynamic balance, are given by Theodorsen and Garrick.[5] This permits direct extension of the present analysis to cover such cases.

It follows from Eq. (3) that the lift coefficient for the airfoil section is the portion of the right-hand side of the expression contained within the brackets. For an elevator oscillation according to $e^{jk\tau}$, the lift coefficient per unit elevator deflection is

$$l_\delta = \left[k^2 T_1 - jkT_4 + 2\pi C \left(\frac{T_{10}}{\pi} + jk \frac{T_{11}}{2\pi} \right) \right] \quad (4)$$

The problem now is to arrive at a simplified form of Eq. (4), which is valid for low frequencies of oscillation —i.e., small values of k. In current practice, this is done by replacing $2\pi C$ by its value when $k = 0$, it then being equal to the steady-state lift coefficient vs. angle-of-attack slope m and by retaining terms in Eq. (4) which are of the order k. It is seen that this procedure leads to the Eq. (1) statement. It will now be shown, however, that this approach to the problem does not yield results that are entirely correct.

The most direct method for approximating Eq. (4) for low values of k would appear to be to expand the expression as a Taylor series about $k = 0$ and retain terms up to the order k. Thus,

$$l_\delta \approx (l_\delta)_0 + k\, (dl_\delta/dk)_0 \quad (5)$$

where the subscript zero denotes the value when $k = 0$. To attempt this, form the derivative

$$\frac{dl_\delta}{dk} = 2kT_1 - jT_4 + j\, 2\pi C \frac{T_{11}}{2\pi} + 2\pi \frac{dC}{dk} \times \left(\frac{T_{10}}{\pi} + jk \frac{T_{11}}{2\pi} \right) \quad (6)$$

The nature of the derivative dC/dk for the small values of k, and in particular when $k = 0$, has been studied by Heilenday and Rauscher.[6] For an airfoil of infinite aspect ratio they find that, for k small and positive,

$$\frac{dC}{dk} = \frac{dF}{dk} + j \frac{dG}{dk} = -\frac{\pi}{2} + j\,(1 + \ln k) \quad (7)$$

and this shows that *as k approaches zero, the imaginary part of dC/dk approaches minus infinity.*

This at once leads to the conclusion that a Taylor series expansion of l_δ about $k = 0$ is not permissible. Such an expansion about a point $k > 0$ is possible, but for the present purpose this procedure is subject to the great disadvantage that the air forces are not returned precisely to their steady-state values when $k = 0$.*

While the difficulty described above can never be overcome theoretically, it is possible to approach the problem of approximating l_δ in the following fashion. If the function G, the imaginary part of C, is approximated by a best-fit straight line in some small, arbitrary region of k around zero, then the slope of this line can be used as the value of dG/dk at $k = 0$. The

* The question of expansion about a point k different from zero is discussed further later in this paper.

straight-line fit of G should, as noted above, preferably return to the value zero when $k = 0$.

For example, Fig. 1 shows a plot of G vs. k for small values of the abscissa. Also shown are two straight-line fits of this curve, calculated by the method of least squares. The line of higher slope on the plot is based on a five-point calculation using values of k between 0 and 0.05 in steps of 0.01. The equation for this line is

$$G'_{0(0.01)0.05} = -2.922\,k \tag{8}$$

The second line is fitted by ten points in the region from 0 to 0.10 in steps of 0.01 and has the equation

$$G'_{0(0.01)0.1} = -2.086\,k \tag{9}$$

Based on this approach to the problem, the Taylor series expansion for l_δ, accurate to order k, is readily shown to be

$$l_\delta = \frac{T_{10}}{\pi}\left[m + 2\pi\left(\frac{dF}{dk}\right)_0 k\right] + jk \times \left(-T_4 + m\frac{T_{11}}{2\pi} + 2\pi\frac{dG'}{dk}\frac{T_{10}}{\pi}\right) \tag{10}$$

A comparison of Eqs. (10) and (1) shows that they differ by the last terms in each of the parentheses contained in the former equation.

It follows from Eq. (10) that the stability derivatives c_{L_δ} and $c_{L_{D\delta}}$ for harmonic oscillation are given by

$$c_{L_\delta} = \frac{T_{10}}{\pi}\left[m + 2\pi\left(\frac{dF}{dk}\right)_0 k\right] \tag{11}$$

$$c_{L_{D\delta}} = \left(-T_4 + m\frac{T_{11}}{2\pi} + 2\pi\frac{dG'}{dk}\frac{T_{10}}{\pi}\right) \tag{12}$$

It is shown in Appendix I that it is valid to use these derivatives for the case of either decaying or growing oscillatory motions, as well as harmonic motion, by permitting the value of the "frequency" k to be complex. Thus, c_{L_δ} and $c_{L_{D\delta}}$ are stability derivatives that entirely conform to the usual connotations. For complex values of k, Eq. (7) continues to hold, provided the real part of k is positive.*

As an example of the results obtained from Eqs. (11) and (12), Fig. 2 shows a plot of these derivatives as a function of k in the range from 0 to 0.10. An elevator with hinge line at the mid-chord is presumed, and the following coefficients, valid for an airfoil of infinite aspect ratio, are used:

$$(2\pi C)_0 = m = 2\pi, \quad (dF/dk)_0 = -\pi/2$$
$$dG'/dk = -2.922 \text{ from Eq. (8)}$$

Also shown in Fig. 2 are values of the derivatives as calculated exactly from Eq. (4) and as computed from

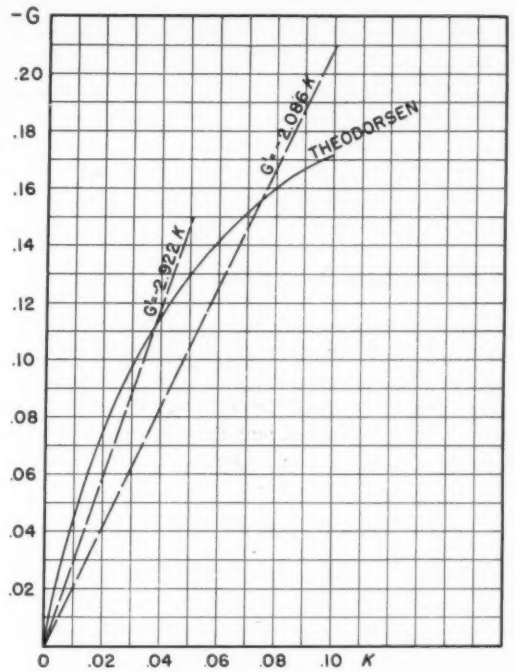

FIG. 1. The function G plotted vs. the nondimensional frequency k for the low-frequency range. Also shown are the straight-line curve-fits of Eqs. (8) and (9).

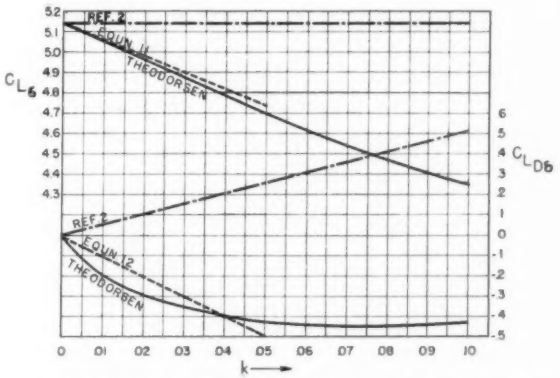

FIG. 2. The lift coefficient derivatives c_{L_δ} and $c_{L_{D\delta}}$ as a function of the nondimensional frequency k, calculated by three different methods. The coefficients refer to a control surface without aerodynamic balance and with hinge line at mid-chord.

Eq. (1). It is seen that the approximation suggested during the present analysis fits the exact results fairly well in the range where Eq. (8) is applicable.

The derivatives currently in conventional use are, however, not entirely correct. The c_{L_δ} from Eq. (1) fails to reflect a 10 per cent reduction as k goes from 0 to 0.05. Also, it is seen that the $c_{L_{D\delta}}$ from Eq. (1) shows severe discrepancies, both with regard to *sign and magnitude*. This same inaccuracy will be reflected in the value of the stability derivative $c_{m_{D\delta}}$.

Before concluding this section of the paper, it should be remarked that it is possible to approach the stability problem on a completely rigorous basis, making use of

* The need for stipulating that the real part of k must be positive if Eq. (7) is to hold arises from the fact that the slope of the function $F(k)$ is discontinuous at the origin. If the derivative dF/dk is formed by approaching the origin first from the left and then from the right, values of $+\pi/2$ and $-\pi/2$, respectively, are obtained.

the exact expressions for terms such as l_δ, given in this case by Eq. (4). The stability roots must then be extracted by iteration of the stability determinant, as was done by Goland and Luke[7] and Goland.[8,] * It is probable that the added accuracy achieved by this procedure, which is of a tedious nature, will be warranted only when studying aircraft of marginal stability where great precision of the results is required.

The Remaining Airfoil Section Derivatives

Proceeding in the same fashion as in the case of the $c_{L\delta}$ and $c_{L\dot{D}\delta}$ derivatives, it is a straightforward matter to derive the approximate forms for the various remaining airfoil section derivatives, accurate to the order k. In the development that follows, in addition to the use of the dimensionless time τ for reference, *all physical lengths are referred to the semichord b*. This causes physical velocities to be referred to the forward velocity v.

In addition, *physical forces are referred to the product $\rho v^2 b^2$; hence, physical moments, whether a total airfoil moment or a hinge-line moment, are referred to the product $\rho v^2 b^3$*. This reference procedure for forces and moments is somewhat at variance with usual stability practice but is particularly convenient for the present presentation.

The coordinates used to describe the motion of the airfoil are the same as those of Theodorsen but with slightly changed notation. Let γ be the *absolute, downward* velocity of the airfoil at a chordwise point located a distance a behind the mid-chord. The absolute airfoil rotation about the point a, positive in the nose-up sense, is written as θ. As before, the control surface deflection, positive for a depressed trailing edge, is δ. The instantaneous angle of attack of the airfoil is, then,

$$\alpha = \gamma + \theta \tag{13}$$

and it is to be noted that α is identical with the instantaneous downward velocity of the craft relative to a frame of axes fixed on the airplane.

As in the last section of the paper, a control surface without aerodynamic balance is presumed, so that the treatment of reference 3 applies. However, the analysis can readily be extended to cover cases with aerodynamic balance by utilizing the results in reference 5.

The remaining lift coefficient derivatives for the airfoil section are then found to be

$$c_{L_\gamma} = c_{L_{\dot\theta}} = m + 2\pi(dF/dk)_0\, k \tag{14}$$

$$c_{L_{D\gamma}} = \pi + 2\pi\,(dG'/dk) \tag{15}$$

$$c_{L_{D\theta}} = \pi + m[(1/2) - a] + 2\pi(dG'/dk) \tag{16}$$

The section derivatives for the airfoil moment coefficient, referred to the point a and positive for a nose-up moment, are obtained as

$$c_{m_\gamma} = c_{m_{\dot\theta}} = \left(a + \frac{1}{2}\right)\left[m + 2\pi\left(\frac{dF}{dk}\right)_0 k\right] \tag{17}$$

$$c_{m_{D\gamma}} = a\pi + [a + (1/2)]2\pi(dG'/dk) \tag{18}$$

$$c_{m_{D\theta}} = -\left(\frac{1}{2} - a\right)\pi + \left(\frac{1}{4} - a^2\right)m + \left(a + \frac{1}{2}\right)2\pi\frac{dG'}{dk} \tag{19}$$

$$c_{m_\delta} = -(T_4 + T_{10}) + \left(a + \frac{1}{2}\right)\frac{T_{10}}{\pi} \times \left[m + 2\pi\left(\frac{dF}{dk}\right)_0 k\right] \tag{20}$$

$$c_{m_{D\delta}} = -\left[T_1 - T_8 - (c - a)T_4 + \frac{1}{2}T_{11}\right] + \left(a + \frac{1}{2}\right)\left[m\frac{T_{11}}{2\pi} + 2\pi\frac{T_{10}}{\pi}\frac{dG'}{dk}\right] \tag{21}$$

The parameters c and the various T are defined in reference 3.

The section derivatives for the hinge-moment coefficient, positive for a moment that tends to depress the trailing edge, are found to be

$$c_{h_\gamma} = c_{h_{\dot\theta}} = -\frac{T_{12}}{2\pi}\left[m + 2\pi\left(\frac{dF}{dk}\right)_0 k\right] \tag{22}$$

$$c_{h_{D\gamma}} = T_1 - (T_{12}/2\pi)\,2\pi(dG'/dk) \tag{23}$$

$$c_{h_{D\theta}} = \left[2T_9 + T_1 - \left(a - \frac{1}{2}\right)T_4\right] - \frac{T_{12}}{2\pi}\left[\left(\frac{1}{2} - a\right)m + 2\pi\frac{dG'}{dk}\right] \tag{24}$$

$$c_{h_\theta} = -\frac{1}{\pi}(T_5 - T_4T_{10}) - \frac{T_{12}T_{10}}{2\pi^2}\left[m + 2\pi\left(\frac{dF}{dk}\right)_0 k\right] \tag{25}$$

$$c_{h_{D\delta}} = \frac{T_4T_{11}}{2\pi} - \frac{T_{12}}{2\pi}\left(\frac{T_{11}}{2\pi}m + \frac{T_{10}}{\pi}2\pi\frac{dG'}{dk}\right) \tag{26}$$

Figs. 3, 4, and 5 show plots of the exact values of various of the section derivatives, as well as the values obtained from Eqs. (14) through (26). These plots are for pitching of the section about its mid-chord axis and for a control surface hinged at the mid-chord. The value of dG'/dk used is that appropriate for $0 < k < 0.05$. The agreement between the exact and approximate values over this range is seen to be acceptable.

Also shown in the plots are the derivative values according to the treatment of reference 2. These are seen to show serious departures from the exactly calcu-

* The author takes this opportunity to point out an error that appeared in the manuscript of reference 8. Eq. (11) should read

$$w_h = \dot z + b\dot\theta = \lambda(z + b\theta)$$

and the succeeding development must be corrected accordingly. However, the calculations reported in reference 8 were carried out by means of the correct analysis and are, to the best of the author's knowledge, correct.

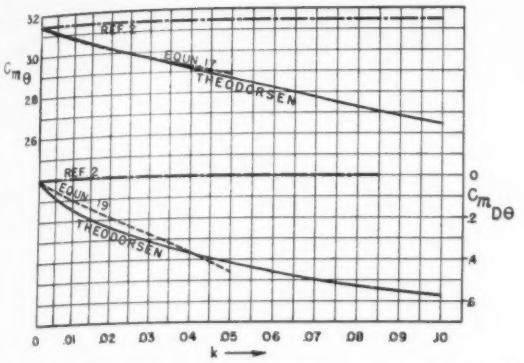

FIG. 3. Total airfoil moment coefficient derivatives c_{m_θ} and $c_{m_{D\theta}}$ as a function of the nondimensional frequency k, calculated by three different methods. The coefficients refer to the moment about the mid-chord, induced by rotation about the mid-chord.

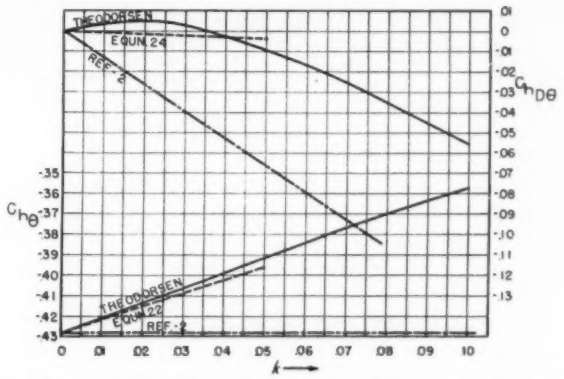

FIG. 4. Hinge-moment derivatives c_{h_θ} and $c_{h_{D\theta}}$ as a function of the nondimensional frequency k, calculated by three different methods. The coefficients refer to a control surface without aerodynamic balance and hinged at the mid-chord; the airfoil rotation is about the mid-chord.

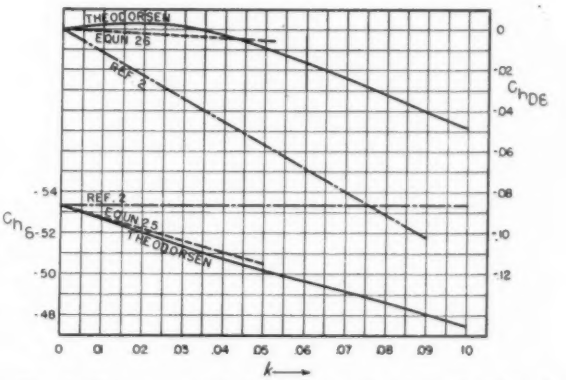

FIG. 5. Hinge-moment derivatives c_{h_δ} and $c_{h_{D\delta}}$ as a function of the nondimensional frequency k, calculated by three different methods. The coefficients refer to a control surface without aerodynamic balance and hinged at the mid-chord.

lated derivatives. The discrepancies in the hinge-moment derivatives are particularly severe.

THE DERIVATIVES FOR HIGHER VALUES OF k

Considering complex $k = \zeta e^{j\nu}$, Fig. 6 shows a plot of $C(k)$ vs. ζ (the absolute magnitude of k) for various values of the argument ν. The data for this plot are taken from a paper by Y. L. Luke and M. A. Dengler, both of the Midwest Research Institute, in which the behavior of $C(k)$ for complex k is comprehensively investigated; publication of this paper in the near future is contemplated. The important point to be gathered from an inspection of Fig. 6 is that, while a power series for $C(k)$ written about $k = 0$ may suffice for $0 < \zeta < 0.1$ (approximately), it cannot possibly afford acceptable accuracy when ζ falls outside of this region.

While the region $0 < \zeta < 0.1$ is generally sufficient to embrace all cases of stick-fixed stability and many cases of stick-free stability, modes of the latter type are sometimes encountered which involve values of ζ considerably above 0.1. The forms developed in this paper are evidently of no use for an analysis of such cases. The derivation of acceptable procedures for use in such instances entails great complexity and is presently under study.

One obvious approach is to expand $C(k)$ as a Taylor series about a point k different from zero; it is found that an expansion about $k = 0.4$ affords fairly good accuracy over a wide region of ζ above 0.2 and for practical values of ν. However, then the expansion is not about the point corresponding to the pseudostatic case, and this entails considerable practical disadvantage. Little can be said at this time about the problem of dealing with stability modes involving large ζ, except to point out the limitations of the present analysis.

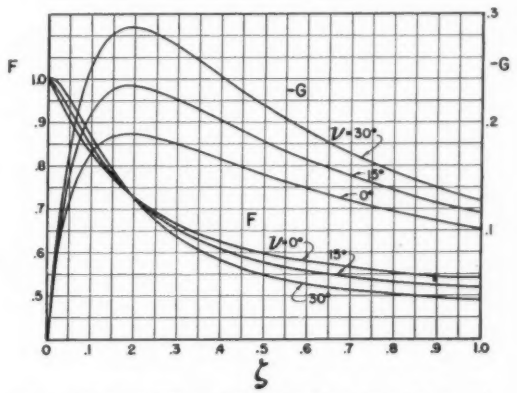

FIG. 6. Plot of $C(k)$ vs. k for complex values of $k = \zeta e^{j\nu}$.

THE DERIVATIVES FOR AIRFOILS OF FINITE SPAN

Up to the present, the development has been based on the Theodorsen analysis,[3] which presumes an airfoil of uniform chord and infinite aspect ratio. The question now arises as to what modification of these forms is required in order to make them applicable to airfoils of finite aspect ratio and with chord dimensions that vary along the span.

Consider first the spanwise distribution of the parameter m, the section lift coefficient vs. angle-of-attack

slope when $k = 0$. The problem of determining the spanwise variation of m is the same as that of computing the steady-state loading on airfoils of finite span. This problem is of a well-known character, and a variety of techniques, thoroughly described in the literature, are available for its solution.

With regard to the calculation of the spanwise distribution of the $F + jG$ function, however, a different situation exists. The problem is discussed by Reissner,[9] Reissner and Stevens,[10] and Wasserman,[11] and a further bibliography is contained in those papers. A study of these references shows that a precise treatment of the problem entails great complexity. Not only must the spanwise distribution of the $F + jG$ function be determined anew for each airfoil plan form and each frequency of oscillation, but the nature of this function also apparently depends on the character of the airfoil motion—i.e., whether it is of the γ, θ, or δ variety.*

Suppose, however, that a new function $f + jg$ is defined so that

$$f + jg = (2\pi F/m) + j(2\pi G/m) \tag{27}$$

where, it is recalled, both $F + jG$ and m refer to section coefficients of the airfoil. When $k = 0$, since $(2\pi F)_0 = m$ and $G = 0$, it is evident that the function $f + jg$ has the value unity across the entire span, regardless of the airfoil plan form; however, when k differs from zero, this function has values that, in general, vary across the span.

It will now be assumed, for the sake of conciseness in the present treatment, that for each value of k and for each airfoil plan form an *average value* of the function $f + jg$ can be deduced which can be taken to act across the entire span. Formal methods for arriving at this average $f + jg$ can be prescribed on the basis of treatments such as references 9 through 11, but these are of a relatively tedious nature.

Since for stability work the function $f + jg$ need be defined only for low values of k, it is highly probable that a convenient and concise procedure to permit its determination for a particular airfoil can be deduced. However, the answer to whether or not this is so must await the results of a further theoretical study. Actually, the parameters of interest to the present treatment are not the $f + jg$ directly but are the slopes $(df/dk)_0$ and dg'/dk, where g' has a definition analogous to the G' of Eqs. (8) and (9). It will be possible, in any event, to tabulate values of these slopes for airfoils with various standard plan forms, and interpolation can be used in the cases of airfoils with plan forms differing slightly from these.

In the absence of accurate values for the slopes, it is suggested that those appropriate to an airfoil of infinite aspect ratio be used—i.e., for the average function,

$$(df_{av.}/dk)_0 = f_{k0} = -\pi/2 \tag{28}$$

$$\left.\begin{aligned} \frac{dg_{av.}'}{dk} = g_k' &= -2.922; \quad 0 < k < 0.05 \\ &= -2.086; \quad 0 < k < 0.10 \end{aligned}\right\} \tag{29}$$

The chief error arising from the use of these values for airfoils of finite span is in the g_k' parameter, which should have smaller absolute values than those of Eq. (29).

Finite span corrections must also be applied to the apparent mass terms in Eqs. (11) through (26); these are the terms that have neither m nor $F + jG$ slopes attached. Adequate methods for determining these corrections are not available at present, at least in a form suitable for design-office calculations, and the use of the two-dimensional values appearing in the equations is therefore recommended.

The next question to be settled is that of determining the lift and moment coefficient derivatives for the complete airfoil. In order to account for airfoils with variable chord, it is necessary that a reference length for the entire system be established; this is generally taken as the mean aerodynamic semichord of the wing. However, any other reference length that affords greater convenience for a particular study can be chosen with equal facility. In the present treatment, this reference length is notated b_r.

All physical dimensions of the airfoil are then referred to b_r; all physical times, to v/b_r; all physical forces, to $\rho v^2 b_r^2$; and all physical moments, to $\rho v^2 b_r^3$. The nondimensional frequency parameter that describes the motion of the system is, then,

$$k_r = \omega b_r/v$$

In the b_r system, let y be a spanwise coordinate with its origin at the wing root; let b' be the semichord at station y, so that $b' = b/b_r$; and let $2l$ be the wing span. The local frequency parameter k at station y is then equal to

$$k = b'k_r \tag{30}$$

Consider now the wing lift due to a displacement in the coordinate γ—i.e., a vertical translation of the entire wing. The wing lift per unit span at station y is first obtained from Eqs. (14) and (15). Recalling that the section derivatives in Eqs. (11) through (26) are nondimensionalized in terms of the *local* semichord b, the wing lift per unit span in physical coordinates is

$$\rho v^2 b \left[c_{L_\gamma}\gamma + c_{L_{\dot{\gamma}}}(d\gamma/d\tau)\right] \tag{31}$$

and, hence, in the b_r system the wing lift per unit span is

$$b'\left[c_{L_\gamma}\gamma + b' c_{L_{\dot{\gamma}}}(d\gamma/d\tau_r)\right] \tag{32}$$

The total wing lift is, then,

$$\int_{-l}^{l} \left[b' c_{L_\gamma}\gamma + (b')^2 c_{L_{\dot{\gamma}}}\dot{\gamma}\right] dy \tag{33}$$

* The present discussion does not touch on the effects of compressibility, which add further severe complications to an understanding of the unsteady aerodynamic mechanisms.

where a dot now denotes a derivative with respect to time in the b_r system.

The lift coefficient derivatives for the entire wing are thus seen to be

$$K_{L_\gamma} = \int_{-l}^{l} b' c_{L_\gamma} dy \tag{34}$$

$$K_{L_{D\gamma}} = \int_{-l}^{l} (b')^2 c_{L_{D\gamma}} dy \tag{35}$$

Consider next the airfoil lift derivatives with respect to rigid body pitch of the entire surface (θ) and with respect to symmetrical operation of the control surfaces (δ). Both of these derivatives are of interest in longitudinal stability calculations. It follows that these derivatives are given by expressions identical with Eqs. (34) and (35), save that the subscript γ is replaced by the subscripts θ and δ, respectively.

If use is now made of Eqs. (11) through (16), it can be shown that

$$K_{L_\gamma} = \int_{-l}^{l} mb'\, dy + k_r f_{k0} \int_{-l}^{l} m(b')^2\, dy \tag{36}$$

$$K_{L_{D\gamma}} = \int_{-l}^{l} [\pi + m g_k'] \, (b')^2\, dy \tag{37}$$

and analogous results follow for the θ and δ airfoil derivatives.

In the case of the airfoil moment coefficient derivatives, proceeding in the same fashion as for the lift derivatives, it is readily shown that

$$K_{m_\gamma} = \int_{-l}^{l} (b')^2 c_{m_\gamma} dy \tag{38}$$

$$K_{m_{D\gamma}} = \int_{-l}^{l} (b')^3 c_{m_{D\gamma}} dy \tag{39}$$

and once again, if the subscript γ is replaced by θ and δ in these equations, expressions for the remaining longitudinal airfoil moment derivatives result. The section derivatives of interest in these definitions are given by Eqs. (17) through (21). It then follows, for example, that

$$K_{m_\gamma} = \int_{-l}^{l} [a + (1/2)] m (b')^2\, dy + k_r f_{k0} \int_{-l}^{l} [a + (1/2)] m (b')^3\, dy \tag{40}$$

$$K_{m_{D\gamma}} = \int_{-l}^{l} \{a\pi + [a + (1/2)] m g_k'\} \, (b')^3\, dy \tag{41}$$

Finally, recalling that hinge-moments are nondimensionalized by $\rho v^2 b_r^3$, it is seen that

$$K_{h_\gamma} = \int_{-l}^{l} (b')^2 c_{h_\gamma} dy \tag{42}$$

$$K_{h_{D\gamma}} = \int_{-l}^{l} (b')^3 c_{h_{D\gamma}} dy \tag{43}$$

with analogous results for the remaining hinge-moment derivatives. The pertinent section derivatives are given by Eqs. (22) through (26).

While attention has thus far been concentrated on the airfoil derivatives that enter into longitudinal stability calculations, it is evident that the lateral stability derivatives can be compounded with equal facility. The procedures used for their derivation are directly analogous to those employed in the longitudinal cases. Thus, for example, the derivative for the airfoil rolling moment due to rate of roll $\dot{\phi}$, with all units in the b_r system, is found to be

$$K_{R_{\dot{\phi}}} = -2 \int_0^l y c_{L_\gamma} b'\, dy \tag{44}$$

and also

$$K_{R_{D\dot{\phi}}} = -2 \int_0^l y c_{L_{D\gamma}} (b')^2\, dy \tag{45}$$

The spanwise distribution of m and the slopes f_{k0} and g_k' used for the calculation of the section derivatives must, of course, be appropriate for the rolling motion.

In the stability equations for an aircraft, the forces and moments on both the wing and tail surfaces appear; these must be nondimensionalized according to a scheme consistent for the entire aircraft system. If the semichord b' and the spanwise coordinate y for both wing and tail are referenced to the same b_r (usually one-half the wing mean aerodynamic chord), all such considerations are automatically taken care of.

Conclusions

It is a natural conclusion of the present study that all stability derivatives should be based on the treatment outlined here, rather than on the procedures reported in the past literature. At the same time, it is important to note that the use of the more correct derivatives proposed in this paper does not increase the degree of complexity required to carry out a stability solution over current levels.

Wherever possible, of course, stability derivatives should be evaluated by accurate prototype or model testing; in the usual instance, only the pseudostatic ($k = 0$) values of the derivatives can be conveniently determined in this manner. These pseudostatic values must then be extrapolated to the case of unsteady motion by the methods described in this paper. For example, a static wind-tunnel test would provide the value of K_{h_γ} at $k = 0$; according to Eqs. (42) and (22) this value is

$$(K_{h_\gamma})_0 = -\int_{-l}^{l} \frac{T_{12}}{2\pi} m\, (b')^2\, dy \tag{46}$$

and the value of the derivative when k_r is not zero must then be taken as

$$K_{h_\gamma} = (K_{h_\gamma})_0 - k_r f_{k0} \int_{-l}^{l} \frac{T_{12}}{2\pi} m\, (b')^3\, dy \tag{47}$$

As a final remark, it is of interest to note that certain of the findings in this paper were anticipated in prior studies conducted by Gruschwitz,[12] Söhngen,[13] and Smilg.[14] These authors point out that the stability derivatives in conventional use do not adequately describe the aerodynamic damping present in the system. They also point out that the negative damping predicted by the Theodorsen derivatives for certain oscillation conditions will probably account for the lateral "snaking" phenomenon encountered in some aircraft designs. The work of Gruschwitz is of further interest in that he brings out the unusual behavior of the damping derivatives called for by the Theodorsen theory as the pseudostatic condition is approached; it is shown here that this is associated with the infinite value of the slope of the G vs. k curve as the frequency k approaches zero.

References

[1] Jones, R. T., and Cohen, D., *An Analysis of the Stability of an Airplane with Free Controls*, N.A.C.A. Report No. 709, 1941.

[2] White, R. J., and Klampe, G., *Force and Moment Coefficients for a Thin Airfoil with Flap and Tab in a Form Useful for Stability and Control Calculations*, N.A.C.A. T.N. No. 960, 1945.

[3] Theodorsen, T., *General Theory of Aerodynamic Instability and the Mechanism of Flutter*, N.A.C.A. Report No. 496, 1935.

[4] Smilg, B., and Wasserman, L. S., *Application of Three-Dimensional Flutter Theory to Aircraft Structures*, Technical Report No. 4798, Air Materiel Command, U.S. Air Forces, Dayton, Ohio, July, 1942.

[5] Theodorsen, T., and Garrick, I. E., *Nonstationary Flow About a Wing-Aileron-Tab Combination Including Aerodynamic Balance*, N.A.C.A. Report No. 736, 1942.

[6] Heilenday, F., Jr., and Rauscher, M., *Theoretical and Experimental Methods of Flutter Analysis; Vol. VI*, Contract No. NO a(s)8790, Massachusetts Institute of Technology, Cambridge, Mass., June, 1949.

[7] Goland, M., and Luke, Y. L., *A Study of the Bending-Torsion Aeroelastic Modes for Aircraft Wings*, Journal of the Aeronautical Sciences, Vol. 16, No. 7, p. 389, July, 1949.

[8] Goland, M., *Stick-Fixed, Short-Period Stability Based on the Wagner Air Forces*, Reissner Anniversary Volume: Contributions to Applied Mechanics; J. W. Edwards, Ann Arbor, Mich., 1949.

[9] Reissner, E., *Effect of Finite Span on the Airload Distributions for Oscillating Wings; Part I—Aerodynamic Theory of Oscillating Wings of Finite Span*, N.A.C.A. T.N. No. 1194, 1947.

[10] Reissner, E., and Stevens, J. E., *Effect of Finite Span on the Airload Distributions for Oscillating Wings; Part II—Methods of Calculation and Examples of Application*, N.A.C.A. T.N. No. 1195, 1947.

[11] Wasserman, L. S., *Aspect Ratio Corrections in Flutter Analysis*, Memorandum Report MCREXA5-4595-8-5, Air Materiel Command, U.S. Air Force, Dayton, Ohio, August, 1948.

[12] Gruschwitz, E., *Die für die Richtungsstabilität eines Flugzeuges mit losem Seitenruder massgebenden Luftkräfte bei Berücksichtigung instationärer Strömung*, Report No. 143, Lillienthal-Gesellschaft für Luftfahrtforschung, November, 1941.

[13] Söhngen, H., *Zur Frage der Lösung der flugmechanischen Bewegungsgleichen bei instationären Luftkraftansätzen*, Report No. 143, Lillienthal-Gesellschaft für Luftfahrtforschung, November, 1941.

[14] Smilg, B., *The Instability of Pitching Oscillations of an Airfoil in Subsonic Incompressible Potential Flow*, Journal of the Aeronautical Sciences, Vol. 16, No. 11, p. 691, November, 1949.

[15] Carslaw, H. S., and Jaeger, J. C., *Operational Methods in Applied Mathematics*, Oxford University Press, London, England, 1941.

Appendix I

The Steady-State Air Forces Induced by Oscillatory Nonharmonic Airfoil Motions

The airfoil motions to be considered here are those that proceed according to the schedule $e^{j\lambda\tau}$, where

$$\lambda = k - j\xi \tag{A1}$$

and where, by definition, both k and ξ are real quantities. The motions are seen to be oscillatory with a nondimensional frequency k, but they are nonharmonic when ξ is different from zero. A negative value for ξ defines a stable motion (amplitude decreasing with time), while a positive ξ implies unstable oscillations. The natural oscillatory motions of an aircraft may be stable, neutrally stable, or divergent; hence, a stability analysis of the system must employ a statement of the air forces which is capable of embracing all three such types of motion.

In the body of this paper, a study is made of the *steady-state* air forces induced by sinusoidal motions of the airfoil. The term *steady state* is used to denote the fact that only those components of the air forces are considered which, like the motion of the airfoil, proceed according to the schedule $e^{jk\tau}$. Physically, this has the implication that the air forces are dealt with after the wake is infinitely long and after the effects of aerodynamic starting transients are no longer present.

These steady-state air forces are, of course, shown to be a function of the frequency k. It will now be shown that, by the simple replacement of k by the parameter λ of Eq. (A1), the harmonic air-force statements become applicable to cases of nonharmonic oscillatory motions.

Consider motions of the airfoil which are defined by a particular time history of the displacement coordinate $x(\tau)$; this coordinate may be a translational velocity, the angle of attack, the control surface displacement, or the like. Furthermore, let $\kappa(\tau)$ represent the *circulatory* air forces that arise from a unit step-function displacement of the coordinate x, starting when $\tau = 0$ (this is the *indicial admittance* of the circulatory system). Then, by Duhamel's integral, it follows that the circulatory air forces $F(\tau)$ arising from the motion $x(\tau)$ are

$$F(\tau) = [\kappa(\tau)]x(0) + \int_0^\tau [\kappa(\tau - s)]\left[\frac{d}{ds}\, x(s)\right] ds \tag{A2}$$

For the motion $x(\tau) = e^{j\lambda\tau}$, Eq. (A2) becomes

$$F(\tau) = \kappa(\tau) + j\lambda \int_0^\tau [\kappa(\tau - s)]e^{j\lambda s}\, ds \tag{A3}$$

(Continued on page 672)

A Method of Determining Some Aerodynamic Coefficients from Supersonic Free-Flight Tests of a Rolling Missile*

RAY E. BOLZ† AND JOHN D. NICOLAIDES‡

Case Institute of Technology and Ballistic Research Laboratories

ABSTRACT

Based on the assumption that the aerodynamic forces acting at any point on a lifting surface are linearly dependent upon the local angle of attack at that point, the theory of pure rolling motion is applied to the experimentally observed motion of a finned missile in supersonic flight in order to (1) determine how well the actual motion is represented by the theory; (2) determine the suitability of the Aerodynamic Range at the Ballistic Research Laboratory, Aberdeen, Md., to the proposed free-flight roll technique; and (3) determine certain aerodynamic coefficients associated with the motion over a range of Mach Numbers from 1.67 to 2.7. Values for the aerodynamic coefficients are also derived using the linearized supersonic theory and are compared with those obtained from experiment.

The results indicate that the actual motion is well represented by the theory to within the small experimental errors and that excellent reproducibility of the aerodynamic coefficients in roll is obtained. Furthermore, the results show a fairly good correlation with the linearized theory when applied to aerodynamic surfaces of 16 per cent thickness as employed on the missiles used in the reported tests.

INTRODUCTION

IN THE PAST, the activities of the exterior ballistician and those of the aerodynamicist have been widely separated. The ballistician was primarily interested in wingless and finless spinning bodies of revolution traveling at supersonic speeds, and the aerodynamicist was interested in subsonic aircraft whose primary elements were the lifting surfaces. However, in recent years, a change has taken place—the ballistician is now equipping his bodies of revolution with wings and/or fins and calling them missiles, and the aerodynamicist has vigorously extended his field of interest and activity into the supersonic régime, with the consequent application to supersonic aircraft and guided missiles. The two fields have thus merged and the ballistic and aerodynamics people can mutually contribute and benefit from their respective work and tools.

One of the experimental tools developed by the exterior ballistician appeared particularly applicable to the general field of experimental aerodynamics—namely, the Free-Flight Range at the Ballistic Research Laboratory, Aberdeen, Md., under the direction of Dr. A. C. Charters.[1, 2] In order to explore a particular phase of this applicability, the authors, with the willing consent and cooperation of Charters, several years ago embarked upon an experimental program in the Aerodynamic Free-Flight Range to evaluate the usefulness of the equipment for accurately yielding not only static but more important *dynamic* force and moment coefficients associated with given winged and/or finned aerodynamic configurations in supersonic flight.

The general experimental technique is: The motion of the missile is determined by measurements taken from successive photographs of a configuration during free-flight down the range. The integrated equations of motion are then "fitted" to the measurements by a least squares procedure, and the constants of the final equation yield the experimental values of the aerodynamic coefficients. The accuracy of the procedure then depends upon the validity of the equations of motion, and a correct theory must necessarily result in a final equation that fits the measurements within the experimental error.

The first project in the overall program is presented in this report, wherein a simple motion—namely, that of pure roll—is imposed on the missile and the theory of pure rolling motion is applied to the experimentally observed motion in order to obtain the associated aerodynamic coefficients. The fit of the equation of rolling motion to the range data is obtained, and a comparison is made of the experimentally obtained coefficients, one static C_{l_δ} and one dynamic C_{l_p}, to those predicted by a linearized theory.

It is not intended that this paper present the results of a finished research program. However, it does include the basic theory of motion, the specific range-test technique adopted, the method of data reduction, some specific results over a series of Mach Numbers, the experimental accuracy and reproducibility of the tests, and the overall evaluation of the range as applied to the technique devised.

Presented at the Aerodynamics Session, Eighteenth Annual Meeting, I.A.S., New York, January 23–26, 1950.

* Part of the material presented in this paper appeared in the experimental section of a Doctoral Dissertation for Yale University (June, 1949) by Ray E. Bolz. The authors wish to acknowledge the contributions of Dr. A. C. Charters to the general program and the assistance of Miss Karolyn Skegas in the reduction of the data.

† Associate Professor of Aeronautical Engineering.

‡ Aerodynamicist, Free-Flight Aerodynamics Branch.

This paper includes the material presented in reference 3, with additional test data at the higher Mach Numbers.

Symbols

a	= radius of body of missile
A_p	= area of fin or wing panel (see Fig. 1)
$A, B, \ldots$	= arbitrary constants depending on boundary conditions
b	= wing span
B	= $\sqrt{M^2 - 1}$
c	= wing chord
C_1	= damping constant $[(K_{l_p}/I) - (K_R/m)]$
C_2	= K_{l_δ}/I
C_D	= drag coefficient
C_{l_δ}	= roll moment derivative due to canted surface, $(\partial C_l/\partial\delta)$, δ in rad.
C_{l_p}	= roll moment derivative due to rolling velocity, $\partial C_l/\partial(pb/2V)$
C_l	= roll moment coefficient, L/qA_pb
d	= diameter of body
$\left(\frac{dC_L}{d\alpha}\right)_{x,y}$	= slope of the lift curve at any point x, y on fin
K_{l_δ}	= L_δ/V^2
K_{l_p}	= L_p/pV
K_R	= $(\rho/2)\,SC_D$
L_δ	= rolling moment due to angle of cant
L_p	= rolling moment due to rolling velocity, damping moment
I	= axial moment of inertia (slugs-ft.^{2})
M	= Mach Number
m	= mass (slugs)
n_δ	= number of canted fins
n	= total number of fins
p	= rolling velocity ($\dot{\phi}$), rad. per sec.
p_s	= steady-state rolling velocity $(\dot{\phi})_\infty$, rad. per sec.
P.E.	= probable error
$pb/2V$	= fin-tip helix angle
$p_sb/2V$	= steady-state fin-tip helix angle
S	= $(\pi/4)d^2$
s	= steady-state rolling velocity (deg. per ft.)
V	= linear velocity of missile along trajectory (ft. per sec.)
x, y	= Cartesian coordinates: y along fin span; x along fin chord
z	= linear distance along the free-flight range
α	= angle of attack
δ	= angle of cant on one fin
β	= tip Mach cone angle
μ, r	= polar coordinates shown in Fig. 3
ρ	= free-stream air density, slugs per cu.ft.
ϕ	= angle of roll
Ω	= $s - \phi'$

Superscripts

Dot over symbol is time derivative of variable

Prime mark is the derivative with respect to z, distance along range

General Experimental Technique

A suitable aerodynamic test vehicle is gun-launched down the Aerodynamic Free-Flight Range. The special firing technique employed results in small pitching and yawing displacements of the test vehicle during the subsequent flight. This vehicle may be a model of any aerodynamically stable missile configuration having one or more pairs of fins set at a differential angle of incidence (cant) to induce a rolling velocity. During flight, as it passes each of 25 stations accurately located along a 218-ft. distance, the missile is photographed (shadowgraphs) simultaneously in the vertical and horizontal planes by means of an extremely short duration spark discharge. The time of occurrence of the discharge for nine of the stations is measured to within 10^{-6} sec. From the photographs, the spatial orientation of the missile is obtained, from which the linear displacements (to 0.001-ft. accuracy) and angular displacements in roll (to $\pm 0.7°$ accuracy) are determined at the 25 discrete distances along the trajectory as well as at nine discrete values of time.

With these data obtained from the aerodynamic range and the analyses in the following sections, the aerodynamic coefficients associated with the rolling motion may be determined and compared with the theoretical values calculated on the basis of linearized supersonic theory.

Theory

(A) *Equation of Motion of a Missile in Pure Roll*

If a symmetrical winged and/or finned missile with canted surfaces is in free flight and has an angular motion of pure roll (yawing and pitching displacements negligible), the missile may be considered as being acted upon by two roll moments. One moment, tending to increase the roll velocity, results from the lift-force couple produced by the canted surfaces in linear forward motion; the second moment, tending to decrease the roll velocity, is the damping moment produced by the lift-force couples induced on all the aerodynamic surfaces by the roll velocity itself.

(1) *Roll Moment Due to Canted Fins.*—The roll moment induced by n_δ differentially offset (canted) wing or tail panels may be expressed as the integral

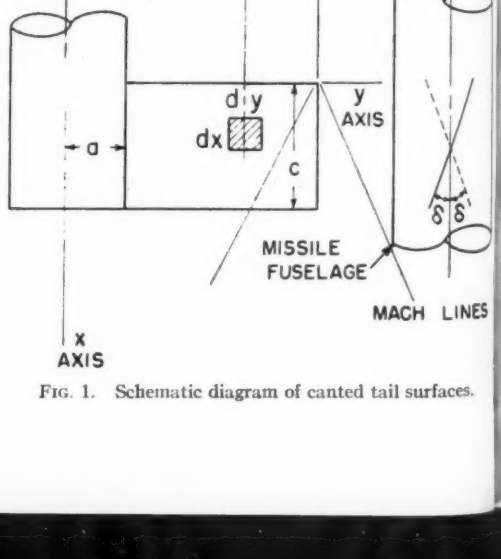

Fig. 1. Schematic diagram of canted tail surfaces.

product of the aerodynamic lift force and the moment arm of this force about the missile axis. Consequently, from Fig. 1,

$$L_\delta = \frac{n_\delta \rho V^2}{2} \int_{x=0}^{c} \int_{y=a}^{b/2} \left(\frac{dC_L}{d\alpha}\right)_{x,y} y\delta \, dx \, dy \qquad (1)$$

$$L_\delta = K_{l_\delta} V^2 \qquad (2)$$

(2) Roll Moment Due to Rolling Velocity, Damping Moment.—When a missile rolls about its own axis, the lifting surfaces are subjected to a normal velocity vector induced by the rolling velocity. The induced velocity results in an induced angle of attack on the surface which varies over the surface as a linear function of the radial distance from the rotational axis. If the roll damping moment, neglecting the viscous damping on the fuselage,* is defined as the roll moment induced by and opposing or damping the rolling velocity, then this aerodynamic damping moment (with reference to Figs. 1 and 2) may be expressed by a double integration as follows:

$$L_p = pV \frac{\rho_n}{2} \int_{x=0}^{c} \int_{y=a}^{b/2} \left(\frac{dC_L}{d\alpha}\right)_{x,y} y^2 \, dx \, dy \qquad (3)$$

or

$$L_p = K_{l_p} pV \qquad (4)$$

(3) Dynamical Equation of Roll.—Applied to a symmetrical missile in pure rolling flight, subject to small pitching and yawing displacements, the dynamical equation in roll becomes, simply,

$$I\ddot{\phi} = L_\delta - L_p \qquad (5)$$

Here, the rolling moments exerted by the wing and tail surfaces arising from the pitching and yawing angular displacements and angular velocities have been neglected because (1) for small pitching and yawing displacements (mean square yaw less than 1.5°) these moments are extremely small and of second order compared with L_δ and L_p (see Appendix I) and (2) they are oscillatory with respect to their direction of action and, as such, any small effect that they may otherwise exert on the resulting rolling motion tends to cancel out.

(B) *Solution of Dynamical Equation of Roll*

For the missiles traveling the length of the range between stations (218 ft.), the decrease in velocity is less than 7 per cent, and, for values of flight Mach Number in excess of 1.6, the variation of $dC_L/d\alpha$, the slope of the lift curve, resulting from this small deceleration is less than about $3^1/_2$ per cent from the average value. Therefore, little error is introduced if the values of

* The effect of viscous damping of a missile fuselage may be estimated from the performance of spinning bodies of revolution as determined in the aerodynamic range. The numerical value of the viscous damping coefficient of our missile is approximately 0.16 per cent of the aerodynamic damping coefficient obtained. Consequently, the effect of body damping may then be neglected for the purposes of this report.

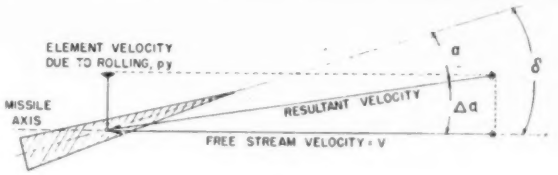

$$\Delta\alpha = \frac{py}{V}$$

FIG. 2. Cross-sectional view of a canted tail surface at a given span location showing the effect of rolling velocity.

K_{l_p} and K_{l_δ} in Eqs. (2) and (4) are considered as constant for any given flight.

Insertion of Eqs. (2) and (4) into Eq. (5) gives

$$I\ddot{\phi} + K_{l_p} \dot{\phi} V = K_{l_\delta} V^2 \qquad (6)$$

where

$$K_{l_\delta} = \frac{\rho n_\delta}{2} \int_{x=0}^{c} \int_{y=a}^{b/2} \left(\frac{dC_L}{d\alpha}\right)_{x,y} y\delta \, dx \, dy \qquad (7)$$

$$K_{l_p} = \frac{\rho n}{2} \int_{0}^{c} \int_{y=a}^{b/2} \left(\frac{dC_L}{d\alpha}\right)_{x,y} y^2 \, dx \, dy \qquad (8)$$

and $\dot{\phi} = d\phi/dt = p$, the rolling velocity.

The approximate linear equation of motion of the missile along the trajectory may be written

$$m\dot{V} = -K_R V^2 \qquad (9a)$$

where

$$K_R = (\rho/2)\, SC_D \qquad (9b)$$

is considered constant for the small variation in velocity V.

Eqs. (6) and (9) are now transformed to the independent variable, z, the horizontal distance along the range, by

$$\left.\begin{aligned} \frac{d}{dt} &= \frac{dz}{dt}\frac{d}{dz} = V\frac{d}{dz} \\ \frac{d^2}{dt^2} &= V^2\frac{d^2}{dz^2} + V\frac{dv}{dz}\frac{d}{dz} \end{aligned}\right\} \qquad (10)$$

This transformation as written is valid, since in the range the distance along the trajectory may be assumed equal to the distance along the range and the missile velocity becomes $V \cong dz/dt$, with negligible error. If a prime is used to denote a derivative with respect to z, then Eqs. (6) and (9a) become

$$\phi'' + \phi'\left(\frac{V'}{V} + \frac{K_{l_p}}{I}\right) - \frac{K_{l_\delta}}{I} = 0 \qquad (11)$$

and

$$V'/V = -K_R/m \qquad (12)$$

Substitution of Eq. (12) into Eq. (11) gives

$$\phi'' + \phi'\left(\frac{K_{l_p}}{I} - \frac{K_R}{m}\right) - \frac{K_{l_\delta}}{I} = 0 \qquad (13)$$

a linear differential equation with constant coefficients.

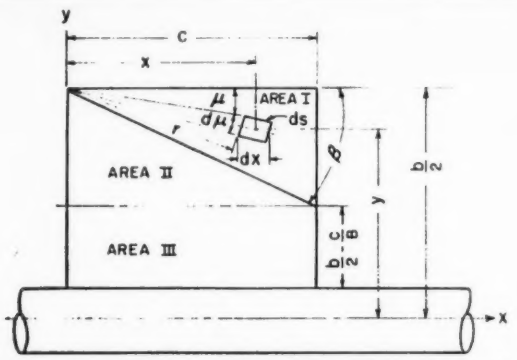

FIG. 3. Schematic view of tail surface illustrating integration procedure.

Defining

$$C_1 = (K_{l_p}/I) - (K_R/m) \tag{13a}$$

$$C_2 = K_{l_\delta}/I \tag{13b}$$

Eq. (13) becomes

$$\phi'' + C_1\phi' - C_2 = 0 \tag{14}$$

The general solution of Eq. (14) may be written immediately as

$$\phi = B + sz + Ae^{-C_1 z} \tag{15}$$

where

$$s = C_2/C_1 \tag{16}$$

steady-state rolling velocity.

A and B are arbitrary constants that depend upon the boundary conditions. A curve given by Eq. (15) relating the missile roll angle and the distance along the trajectory is fitted to the data points by means of the method of differential corrections. The process of "fitting" then results in a determination of the roll constants C_1 and C_2 (and therefore the constants K_{l_p} and K_{l_δ}).

Thus the damping and rolling moments can be experimentally determined as a function of missile design and Mach Number.

(C) *Theoretical Determination of the Roll-Moment Coefficients*

The values for K_{l_p} and K_{l_δ} defined in Eqs. (7) and (8) are determined experimentally in the aerodynamic range by the technique discussed in this paper. However, approximate values for these two coefficients may also be determined theoretically from the application of the existing linearized supersonic theory.

The theory as applied here assumes the two-dimensional value of $dC_L/d\alpha$ in the areas of the fins outside the tip region for the calculation of K_{l_p} and K_{l_δ}. This assumption, of course, cannot give the exact theoretical lift distribution on the wing within the Mach cone originating from the intersection of the wing leading edge with the body. However, since this region (where the lift distribution is only approximately calculated because of the neglect of the body-wing juncture interference effect) is close to the body, the resultant error in the theoretical rolling moments should be small.

The effects of body upwash on wing lift when the body is at an angle of yaw have also been neglected. However, in the roll tests in the aerodynamic range, it should be noted that yaw during flight down the range is always intentionally restricted by the launching technique to an extremely small angle (mean square yaw less then 1.5°) in order for the roll Eq. (6) to be nearly exact. Any upwash on the wing resulting from the yawed body would result in (1) small symmetrical forces (lift forces in the same direction on both halves of the fin) when the fins are oriented at 0° or 45° to the plane of yaw, and (2) possibly *very small* unsymmetrical forces due only to flow dissimilarities when the missile is oriented in roll to any angle, other than those stated above, referred again to the plane of yaw. Since a roll moment can obviously arise only from the unsymmetrical forces, it may be concluded from the qualitative observations above that any roll moments resulting from body upwash phenomena would not only be small moments but would be rapidly oscillating in sign as well as in magnitude. Such moments would contribute negligible effect to the rolling motion of the missile resulting from the relatively large and continuously directed moments, L_p and L_δ.

One further point may be noted—namely, that the forces on the cone-cylinder fuselage cannot contribute to a rolling moment other than the negligible viscous damping moment already mentioned.

(*1*) *Determination of K_{l_p} from the Linearized Supersonic Theory.*—From the linearized two-dimensional theory of Ackeret,[4] the value of the lift slope at all points on the surface of an infinite-aspect-ratio lifting surface is given by the expression

$$\left(\frac{dC_L}{d\alpha}\right)_{x,y} = \frac{4}{\sqrt{M^2 - 1}} = \frac{4}{B} \tag{17}$$

which is a function of Mach Number only. However for a finite wing or tail surface, the pressure distribution over the lifting surface included within the tip Mach cone is influenced by the wing-tip boundary conditions as well as by the variable angle of attack (py/V helix angle) induced over the surface by the rolling velocity.

This pressure distribution is evaluated on the basis of the three-dimensional linearized supersonic theory of reference 5. The value, then, for $(dC_L/d\alpha)_{x,y}$ for an incremental area on a rectangular wing within the tip Mach cone boundary is

$$\left(\frac{dC_L}{d\alpha}\right)_{x,y} = \frac{8}{\pi B}\left[\sin^{-1}\sqrt{\frac{B}{x}\left(\frac{b}{2}-y\right)} - \frac{1}{y}\sqrt{\left(\frac{b}{2}-y\right)\left(y-\frac{b}{2}+\frac{x}{B}\right)}\right] \tag{18}$$

a function of position (x, y) on the wing, as well as of the flight Mach Number. From Fig. 3, then, the value of K_{l_p} for the missile is

$$K_{l_p} = (K_{l_p})_{\text{area } I} + (K_{l_p})_{\text{area } II} + (K_{l_p})_{\text{area } III} \tag{19}$$

From Eqs. (8) and (18), using dS in place of $(dx\,dy)$ for the differential area,

$$(K_{l_p})_I = \frac{\rho n}{2}\int_S \frac{8}{\pi B}\left[\sin^{-1}\sqrt{\frac{B}{x}\left(\frac{b}{2}-y\right)} - \frac{1}{y}\sqrt{\left(\frac{b}{2}-y\right)\left(y-\frac{b}{2}+\frac{x}{B}\right)}\right] y^2\,ds \tag{20}$$

where, from Fig. 3,

$$\left.\begin{aligned} dS = r\,d\mu\,dr &= (x/\cos\mu)\,(dx/\cos\mu)\,d\mu \\ y &= (b/2) - x\tan\mu \end{aligned}\right\} \tag{21}$$

An integration of Eq. (20) using Eqs. (21) results in

$$(K_{l_p})_I = (4\rho n/B^2)\,[(c^2b^2/32) - (7c^3b/96B) + (17c^4/384B^2)] \tag{22}$$

From Eqs. (8) and (17), integration for $(K_{l_p})_{II}$ and $(K_{l_p})_{III}$ is accomplished, and these values, added to Eq. (22), give

$$K_{l_p} = \frac{2\rho n}{B}\left(\frac{c^4}{192B^3} + \frac{c^3b}{48B^2} - \frac{c^2b^2}{16B} + \frac{cb^3}{24} - \frac{ca^3}{3}\right) \tag{23}$$

(2) *Determination of K_{l_δ} from Linearized Supersonic Theory.*—The expression for K_{l_δ} is determined by an integration of Eq. (7). Here again, Eq. (17) gives the value of the lift slope on the wing or tail surface at all points outside of the area bounded by the Mach cone. The lift slope for the area within the Mach cone is given by

$$(dC_L/d\alpha)_{x,y} = (8/\pi B)\sin^{-1}\sqrt{\{B[(b/2)-y]\}/x} \tag{24}$$

derived in references 5 and 6. This value differs from Eq. (18) because the lift forces that give rise to the roll moment L_δ are a result of a uniform angle of attack at all points on the surface—namely, the angle of cant.

Referring again to Fig. 3,

$$K_{l_\delta} = (K_{l_\delta})_{\text{area } I} + (K_{l_\delta})_{\text{area } II} + (K_{l_\delta})_{\text{area } III}$$

From Eqs. (7), (21), and (24),

$$(K_{l_\delta})_I = \frac{\rho n_\delta \delta}{2}\int_{x=0}^{c}\int_{\mu=0}^{\tan^{-1}(1/B)}\left\{\frac{8}{\pi B}\sqrt{\frac{B[(b/2)-y]}{x}}\right\}\frac{yx}{\cos^2\mu}\,d\mu\,dx$$

and

$$(K_{l_\delta})_I = (\rho n_\delta \delta/B^2)\,[(c^2b/4) - (c^3/4.8B)] \tag{25}$$

From Eqs. (17) and (7), the values of $(K_{l_\delta})_{II}$ and $(K_{l_\delta})_{III}$ are determined, and the addition of these values to Eq. (25) gives

$$(K_{l_\delta}) = \frac{\rho n_\delta \delta}{B}\left(\frac{b^2c}{4} + \frac{c^3}{8B^2} - a^2c - \frac{c^2b}{4B}\right) \tag{26}$$

(3) *Determination of the Conventional Aerodynamic Coefficients in Roll.*—It is desirable to express any experimentally or theoretically determined coefficients in terms of the conventionally defined aerodynamic coefficients of roll, C_{l_p} and C_{l_δ}.

By definition,

$$L_\delta = C_{l_\delta}\,qA_pn_\delta\delta b = K_{l_\delta}V^2$$

and

$$L_p = -C_{l_p}\left(\frac{pb}{2V}\right)qA_pbn = K_{l_p}Vp$$

Then,

$$\left.\begin{aligned} C_{l_\delta} &= \frac{2K_{l_\delta}}{\rho bA_pn_\delta\delta} = \frac{2IC_2}{\rho bA_pn_\delta\delta} \\ C_{l_p} &= \frac{-4K_{l_p}}{\rho b^2A_pn} = \frac{-4I}{\rho b^2A_pn}\left(C_1 + \frac{K_R}{m}\right) \end{aligned}\right\} \tag{27}$$

Comparisons of the experimental and theoretical values of C_{l_p} and C_{l_δ} offer a means of evaluating the accuracy of the linearized supersonic theory as applied

FIG. 4. Typical shadowgraph of missile in free flight showing locating pins in the tail fins and supersonic flow phenomena.

here when used to calculate these quantities. It will be noted from Eqs. (27) that accurate measurements of the actual angle of incidence of each tail and wing panel is required for the theoretical determination of C_{l_δ} for any missile tested.

METHOD OF DATA REDUCTION

The experimental values of the aerodynamic coefficients in roll for the missiles tested are determined by the following general procedure for reduction of the data obtained from the aerodynamic range.

(A) Accurate measurements of the angular orientation in roll (ϕ) and the linear position (z) of the missile in space are obtained from each of the photographic plates taken during the flight of the missile down the range. Accurate measurements of the time at which nine of the photographs were taken are determined from the chronograph record and megacycle counters.

(B) The form of the solution $\phi = \phi(z)$ [Eq. (15)] of the theoretical roll equation is "fitted" to the measured values of ϕ and z, and the optimum values of the constants C_1 and C_2 in Eq. (15) are determined by the method of differential corrections.

(C) The value of the retardation constant K_R/m for the missile is determined by existing techniques, using the measured values of z and the time t.

(D) Values of the aerodynamic coefficients in roll are determined and their statistical accuracy (P.E.) is computed.

The details of these four general steps will now be discussed.

(A) *Measurements from the Photographic Plates*

(*1*) *Angular Orientation in Roll.*—In order to determine the roll angle from the shadowgraphs of the missile (see Fig. 4), it is first necessary to identify the quadrant in which a particular reference fin or wing occurs. Therefore, one particular fin must be recognizable in both the vertical and horizontal photographs taken at each station. Identification of the fins was obtained, after considerable experimentation, by locating a small pin in the trailing edge of each fin near the tip. The shape of the four pins differed as seen in Fig. 4, and it was always possible to distinguish at least one of the shapes in both photographs and thereby definitely fix the quadrant of roll orientation. The roll angle of the missile at any station may be calculated from the coordinates of each of the identification pins [Eq. (28)] as obtained from the horizontal and vertical spark photographic plates using the usual methods of reduction of range data for obtaining the spatial position of a point from its images projected on the horizontal and vertical plates. Then, from Fig. 5,

$$\phi_{sta} = \tan^{-1}\frac{\overline{AC} - \overline{CD}}{\overline{AD}} = \tan^{-1}\frac{\overline{BD} - \overline{AB}}{\overline{AD}} = \tan^{-1}\frac{\overline{EG} - \overline{GH}}{\overline{EH}} = \tan^{-1}\frac{\overline{HF} - \overline{EF}}{\overline{EH}} \quad (28)$$

The angular accuracy of the roll angle at a station is estimated to be $\pm 0.7°$ from a comparison of the four individual determinations made according to Eq. (28).

(*2*) *Linear Position of Missile.*—The location of a reference point on each station along the range is known to 0.001 ft. This reference point appears on the photographs, and the location of the center of gravity of the missile in space at each station is accurately and

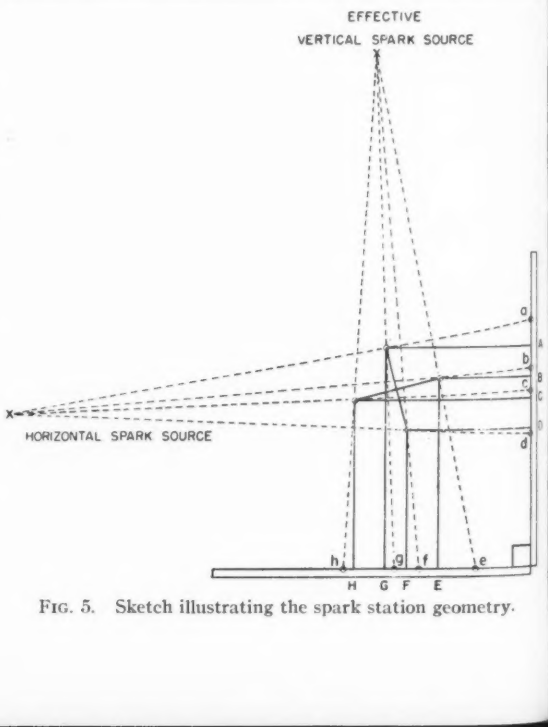

FIG. 5. Sketch illustrating the spark station geometry.

simply determined by the technique presented in reference 3.

(B) *Determination of the Constants in the Roll Equation*

The constants C_1 and C_2, and at the same time the constants A, B, and s, are determined by "fitting" the theoretical form of the roll Eq. (15), $\phi = \phi(z)$, to the ϕ, z data obtained from a particular firing. The process of "fitting" consists first of finding the initial or approximate values of the constants in Eq. (15) (designated as A_0, B_0, S_0, and C_{1_0}) and second of applying the method of differential corrections to determine the optimum values of the constants.

(1) *Method of Differential Corrections.*—Since the roll equation contains an exponential term, no method of least squares has been developed to handle this type of equation directly. However, the roll Eq. (15) may be expanded by a Taylor series about the initial values of the constants

$$\phi = B_0 + s_0 z + A_0 e^{-C_{1_0} z} + \Delta B + z\Delta s + e^{-C_{1_0} z}\Delta A - zA_0 e^{-C_{1_0} z}\Delta C_1 - ze^{-C_{1_0} z}\Delta C_1 \Delta A + z^2 A_0 e^{-C_{1_0} z}[(\Delta C_1)^2/2] + \ldots$$

in which all terms in ΔC_1 and ΔA of order 2 or greater may be neglected if ΔC_1 and ΔA are small. Then,

$$\phi_m - \phi_0 = \Delta B + z\Delta s + e^{-C_{1_0} z}\Delta A - A_0 z e^{-C_{1_0} z}\Delta C_1$$

where

$$\phi_0 = (B_0 + s_0 z + A_0 e^{-C_{1_0} z})$$

initial value of roll angle, and

$$\phi_m = \text{measured value of roll angle}$$

is a linear relation, and the differential corrections (ΔB, Δs, ΔA, and ΔC_1) to the initial value of the constants may be obtained by the usual least squares process. The corrected constants

$$\begin{aligned} A_1 &= A_0 + \Delta A; \qquad s_1 = s_0 + \Delta s \\ B_1 &= B_0 + \Delta B; \qquad C_1 = C_{1_0} + \Delta C_1 \end{aligned} \tag{29}$$

may in turn be used as the initial values, and the process may be repeated until the sum of the squares of the residuals* approaches a minimum. If the process is not convergent,† then either the roll equation does not represent the motion with sufficient exactness or the initial values for the constants A and C_1 are not well determined.

Therefore, the successful application of the method of differential corrections depends upon a fairly accurate determination of the initial values of the constants. The technique employed to obtain them is discussed in the following section.

(2) *Determination of the Initial Values for the Roll Constants.*‡—Differentiation of the roll Eq. (15) yields

$$\phi' = s - C_1 A e^{-C_1 z} \tag{30}$$

and substituting the value of $Ae^{-C_1 z}$ from Eq. (15) into Eq. (30)

$$\phi' = (s + C_1 B) + (C_1 s)z + (C_1)\phi \tag{31}$$

The value of ϕ' may be computed at each station by the method of divided differences,[7] using the known values of ϕ's and z's in Eq. (15), $\phi = f(z)$.

$$f'(z)_0 = (\phi')_0 = f(z_0, z_1) + (z_0 - z_1)f(z_0, z_1, z_2)$$

where 0, 1, and 2 are consecutive stations along the range and $f(z_0, z_1)$ and $f(z_0, z_1, z_2)$ are defined in reference 7.**

The ϕ' at the last two stations, ($n - 1$ and n), however, cannot be computed by the above equation because the second difference cannot be obtained. The ϕ' at ($n - 1$) station is given by

$$(\phi')_{n-1} = f(z_{n-2}, z_{n-1}) + (z_{n-1} - z_{n-2})f(z_{n-2}, z_{n-1}, z_n)$$

and at the last station by

$$(\phi')_n = f(z_{n-2}, z_{n-1}) + (2z_n - z_{n-2} - z_{n-1})f(z_{n-2}, z_{n-1}, z_n)$$

With the ϕ, ϕ', and z values known for each station, Eq. (31) is solved for the constant C_1 by the method of least squares. Using this value of C_1, Eq. (15) is in turn solved by the method of least squares and values of s, B, and A are determined. These four values are then the initial values C_{1_0}, s_0, A_0, and B_0 as required by the method of differential corrections.

(3) *"Fit" of the Roll Equation.*—The final equation representing the rolling motion of the missile is Eq. (15), written with the optimum values of the constants derived from the data by successive applications of the method of differential corrections until the sum of the squares of the residuals approaches a minimum. The fit of the final roll equation to the range data may then be evaluated by a comparison of the statistical magnitude of the final residuals with the magnitude of the estimated error in the measurement of the roll angle from the photographic plates. The statistical magnitude of the final residuals is given by the usual statistical quantity Probable Error,[7] called here "the Probable Error of the residuals"

$$\text{P.E.} = 0.6745\sqrt{\Sigma\Delta\phi^2/(n-4)} \tag{32}$$

where

$\Delta\phi$ = residual
n = number of observations

* Residual here is defined as the difference between the roll angle of the missile as measured and the angle calculated from the roll equation at any distance, z, along the range where the missile was photographed.

† If the sum of the squares of the residuals decreases with successive applications of the method of differential corrections, the process is convergent.

‡ Procedure suggested by Dr. Zdenek Kopal, Professor, Massachusetts Institute of Technology.

** Page 21.

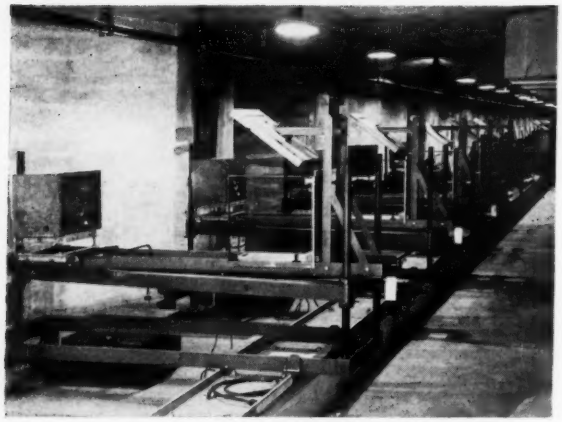

FIG. 6. Aerodynamic Free-Flight Range showing the spark stations located along the flight trajectory.

If the P.E. of the residuals is of the same order of magnitude as the estimated error in measurement of the roll angles from the shadowgraphs ($\pm 0.7°$ approximately), then the final roll equation represents the *best* equation that can be written to fit the data and, as such, represents the true rolling motion of the missile within experimental accuracy.

(C) *Determination of the Value of the Retardation Constant* K_R/m

The retardation constant defined by Eq. (9b) is proportional to the coefficient of drag of the missile. The constant is then determined in the conventional manner described in reference 3, where it is assumed that the time is given by a power series in the distance measured from the center of the range (z_0) as

$$t = a_0 + a_1(z - z_0) + a_2(z - z_0)^2 + \ldots$$

The coefficients a_0, a_1, a_2, etc., are determined from the experimental measurements by the method of least squares, and the drag coefficient is, in turn, determined from these coefficients.

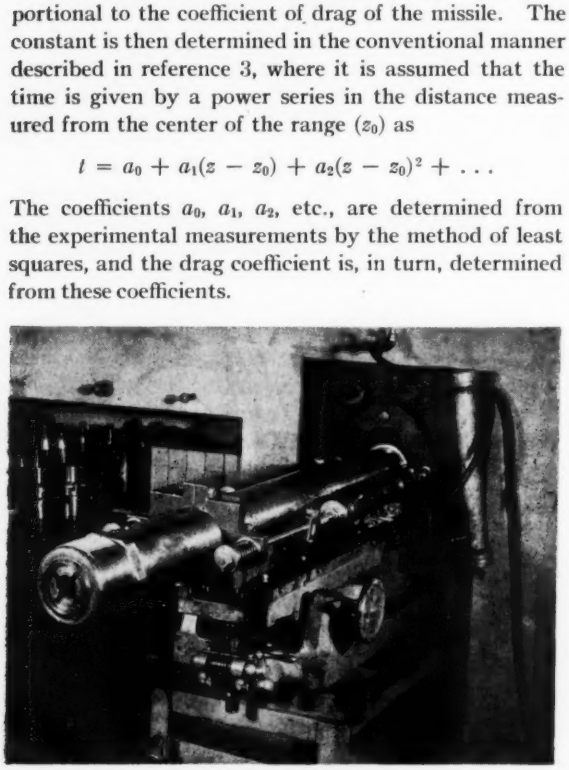

FIG. 7. "Railed" gun for launching missiles.

(D) *Aerodynamic Coefficients and the Statistical Precision*

The values of the constants C_1 and C_2 of the roll equation, as determined by successive applications of the method of differential corrections, may be considered as the best values that the experimental data can yield consistent with the assumptions made in writing the equations of motion. The roll coefficients C_{l_p} and C_{l_δ} are then determined simply by Eq. (27).

The effectiveness parameter, $p_s b/2V$, the steady-state tip helix angle, may be obtained from the linearized theory by

$$\frac{p_s b}{2V} = \frac{b}{2(57.3)}\left(\frac{K_{l_\delta}}{K_{l_p}}\right) \text{ rad.} \tag{33}$$

and, from the experimental data, by substitution of Eqs. (13a) and (13b) into Eq. (33); whence,

$$\frac{p_s b}{2V} = \frac{b}{2(57.3)}\left[\frac{C_2}{C_1 + (K_R/m)}\right] \tag{34a}$$

and using Eq. (16) gives

$$\frac{p_s b}{2V} = \frac{sb}{2(57.3)}\left(1 - \frac{K_R}{C_1 m}\right) \tag{34b}$$

The accuracy of the final aerodynamic coefficients is again expressed by the statistical quantity, P.E., dependent upon the P.E. of the constants in the roll equation. The general equations for the P.E. of any function of independent quantities whose P.E.'s are known is given by[7]

$$R = \sqrt{\left(\frac{\partial Q}{\partial q_1}\right)^2 r_1^2 + \left(\frac{\partial Q}{\partial q_2}\right)^2 r_2^2 + \ldots \left(\frac{\partial Q}{\partial q_n}\right)^2 r_n^2} \tag{35}$$

where

$$Q = F(q_1, q_2, q_3, \ldots, q_n)$$

and $R, r_1, r_2, \ldots, r_n$ are the P.E.'s of $Q, q_1, q_2, \ldots, q_n$, respectively.

Experimental Tests

The purpose of the experimental program is not to present a finished research program but rather to investigate the suitability of the aerodynamic range to the free-flight roll technique presented in this paper. Specifically, the purpose may be restated in three parts:

(1) To determine the accuracy of agreement of the theoretical roll equation with the experimental data measured in the aerodynamic range, as well as to determine the accuracy of the reduction methods used to obtain the roll constants (aerodynamic coefficients) from the data.

(2) To determine the ability of the combined range and technique to reproduce accurately aerodynamic coefficients.

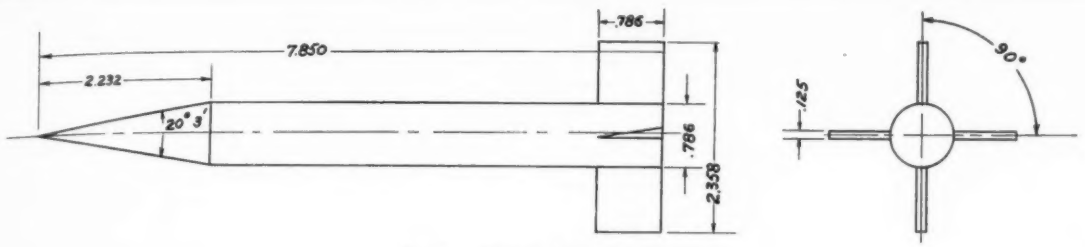

FIG. 8. Design of test missile.

(3) To compare the experimental and theoretical values of the aerodynamic coefficients.

(A) *Experimental Apparatus and Procedure*

(1) *Aerodynamic Range.*—The aerodynamic range and the test procedure are described briefly in the first section of this paper, and further details are presented in reference 3 and Fig. 6. The one unique modification to the equipment is the special "railed" gun (shown in Fig. 7) used for launching winged and/or finned missiles. In the operation of the gun, the projectile is guided by its body in the central cylindrical portion of the barrel, the fins or wings riding freely in the slots.

(2) *Design of Missiles for Firing Program.*—To fulfill the purposes of the program, a single missile design was chosen consisting of the simplest configuration from a construction standpoint, as well as from a standpoint of amenability to theoretical supersonic aerodynamic calculations. The missile design is shown in Fig. 8 and consists of a cone-cylinder fuselage with four rectangular fins in cruciform arrangement. The fin surfaces are single-wedge-shaped with 16 per cent maximum thickness. On each model, two of the tail fins were canted.

For five of the models, the fuselage was of aluminum with wings of Tobin bronze. Bronze wings were used to obtain (1) a higher moment of inertia in roll in order to decrease the rate of acceleration in roll and correspondingly lengthen the curved portion of the measured roll displacement-distance curve, and (2) a higher mass in order to decrease the linear deceleration of the missile and result in more nearly constant-velocity flight. The remaining two models were machined entirely from Tobin bronze to increase further the moment of inertia in roll. A summary of the missile design is given in Table 1.

TABLE 1

Missile Number	Average Angle of Cant on Two Tail Fins, Deg.	Material	Moment of Inertia in Roll, I (Slugs per Sq.Ft.)	Mass of Missile, m (Slugs)
1	2.029	Aluminum fuselage plus bronze fins	1.240×10^{-5}	1.224×10^{-2}
2	4.288	Aluminum fuselage plus bronze fins	1.235	1.221
3	2.108	All bronze	2.186	3.068
4	4.454	All bronze	2.210	3.067
5	1.933	Aluminum fuselage plus bronze fins	1.266	1.226
6	2.100	Aluminum fuselage plus bronze fins	1.263	1.223
7	4.454	Aluminum fuselage plus bronze fins	1.253	1.221

(B) *Results and Discussion*

Four of the missile models (Table 1) were gun-launched at an intended Mach Number of about 1.7 in order to investigate reproducibility. The other three models were fired in order to obtain results at higher Mach Numbers. The actual Mach Numbers that resulted in the seven flights both at the beginning and end of the trajectory, as well as the atmospheric air density and atmospheric velocity of sound, are recorded in Table 2.

TABLE 2

Missile Number	Mach Number at Beginning of Trajectory	Mach Number at End of Trajectory	Mach Number at Center of Timing Data	Velocity of Sound in Range Atmosphere (Ft. per Sec.)	Air Density of Range Atmosphere (Slugs per Ft.)
1	1.790	1.675	1.746	1,135	2.297×10^{-3}
2	1.752	1.635	1.694	1,131	2.296
3	1.621	1.575	1.592	1,121	2.357
4	1.665	1.616	1.637	1,120	2.357
5	2.722	2.587	2.682	1,125	2.342
6	2.301	2.166	2.247	1,132	2.309
7	2.450	2.327	2.416	1,132	2.311

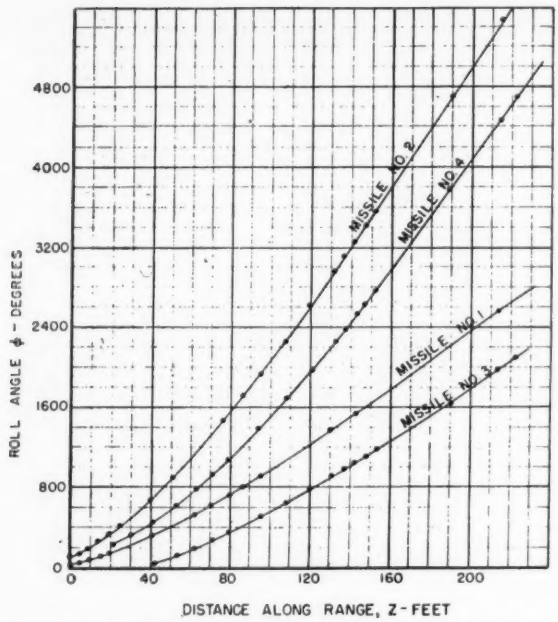

FIG. 9. Measured values of the missile roll angle at the range station locations plotted along with the curve of the derived equation. (The graph does not show the quantitative agreement of the experimental data to within $\pm 1°$ of the derived curve because of the insensitivity of the scale.)

(*1*) *Rolling Motion.*—The angular orientation in roll of the first four models, as measured from the shadowgraphs taken at each spark station along the trajectory, is shown by the points in Fig. 9 to illustrate the data obtained. In this same figure are plotted the equations of the curves that best fit the data as obtained by the methods discussed in the previous section. The agreement of the data to within a degree of the fitted curve cannot be shown in the figure because of the insensitivity of the scale.

The difference between the curves for missile Nos. 2 and 1, as well as Nos. 4 and 3, is a result of the differences in the angles of cant employed. The difference between the curves for missile Nos. 2 and 4, as well as Nos. 1 and 3, is due primarily to the differences in the roll moment of inertia (see Table 1).

The use of a greater moment of inertia, it was felt, would result in a better determination of the roll coefficients because of the slower roll acceleration rate and linear deceleration rate. However, no such variation in experimental accuracy with moment of inertia can be noted in the results, and the accuracy appears dependent only upon the number and distribution along the trajectory of photographs successfully obtained during a given flight.

The excellent "fit" of the roll equation to the experimental points that cannot be observed in Fig. 9 because of size limitations is given in Table 3 as the statistical quantity, P.E. Since the P.E. is small and of the same order of magnitude as the estimated error in roll angle measurements, it may be concluded that the roll

TABLE 3

Model	1	2	3	4	5	6	7
P.E., deg.	0.3	0.7	0.6	0.6	0.7	0.3	0.6

equation represents the actual motion of the models tested to within the experimental error. It therefore appears that the rolling motion is unaffected by the yawing motion for the mean square yaws encountered in the tests (see Table 4).

The optimum values of the constants in the roll equation were obtained by the methods outlined in the Data Reduction Section and are given with their P.E.'s in Table 4 as determined from the reduction.

(*2*) *Aerodynamic Coefficients.*—The experimental values of the aerodynamic coefficients for the models tested may be obtained from the data in Table 4 and Eqs. (27). The theoretical values of the coefficients for the models are obtained from Eqs. (23), (26), and (27). The values for the coefficients are given in Table 5, and their good quality is again indicated by the statistical factor, P.E., the significance of which is discussed in the section on "Method of Reduction."

The experimental values of C_{l_p} and C_{l_δ} (Table 5) are plotted, respectively, in Figs. 10 and 11 against the average flight Mach Number (Table 2). The figures show that values for models 3, 5, and 6 deviate somewhat from the experimental curve. In particular

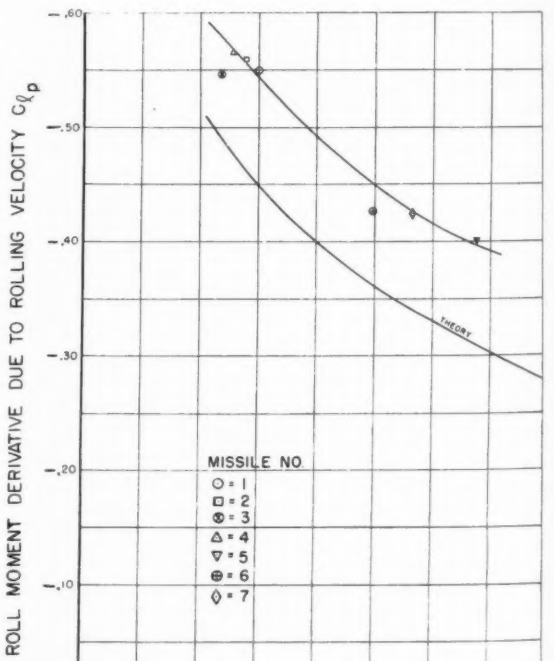

FIG. 10. Experimental values of C_{l_p} as a function of Mach Number plotted along with the theoretical curve.

TABLE 4

Model	1	2	3	4	5	6	7
A	660°	1,386	882	2,285	918	925	1,930
B	−624°	−1,298	−838	−2,079	−919	−900	−1,776
C_1	0.0166	0.0169	0.0096	0.0098	0.0124	0.0127	0.0128
P.E., %	0.2	0.3	2.3	0.5	1.5	2.0	0.4
s	14.90	32.02	15.57	32.64	14.17	15.78	33.58
P.E., %	0.1	0.1	0.8	0.2	0.4	0.9	0.1
$C_2 = C_1 s$	0.247	0.542	0.150	0.321	0.176	0.200	0.429
P.E., %	0.2	0.3	2.4	0.6	1.6	2.2	0.4
K_R/m	2.7×10^{-4}	2.8	1.2	1.2	1.8	2.2	1.9
P.E., %	0.7	0.1	1.1	0.4	1.2	0.1	0.7
YAW^2	1.48°	0.34	0.35	1.15	1.69	1.59	0.09
No. of observations	14	21	14	18	14	14	19

TABLE 5

Model	1	2	3	4	5	6	7
Mach Number	1.746	1.693	1.592	1.637	2.682	2.247	2.416
$-C_{l_p}$ (theory)	0.449	0.460	0.483	0.472	0.310	0.362	0.340
$-C_{l_p}$ (exp.)	0.548	0.559	0.546	0.564	0.401	0.426	0.424
P.E., %	0.2	0.3	2.3	0.5	1.5	2.0	0.4
C_{l_δ} (theory)	0.716	0.740	0.794	0.769	0.461	0.549	0.511
C_{l_δ} (exp.)	0.778	0.806	0.784	0.802	0.570	0.618	0.619
P.E., %	0.2	0.3	2.4	0.6	1.6	2.2	0.4
$\frac{p_s b}{2V}$ (theory)	0.0283	0.0602	0.0303	0.0633	0.0251	0.0277	0.0583
$\frac{p_s b}{2V}$ (exp.)	0.0251	0.0540	0.0264	0.0553	0.0240	0.0261	0.0559
P.E., %	0.04	0.05	0.6	0.2	0.4	0.9	0.1

the discrepancy in the value of model 3 is noted. From Table 5, however, the P.E. associated with the experimental results for models 3, 5, and 6 are three or four times greater than the largest P.E. of any of the other four models. This is positive evidence that the reductions for these three models were weak. The weakness is due not only to the relatively small number of photographs obtained during flight down the range but also to the poor distribution along the range of the stations yielding these successful photographs. In particular, in Fig. 9 for model 3, note the lack of stations at the beginning of the range where data are required for a good determination of the constant C_1. The experimental curves in Figs. 10 and 11 are drawn through the weighted average of the coefficients (weighted on the basis of the P.E.'s) for models 1 through 4 and very near to the coefficient for model 7. This procedure, then, enables the curves to be drawn on the basis of the statistical accuracy of the data points.

The theoretical values of C_{l_p} calculated from the linearized theory as applied in this paper are 16 to 22 per cent less than the experimental values, and the theoretical values of C_{l_δ} are 7 to 17 per cent less than the experimental values.

Concerning this deviation of the experimental values from the theoretical, it will be remembered that the airfoil section used was of triangular shape (single wedge) with about 16 per cent maximum thickness at the trailing edge. A comparison of the theoretical lift of an infinite-aspect-ratio wing of such cross section obtained by the linearized theory with that obtained from the exact theory using the oblique shock equa-

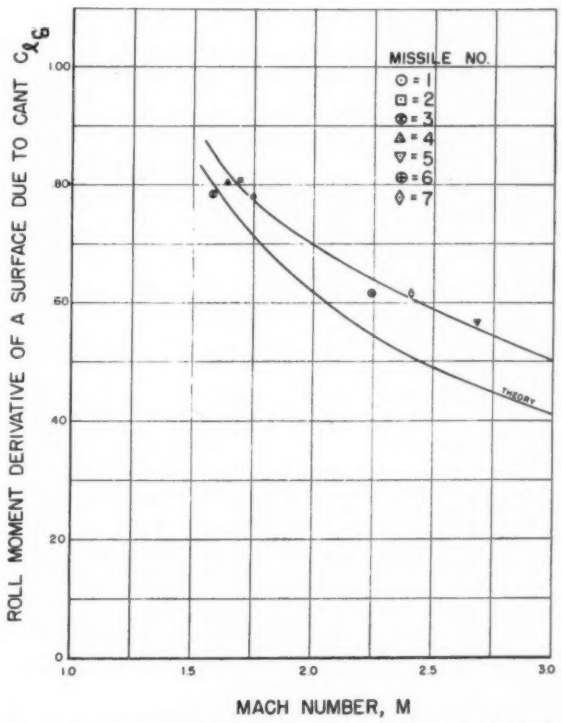

FIG. 11. Experimental values of C_{l_δ} as a function of Mach Number plotted along with the theoretical curve.

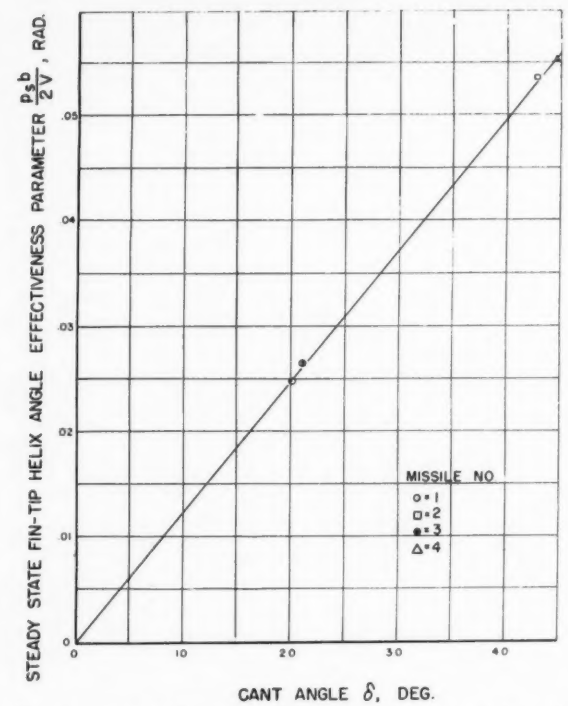

FIG. 12. The effectiveness parameter plotted as a function of the angle of cant on each of two fins.

tions results in about a 15 per cent lower value for the linearized lift at a Mach Number of 1.7 and about 22 per cent at Mach Number of 2.6.

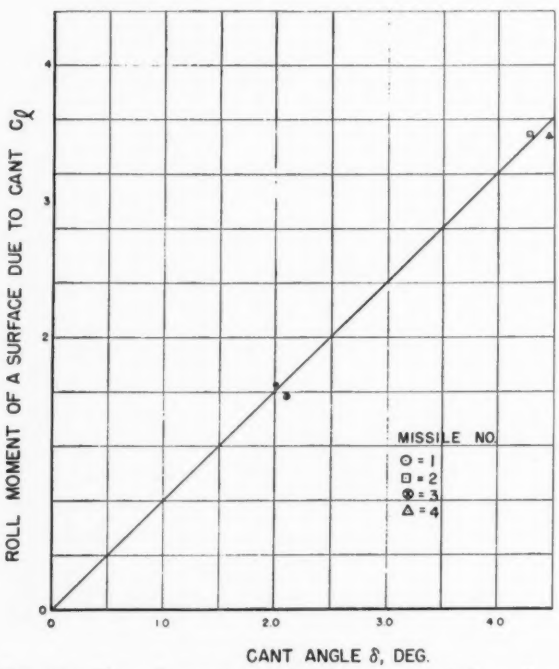

FIG. 13. The roll moment produced by a canted fin surface plotted as a function of the cant angle.

TABLE 6

Model	Mach Number	C_{l_p}	C_{l_δ}	$(p_s b/2V)/\delta$
1	1.665	−0.566	0.820	0.01226
2	1.665	−0.565	0.821	0.01256
3	1.665	−0.530	0.746	0.01261
4	1.665	−0.557	0.787	0.01245
Weighted average		−0.564	0.816	0.01238
P.E. of weighted average, %		0.3	0.6	0.5
Theory		−0.466	0.758	0.014

(3) *Effectiveness Parameter.*—The experimental values for the effectiveness parameter obtained from Eq. (33), Table 4, and the physical measurements and the theoretical values for this parameter obtained from the Eqs. (23), (26), and (34a) are given in Table 5, together with their P.E.'s. Fig. 12 gives the theoretical curve for the effectiveness parameter per degree angle of cant $(p_s b/2V)/\delta$ as a function of Mach Number, together with the experimental points. It is noted that the experimental curve is approximately 12 per cent lower than the theory and does not exhibit the upward curvature in the low Mach Number region.

(4) *Internal Consistency or Reproducibility of the Data, and Linearity.*—The internal consistency or reproducibility of the data was estimated by reducing the experimental values of C_{l_p}, C_{l_δ}, $(p_s b/2V)/\delta$ for the first four models to a common Mach Number of $M = 1.665$ by the theoretical value of the slopes at $M = 1.665$. These reduced values are given in Table 6.

The weighted average obtained from reference 8 is

$$\frac{\sum C/\text{P.E.}^2}{\sum 1/\text{P.E.}^2} = \text{weighted average}$$

and the P.E. of the weighted average, reference 8, is

$$\text{P.E.} = 0.6745 \sqrt{\frac{w_1 v_1^2 + w_2 v_2^2 + w_3 w_3^2 + w_4 v_4^2}{(n-1)(w_1 + w_2 + w_3 + w_4)}}$$

where

$w = 1/\text{P.E.}^2$

v = difference of coefficient from average value at same Mach Number

n = number of observations

These values of P.E., given in Table 6, are a measure of the internal consistency or reproducibility of the data, and their small values indicate that the technique is promising.

In plotting C_{l_δ} vs. M, it was assumed that C_l was linear with δ; this assumption may now be verified by plotting C_l vs. δ, where

$$C_l = C_{l_\delta}\delta$$

It is seen in Fig. 13 that the assumption of linearity is consistent with the experimental results. In Fig. 14, the effectiveness parameter is plotted vs. δ, and it is seen to be linear in good agreement with theory.

Conclusions

(1) The tests establish the validity of the roll equation for accurately representing the true motion of the missile, as well as the accuracy of the reduction methods employed, since the P.E. of the residuals of the "fitted" equation is a maximum of 0.7° and is of the same magnitude as the estimated error in the roll angle measurement.

(2) The tests show that the rolling moment coefficients due to cant and the effectiveness parameter depend linearly on the angle of cant for the range of angles employed in the tests.

(3) The tests show that the absolute theoretical values of the coefficients C_{l_p} and C_{l_δ} as obtained for the 16 per cent thick wing are, respectively, from 16–22 and 7–17 per cent less than the experimental values over the range of Mach Numbers 1.6 to 2.7.

(4) The tests establish the good reproducibility of the aerodynamic coefficients as shown by the weighted P.E.'s of 0.3 per cent for C_{l_p}, 0.6 per cent for C_{l_δ}, and 0.5 per cent for $(p_s b/2V)/\delta$ when the values of the coefficients are reduced to a common Mach Number.

Appendix I—Rolling Moments Due to Angle of Attack α and Angle of Yaw β

These two moments are identical in nature because of the symmetry of the missile surfaces. The magnitude of such a moment is given by

$$L = (\partial C_L/\partial\beta)\beta(\rho V^2/2)S_{w,t}\,b$$

where $(\partial C_L/\partial\beta)$ is termed the stability derivative and $S_{w,t}$ is the area of the wing, tail, or both. Then,

$$L = \left[\frac{\alpha}{B^2}\left(\frac{1-B^2}{AB} - \frac{3+B^2}{3A^2B^2}\right)\right]\frac{v}{V}\,\frac{\rho V^2}{2}\,S_{w,t} \quad \text{(I)}$$

where the expression for $\partial C_L/\partial\beta$ has been obtained from reference 9 and β now is replaced by the ratio v/V, where v is the sideslip velocity. In Eq. (I) A is defined as the aspect ratio of the surface considered. Now, when α, the angle of attack, is replaced by its equivalent w/V, where w is the component of missile velocity in the vertical plane, Eq. (I) becomes

$$L = \left[\frac{1}{B^2}\left(\frac{1-B^2}{AB} - \frac{3+B^2}{3A^2B^2}\right)\right]\frac{bS_{w,t}}{2}(vw) \quad \text{(II)}$$

But (vw) for the motions resulting from these experimental tests is the product of two small disturbance velocities compared with V, and, as such, the moment is of second order and *negligible*.

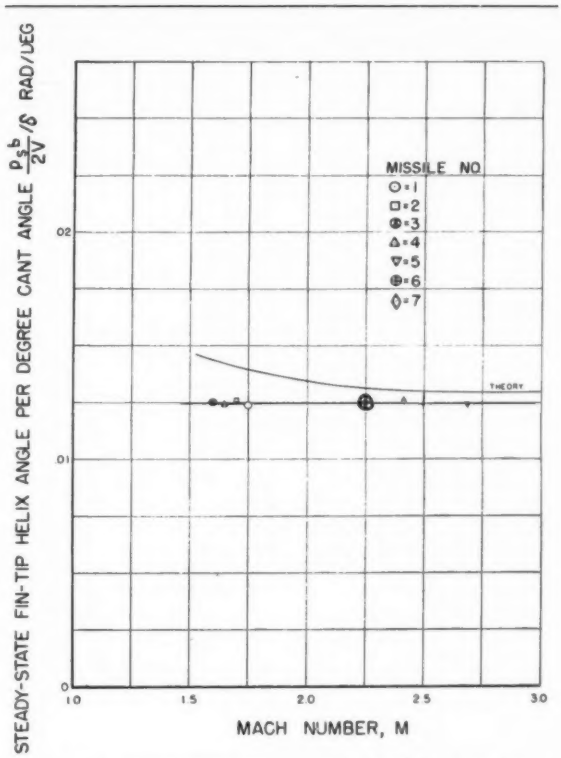

Fig. 14. The effectiveness parameter $(p_s b/2V)/\delta$ plotted as a function of the flight Mach Number.

References

[1] Charters, A. C., *Some Ballistic Contributions to Aerodynamics*, Journal of the Aeronautical Sciences, Vol. 14, No. 3, p. 155, March, 1947.

[2] Charters, A. C., and Thomas, R. N., *The Aerodynamic Performance of Small Spheres from Subsonic to High Supersonic Velocities*, Journal of the Aeronautical Sciences, Vol. 12, No. 4, p. 468, October, 1945.

[3] Bolz, R. E., and Nicolaides, J. D., *A Method of Determining Some Aerodynamic Coefficients from Supersonic Free-Flight Tests of a Rolling Missile*, B.R.L. No. 711, April, 1949.

[4] Liepmann, H. W., and Puckett, A. E., *Aerodynamics of a Compressible Fluid*, Chapt. 9; John Wiley & Sons, Inc., New York, 1947.

[5] Evvard, J. C., *Distribution of Wave Drag and Lift in the Vicinity of Wing Tips at Supersonic Speeds*, N.A.C.A. T.N. No. 1382, 1947.

[6] Snow, R. M., and Bonney, E. A., *Aerodynamic Characteristics of Wings at Supersonic Speeds*, Bumblebee Report No. 55, The Johns Hopkins University, Applied Physics Laboratory, March, 1947.

[7] Whittaker, E. T., and Robinson, G., *The Calculus of Observations*, Blackie & Sons, 1926.

[8] Scarborough, J. B., *Numerical Mathematical Analysis;* The Johns Hopkins Press, 1930.

[9] Harmon, S. M., *Stability Derivatives of Thin Rectangular Wings at Supersonic Speeds*, N.A.C.A. T.N. No. 1706, November, 1948.

Base Drag and Thick Trailing Edges

SIGHARD F. HOERNER*
Air Materiel Command

ABSTRACT

The negative pressure originating behind the flat base of projectiles presents a drag component that is consequently termed "base drag." As illustrated in Fig. 1, the same kind of drag exists for every elongated body the flow around which is separated from its rear side, such as airfoil sections, the trailing edges of which are cut off or thickened. The same type of drag is also found behind certain sheet-metal joints. It is possible to correlate all the various base drags with each other by considering the effect of the boundary layer originating from the forebodies. Analyzing competent measurements, simple formulas are found with which to calculate the drag of tail turrets and blunt trailing wing edges. In the case of thicker sections, such as are used for the blade roots of propellers, the lift is also affected, and the lift-drag ratio can be improved remarkably by thickening the trailing edge. At supersonic speeds the base drag approaches the natural limit as given by zero pressure (vacuum). Depending upon the body shape, the base pressure assumes an approximately constant percentage of the theoretical limit.

SYMBOLS

y	=	coordinate across direction of flow
l	=	length of bodies in direction of flow
c	=	wing chord
h	=	height or thickness of trailing edge
d	=	diameter of the base or supporting rod, respectively
D	=	maximum body diameter
s	=	thickness of the boundary layer
v	=	local velocity within boundary layer
V	=	velocity of flow or flight
q	=	dynamic pressure $0.5\rho V^2$
S	=	area to which the drag coefficient is referred
C_f	=	coefficient indicating drag due to skin friction and surface protuberances
C_{DB}	=	base drag, based upon base area
C_D	=	body drag, based upon maximum cross-section area
C_{D0}	=	profile drag coefficient, based upon wing area
Δp	=	static pressure difference
B	=	subscript indicating the base

In several figures, a "dot" is used as a subscript, indicating the drag coefficient based upon the frontal area. C_{DP} is eventually used instead of C_{D0}.

(1) BASE DRAG OF THREE-DIMENSIONAL BODIES

(A) *Mechanism of Base Drag*

BY EXAMINING THE FLOW PATTERN around and behind the base of a projectile (Fig. 1a), it is found to be that of a jet pump. The jet—that is, the outer flow—placed like a tube around the space behind the base, mixes with the dead air and tries to pump it away. However, since there is no supply from which additional air can be drawn, the pump has no delivery, and its only effect is to reduce the static pressure on the body base.

The base drag of projectiles is often quoted to be around $C_{DB} = 0.2$, equivalent to a base pressure $\Delta p_B/q = -0.2$. However, by studying available pressure or drag measurements, the base pressure is recognized to depend largely upon the length of the forebody, the ratio of base to body diameter, and the surface conditions of the projectile.

The base pressure is proportional to the dynamic pressure of the outside flow. Evidently, however, the boundary layer existing at the end of the forebody serves as an insulation sheet, reducing the effective dynamic pressure of the jet-pump mechanism. The boundary-layer thickness is proportional to the drag originating from the surface of the forebody. Consequently, in Fig. 2, the drag coefficient

$$C_{fB} = D_{\text{skin}}/q\,S_B = C_f(S/S_B) \tag{1}$$

is chosen as the parameter upon which the base drag is considered to depend. In this equation, C_f indicates the skin drag of the forebody, which includes not only the friction drag but also any additional pressure-drag components originating from the surface, such as the drag of driving bands or other protuberances.

In supersonic cases, the wave drag is not to be included in C_f. This kind of drag generally does not noticeably increase the boundary-layer thickness, since the equivalent momentum is generally carried sideways by the respective shock waves. Of course, there remains some reduction in dynamic pressure behind a shock wave. Between $M = 1$ and 2, however, this loss is relatively small—that is, in the order of less than 10 per cent—when considering projectile bodies with pointed and slender noses. Therefore, by evaluating supersonic tests,[16, 20, 21] the wave drag was entirely neglected.

The available experiments on projectiles and fuselages (Fig. 1b), as plotted in Fig. 2, show approximately

$$C_{DB} = 0.029/\sqrt{C_{fB}} \tag{2}$$

As far as the tests were extended, the base pressure varies between $\Delta p_B/q = -0.03$ and -0.30. From analysis, the thickness of the boundary layer at the end of a projectile is found to be, roughly,

$$s/D = C_{fB} \tag{3}$$

valid for small drag coefficients. Consider, for example, the case with $C_{fB} = 1$, with the boundary layer extend-

Received October 17, 1949.

* Dr.-Ing. habil. Wright-Patterson Air Force Base.

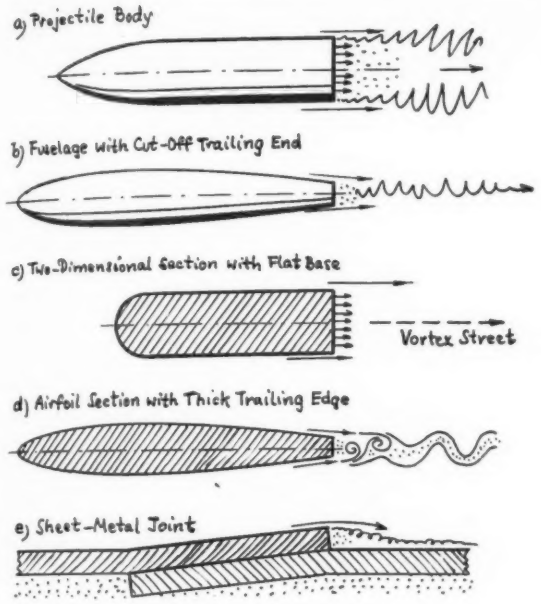
a) Projectile Body
b) Fuselage with Cut-Off Trailing End
c) Two-Dimensional Section with Flat Base
Vortex Street
d) Airfoil Section with Thick Trailing Edge
e) Sheet-Metal Joint

FIG. 1. Several cases of base drag.

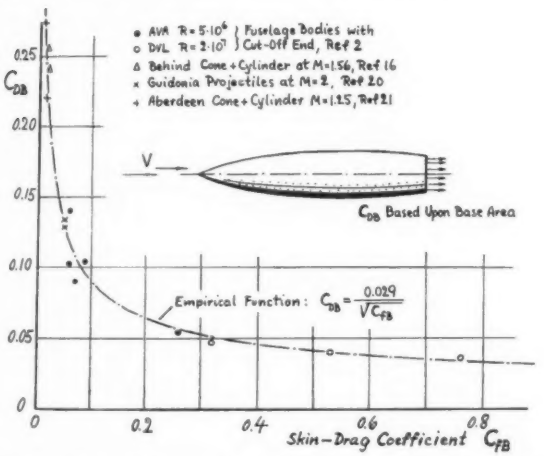
AVA R = 5·10⁶ } Fuselage Bodies with
DVL R = 2·10⁷ } Cut-Off End, Ref 2
Behind Cone+Cylinder at M=1.56, Ref 16
Guidonia Projectiles at M=2, Ref 20
Aberdeen Cone+Cylinder M=1.25, Ref 21
V
C_DB Based Upon Base Area
Empirical Function: C_DB = 0.029/√C_fB
Skin-Drag Coefficient C_fB

FIG. 2. Drag originating from the base of three-dimensional bodies, depending upon their skin drag.

ing outside and around the base for a thickness equal to approximately two-thirds of the base diameter. Here, it seems that the effect of the "jet pump"—that is, the amount of negative base pressure—is reduced to one-tenth of that near to $C_{fB} = 0$.

(B) *Effect of Boat-Tailing*

In the case of bodies, such as in Fig. 1b, where the base diameter is smaller than the maximum diameter of the body, the mechanism of the base drag remains essentially the same as in the case of Fig. 1a. Referring the base drag to the maximum cross section of the body and with $C_{fB} = C_D\,(D/d)^2$, from Eq. (2),

$$\Delta C_D = \left(\frac{d}{D}\right)^2 C_{DB} = \frac{0.029}{\sqrt{C_D}}\left(\frac{d}{D}\right)^3 \qquad (4)$$

with C_D indicating the original skin drag of the body with $d \to 0$. Fig. 3 presents measurements on a smooth and slender streamline body, the trailing end of which was cut off in steps.[2] Fig. 4 shows the drag increment ΔC_D, depending on the diameter ratio d/D. Curves, according to Eq. (4), seem to interpret the measured values sufficiently well.

All this consideration of boat-tailing assumes, however, a flow pattern attached to the sides of the tail. In cases where the tail is too short and the flow is separated from its flanks, the whole cross-section area of the body has to be considered as base and the proper drag has to be determined according to Eq. (2). Round-

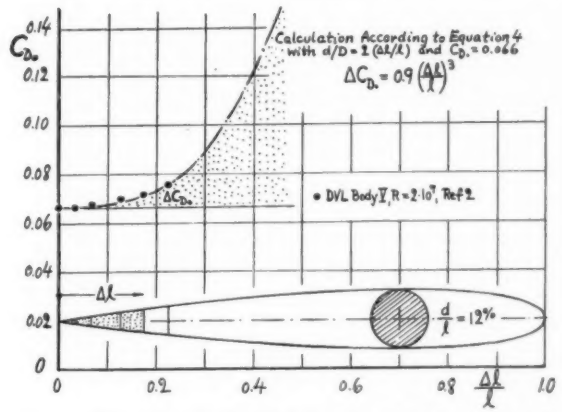

FIG. 3. Drag of a fuselage body, the end of which is cut off.

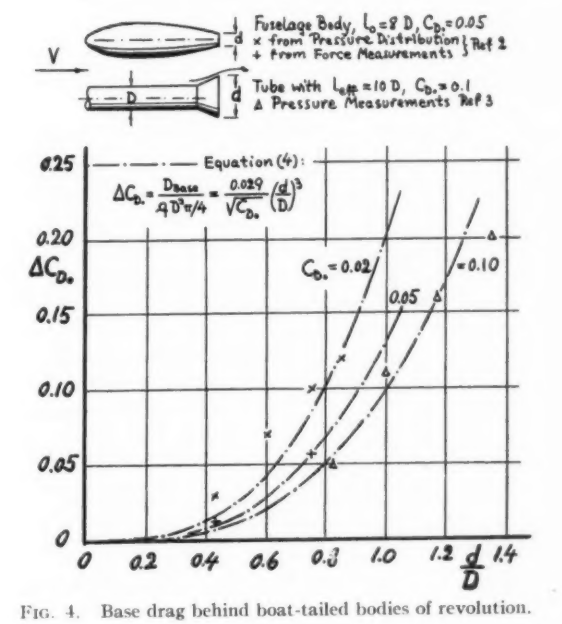

FIG. 4. Base drag behind boat-tailed bodies of revolution.

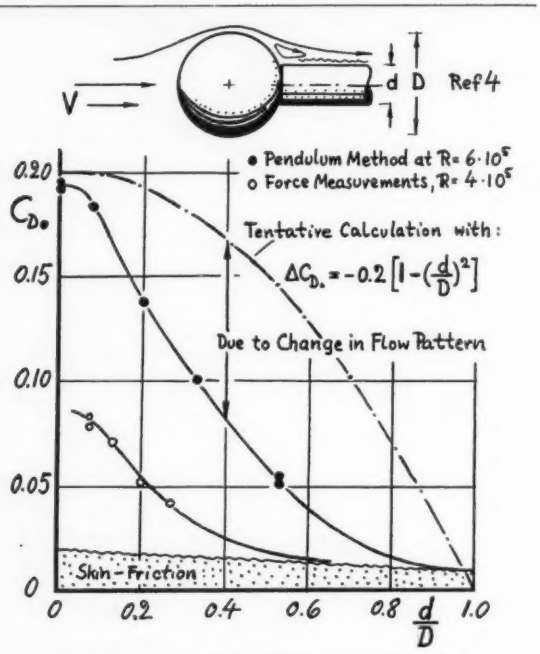

FIG. 5. Drag of spheres at Reynolds Numbers above the critical, depending upon the diameter of the supporting rod.

ing the blunt end of a fuselage, for instance, affects the base drag only as far as the round edge is able to lead the flow somewhat farther into the dead space. Reference 2 indicates a reduction of base drag coefficient (C_{DB} = 0.04 to 0.06) by ΔC_{DB} = 0.005 to 0.010 upon adding a half sphere to the cut-off end of a fuselage body. This result applies, however, to a smooth body only. If one considers a real airplane fuselage with a coefficient two or three times as high (C_D = 0.1 to 0.2), the effect of rounding the blunt end is expected to be hardly noticeable.

Besides the experiments in reference 2, there are also some points included in Fig. 4 measured behind a tube. A collar was attached to the rear end of this tube, and pressure measurements were made within the dead space behind the collar. The tests show that the theory, according to Eq. (2), also holds true in this special case with $d/D > 1$.

The fuselage of a military airplane has a drag coefficient of the order of C_D = 0.15 when accounting for the usual surface irregularities and protrusions. The base drag caused by cutting off or thickening the trailing end amounts to ΔC_D = 0.09 for d/D = 1 (case like Fig. 1a). In order to accommodate a tail turret, however, a diameter ratio d/D = 0.5 may be sufficient. The corresponding amount of drag ΔC_D is less than 0.01, which is comparatively small—that is, in the order of 6 per cent of the fuselage drag.

(C) *Effect of Supporting Rod*

In order to support projectile models in wind tunnels, a sting is usually used leading from downstream to the base. From measurements on spheres, as plotted in Fig. 5, it is known that such a rod affects the drag remarkably as far as Reynolds Numbers above the critical are concerned. At first, one assumes that the drag is reduced because a portion of the rear surface of the sphere and the corresponding amount of base drag is covered or cut out by the rod. A tentative calculation, however, accounting for this effect does not check the actual drag reduction. Evidently, the flow pattern of the sphere is changed because of the addition of the rod. The cross section of the "jet pump," as described above, is changed from a circular to a ring-shaped form, and, as outlined later, the pump effect is thus improved. Consequently, the partial flow separation still existing behind the sphere at supercritical Reynolds Numbers and the corresponding pressure drag are reduced.

The base drag behind projectiles and similar bodies is different from that of the sphere; the separation is fixed at the sharp edge of the base. Starting from d/D = 1, a ring-shaped base area is formed upon decreasing the rod diameter. The corresponding flow pattern can be considered as a two-dimensional one, and the drag can be properly calculated from Eq. (9). At d/D = 0, however, Eq. (2) for three-dimensional base drag has to be applied. Between this point and the two-dimensional curve one has to guess as to the course of the base pressure. Tentative calculations, the thickness of the boundary layer and the effective dynamic pressure of the "jet pump" being considered,

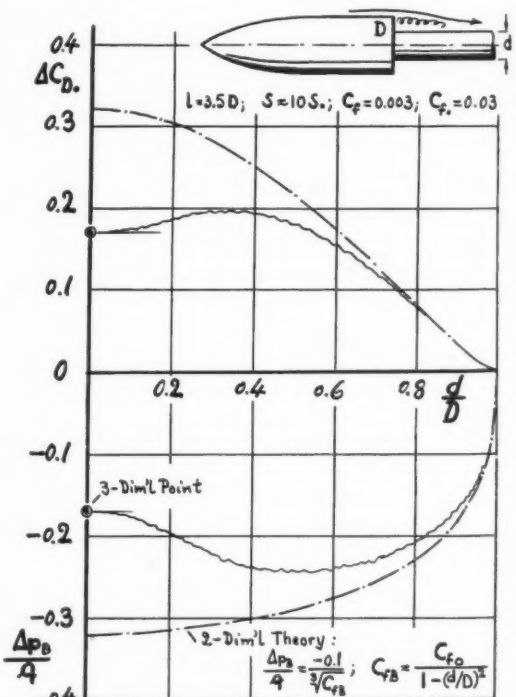

FIG. 6. Variation of base pressure due to rear supporting rod.

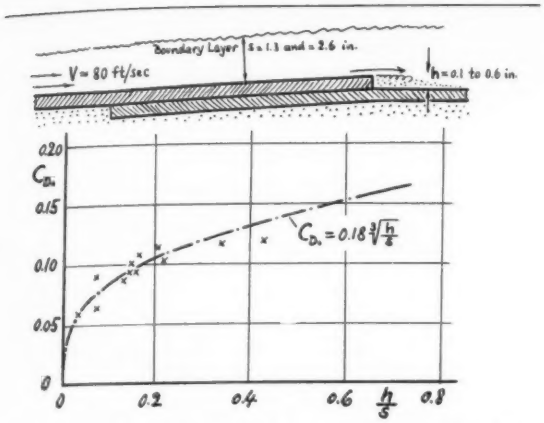

FIG. 7. Drag of a sheet-metal joint; experimental points from reference 5.

suggest a slight increase of the negative amount of base pressure upon increasing the rod diameter beyond $d/D = 0.1$. Model tests, especially in high-speed and supersonic wind tunnels, usually employ rods heavier than according to this permissible ratio.

Considering the base-pressure coefficient ΔC_D in the upper part of Fig. 6, the variation is not so great as that of the pressure coefficient. Contrary to Fig. 5, however, there is no decrease of base drag to be expected as far as diameter ratios smaller than 0.5 are concerned.

(2) Drag of Sheet-Metal Joints

The flow pattern behind the sharp-edged sheet-metal joint, as shown in Fig. 1e, is similar to that past the thick trailing edge of an airfoil section (Fig. 1d). In both cases, the corresponding pressure drag is, by principle, the same kind as that originating from the base of a projectile.

The general distribution of the velocity across a turbulent boundary layer is

$$v/V = (y/s)^{(1/6 \text{ or } 1/7)} \tag{5}$$

The drag of a small body, placed within the boundary layer, is proportional to the effective or average dynamic pressure q_e, corresponding to its height h.

$$q_e/q = 0.7\ (h/s)^{1/3} \tag{6}$$

Consequently, in Fig. 7, the drag of sheet-metal joints, similar to that in Fig. 1e, follows more or less accurately the $^1/_3$ power of h as far as the range of $h/s < 1$ is concerned.

$$C_D = 0.18\ \sqrt[3]{h/s} \tag{7}$$

This trend is proved by many other measurements on various surface protuberances.[5]

With the velocity distribution as given in Eq. (5), the skin-drag coefficient of one side of a plane plate is approximately

$$C_f = 0.2\ (s/l); \quad C_{fB} = 0.2\ (s/h) \tag{8}$$

when considering the "base" of a sheet-metal joint. By introducing $h/s = 0.2/C_{fB}$ into Eq. (7), the following results:

$$C_{DB} = 0.1/\sqrt[3]{C_{fB}} \tag{9}$$

This function is plotted in Fig. 8, together with the experimental points as taken from Fig. 7.

(3) Characteristics of Thick Trailing Edges

(A) Drag at Trailing Edge of Two-Dimensional Bodies

Fig. 8 presents the available measurements on the additional drag, originating from airfoils, the trailing edges of which are either thickened (Fig. 1c) or cut off (Fig. 1d), thus forming a surface equivalent to the base of projectiles. Considering such tests, the value C_{fB} is found from

$$C_{fB} = 2\ C_f(c/h) \tag{10}$$

with C_f indicating the skin drag proper to all of the body in front of the base—that is, including any supervelocity effects and the drag of surface roughness and protuberances. For most of the experiments at smaller C_{fB} values,

$$C_{DB} = 0.135/\sqrt[3]{C_{fB}} \tag{11}$$

At the same coefficient C_{fB}, if one compares Figs. 2 and 8, the pressure difference behind the trailing edge of airfoils appears to be at least three times as high as the base pressure of three-dimensional bodies. This difference can be understood upon studying the velocity distribution across the wake behind the body. Assume a boundary layer, with a distribution as given in Eq. (5), as arriving at the edge of the base, and the character of this distribution may be more or less maintained upon entering the space behind the base, as far as the two-dimensional case is concerned. In the three-

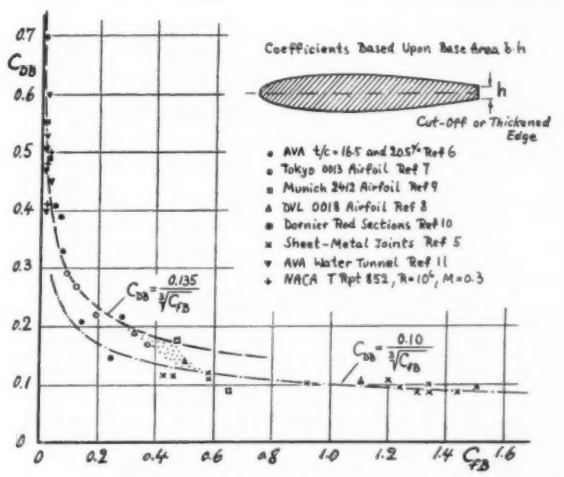

FIG. 8. Drag due to thickened or cut-off trailing edge of airfoil sections.

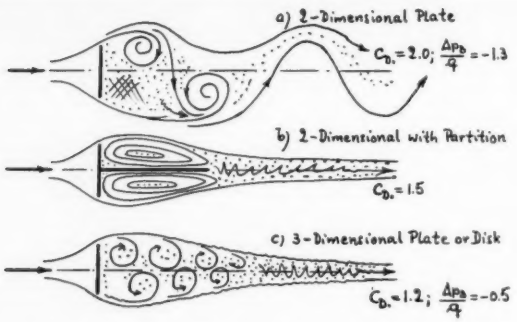

FIG. 9. Flow pattern past various plates. In (b), $\Delta p_B/q = 0.8$.

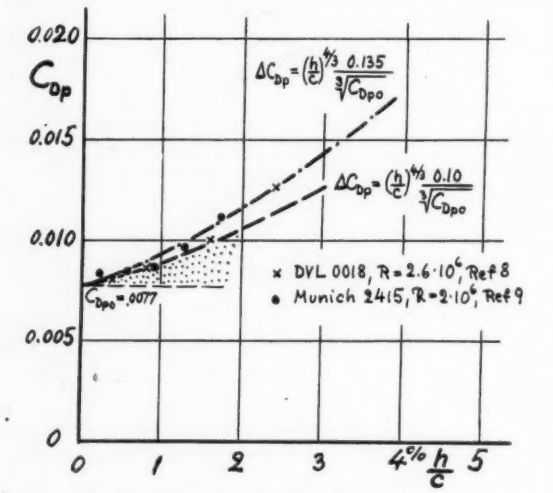

FIG. 10. Profile drag, at $C_L = 0$, of airfoil sections, the trailing edges of which are cut off or thickened.

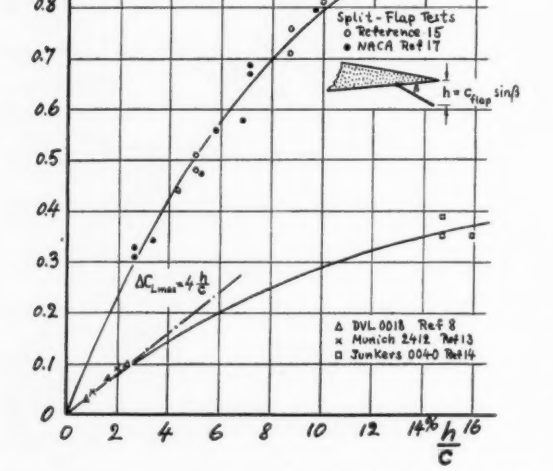

FIG. 11. Increase in maximum lift due to thickness of trailing edge.

dimensional case, however, the boundary-layer material is transferred from a ring-shaped to a circular cross section. In doing this by velocity and volume, it is found by mathematical means that the power in Eq. (5) is changed from $^1/_6$ to $^1/_3$. Consequently, the distribution of the dynamic pressure is changed from the $^1/_3$ to the $^1/_{1.5}$ power of the distance or the radius, respectively. Confirming this trend, the power in Eq. (2) is $^1/_2$ as compared to $^1/_3$ in Eqs. (9) and (11). At the same time, the magnitude of the average dynamic pressure within the boundary layer is reduced to roughly one-third of that in the two-dimensional case. Most of the difference in base drag is thus sufficiently explained.

In Fig. 8, most of the measurements on airfoil sections show somewhat higher drag coefficients [Eq. (11)] than the sheet-metal joints [Eq. (9)]. This difference is probably attributable to the flow pattern. The mixing of the outer flow with air from the dead space behind the base does not proceed so smoothly as illustrated in Fig. 1a. Instead, the pattern is more irregular, forming bigger vortices, intruding deeper into the space once in a while, and carrying away air particles in lumps. Behind two-dimensional bodies, the flow usually assumes the regular stable pattern of the von Kárman vortex-street, as illustrated in Fig. 9a. Because of the vigorous and extended up-and-down movement of this street, the exchange of momentum between the outer flow and the air particles in the dead space is intensified. On the other hand, in the case of the sheet-metal joints, any larger vortex movement is slowed down and more or less suppressed by the wall along which the movement takes place. Experiments in a water tunnel[12] prove that in the absence of the vortex street—that is, with a flow pattern as illustrated in Fig. 9b—the drag coefficient of a plate is reduced from approximately 2.0 to 1.5. This means a reduction of the negative "base" pressure from $\Delta p/q \approx -1.3$ to -0.8. Approximately the same ratio is found in Fig. 8 between the respective two curves (constants 0.135 and 0.10).

The base-drag coefficients in Eqs. (9) and (11) are converted into profile-drag coefficients by multiplying them with h/c.

$$\Delta C_{D0} = \frac{0.10}{\sqrt[3]{C_{D00}}}\left(\frac{h}{c}\right)^{4/3}; \quad \Delta C_{D0} = \frac{0.135}{\sqrt[3]{C_{D00}}}\left(\frac{h}{c}\right)^{4/3} \qquad (12)$$

where $C_{D00} = C_{fB}\,(h/c)$ indicates the profile drag of the section for $h/c = 0$. Fig. 10 (like Fig. 8) shows a transition of the experimental points from one of the calculated curves to the other. Obviously, for small values of h—that is, as long as the edge is thinner than roughly one or one-half times the boundary-layer thickness—a regular vortex street does not originate.

(B) *Effects of Trailing Edge on Lift*

In the case of wings, thickening the trailing edge not only affects the drag but also the lift. As evident from

Fig. 11, the thick edge works similar to a split flap, increasing the maximum lift approximately by

$$\Delta C_{L\,max.} = 4(h/c) \tag{13}$$

This effect is in the order of one-third of that of an ordinary split flap deflected to 90°. Combining Eqs. (9) and (13), the efficiency of an airplane is given by

$$\frac{C_{L\,max.}}{C_{D\,min.}} = \left(C_{L\,max.\,0} + 4\,\frac{h}{c}\right) \div \left[C_{D\,min.\,0} + \frac{0.1}{\sqrt[3]{C_{D00}}}\left(\frac{h}{c}\right)\right] \tag{14}$$

For conventional values, such as $C_{L\,max.} = 1.4$, $C_{D\,min.} = 0.025$, and $C_{D00} = 0.01$, this equation has its maximum between h/c = (0 and 0.4) per cent. This means, with $h/c = 0.4$ per cent, the ratio $C_{L\,max.}/C_{D\,min.}$ is about the same as at $h = 0$. Four-tenths per cent is considered permissible, and the corresponding thickness of the trailing wing edge of any airplane is found to be between $^1/_8$ and 1 in., depending upon the size of wing and plane.

The effect of a blunt trailing edge on the lift-curve slope is similar in relative magnitude to that upon the maximum lift.[7, 8] This effect may be important in the case of control surfaces.

Fig. 12 suggests another application of the thick trailing edge. The lift characteristics of a 40 per cent thick section are remarkably improved above $C_L = 0.4$ when using a thick trailing edge; the maximum lift/drag ratio is increased by some 100 per cent. Such sections—that is, profiles with high thickness ratios—are employed at the blade roots of propellers. It appears to be favorable, in this case, to manufacture the trailing edge with h/t in the order of 20 per cent. In this way, the minimum drag is not necessarily increased. The flow past thick sections is usually somewhat detached from the trailing edge. Consequently, thickening this edge means filling out the dead space. The experiments in reference 14 lead one to assume a slight reduction of drag with $h/t = 10$ per cent or $h/c = 4$ per cent, for a 40 per cent thick profile. Such sections may be especially advantageous in the case of turboprop engines, where the combustion air usually is taken in between and around the blade roots.

(4) Base Drag at Supersonic Speeds

At first there is no fundamental change to be expected in the mechanism of the "jet pump" because of approaching and exceeding the speed of sound. The negative base pressure finds a natural limit, however, as the condition of vacuum is reached. The so-defined maximum amount of base-pressure and base-drag coefficient is a function of the Mach Number.

$$C_{DB\,max.} = -\left(\frac{\Delta p}{q}\right)_{max.} = \frac{2}{\gamma M^2} = \frac{1.42}{M^2} \tag{15}$$

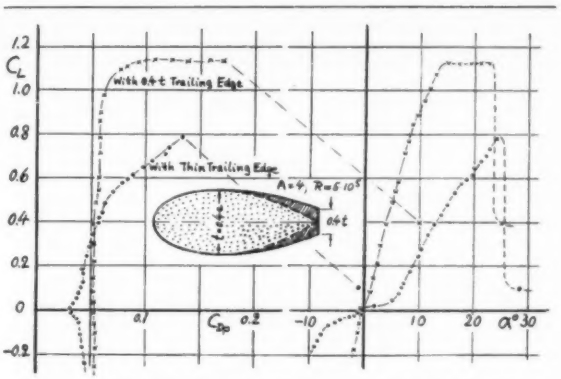

FIG. 12. Lift and drag of a 40 per cent thick airfoil with two different thickness ratios of the trailing edge.[14] $A = 4$; $c = 5.9$ in.; $R_{eff.} = 5 \times 10^6$.

with the constant $\gamma = 1.405$. As shown in Fig. 13, this upper limit is never likely to be encountered by any base pressure in the subsonic field. At supersonic Mach Numbers, however, the theoretical limit comes down remarkably. A series of base-pressure measurements carried out on projectiles and similar bodies suggests a certain percentage of the theoretical amount

$$C_{DB} = 0.5\,C_{DB\,max.} \approx 0.7/M^2 \tag{16}$$

Of course, this drag is true only for a certain boundary-layer thickness—that is, for a specific value C_{fB} as used in Fig. 2 and Eq. (9). In the case of Eq. (16) the correct subsonic value of C_{DB} is in the order of $C_{DB} = 0.25$.

Experiments recently published in reference 19 confirm the hypothesis as expressed in Eq. (16). Furthermore, these tests are remarkable because they are the only known ones extending through the speed of sound. In the vicinity of $M = 0.9$, the tests show a minimum in the order of $C_{DB} = 0.08$. Considering the flow pattern proper for this Mach Number, the low base-pressure difference can be explained when assuming that between $M_{crit.}$ and $M = 1$ most of the drag is caused by flow separation. Correspondingly, the effective dynamic pressure of the "jet pump" mechanism is highly reduced. In order to account for $C_{DB} = 0.08$, it is sufficient to assume in Fig. 2 a forebody drag-coefficient $C_{fB} = 0.15$. The flow pattern changes rapidly, however, when approaching $M = 1$. Here, the loss of dynamic momentum, as equivalent to the drag of the forebody, is evidently shifted from the boundary layer into the outer space. With most of the momentum being carried away from the body by means of pressure waves, the dynamic pressure is not remarkably reduced to any extent around the base, and, as done before when evaluating the experiments of reference 1 in Fig. 2, only the "skin drag" of the forebody is to be considered as affecting the base pressure.

When the subsonic base drag of any body is known, it is possible to estimate the course it will take when approaching the upper theoretical limit [Eq. (15)].

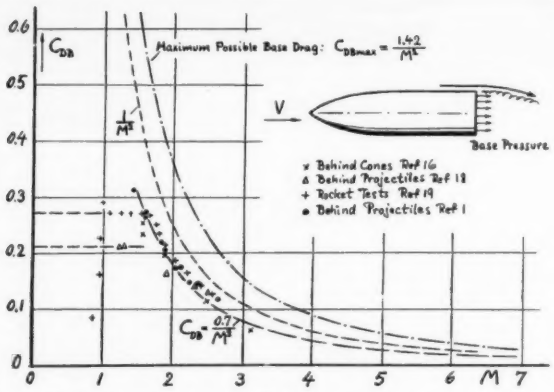

FIG. 13. Base-drag coefficient at supersonic speeds.

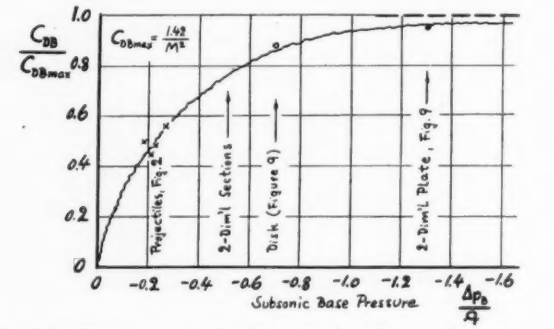

FIG. 14. Function, assisting in estimating the base drag of any body.

In order to assist in such estimating, Fig. 14 was prepared. Including data as found for plates, the rear side of which can also be considered as base, three experimental points are available. From these points, the zero point, and the upper limit as given by $C_{DB} \div C_{DB\ max.} = 1$, a curve is defined which permits one to make reasonable estimates of the base drag at supersonic speeds.

Comparing the base drag to the wave drag as originating from the rear of double cones and double-wedge sections, limiting Mach Numbers are found beyond which single cones or wedges, with half the nose angle and flat base, are superior as to their total drag over the double shapes. For a 10 per cent thick wedge section, for example, this point is reached between $M = 2$ and 3.

RESULTS

(1) The base drags of projectiles and of fuselages with blunt or cut-off trailing end are a distinct function of the forebody drag (Figs. 2 and 8).

(2) From the drag characteristics of sheet-metal joints (Fig. 7), it is possible to calculate the drag originating from the blunt or cut-off trailing edge of airfoil sections (Figs. 8 and 10).

(3) A thick trailing edge is suitable to improve the lift and the lift/drag ratio of thicker airfoil sections (Fig. 12). Such sections have practical interest for the blade roots of propellers.

(4) At supersonic speeds the base drag is related to the maximum possible pressure differential, which is that between vacuum and the ambient pressure (Fig. 13). The supersonic drag behind any body can be estimated (Fig. 14) when the subsonic coefficient is known.

REFERENCES

[1] Bach, *Druckverteilungsmessungen an Geschossmodellen (Pressure Distribution Measurements on Projectile Models)*, Report ZWB UM 6057 (Aachen 1945); Trans. A.T.I. 2457, CADO, Wright-Patterson Air Force Base.

[2] Kosin and Lehmann, *Ein Beitrag zur Aerodynamik des Rumpfes (Contribution to the Aerodynamics of Fuselages)*, Jahrbuch D Luftfahrtforschung, p. I 241, 1942.

[3] Winter and Jaklitsch, *Ueber die zusaetzliche Sogwirkung grosser Klappenausschlaege bei Duesenkuehlern (About the Suction Behind Radiator Flaps)*, ZWB Tech. Berichte, p. 309, 1944.

[4] Hoerner, *Versuche mit Kugeln betreffend Kennzahl Turbulenz und Oberflaechenbeschaffenheit (Experiments with Spheres)*, Luftfahrtforschung, p. 42, 1935; Trans., N.A.C.A. T.M. No. 777.

[5] Wieghardt, *Erhoehung des turbulenten Reibungswiderstandes durch Oberflaechenstoerungen (Drag Due to Surface Protuberances)*, Jahrbuch D Luftfahrtforschung, 1943; or ZWB Report FB 1563.

[6] Prandtl and Betz, Ergebnisse AVA Goettingen, Vol. III, p. 82.

[7] Okamoto, *Effects of Cutting Away the Trailing Edge . . .*, Aeronautical Institute, Tokyo University, Report No. 131, 1935.

[8] Swaty, *Beeinflussung der Beizahlen des Profils 0018 durch Kuerzungen an der Hinterkante (Variation of the Characteristics of 0018 Airfoil Section Due to Cutting Off Its Trailing Edge)*, Jahrbuch D Luftfahrtforschung, p. I 58, 1940.

[9] Engelhardt, *Impulsmessungen an einem Fluegel mit veraenderlicher Hinterkantendicke (Momentum Measurements Behind a Wing with Variable Thickness of the Trailing Edge)*, Aero. Lab. Tech. University Munich, Report No. 4, 1944.

[10] Goldmann, *Widerstandsmessungen an drei Staeben (Drag Measurements on Three Rods)*, Wind-Tunnel Report Dornier No. 13, 1937.

[11] Drescher and Schwenk, *Untersuchung dicker Profile im Wasserkanal (Experiments with Thick Profiles in the Water Tunnel)*, Report AVA Goettingen No. B 44/J/17, 1944.

[12] Hoerner, *Verschiedene Messungen (Various Experiments)*, Fieseler Water-Tunnel, Report No. 2, 1939.

[13] Petrikat, *Einfluss der Hinterkantenausbildung bei Streben und Tragfluegeln (Influence of the Trailing Edge on the Characteristics of Struts and Wings)*, Fieseler Water-Tunnel Report No. 21, 1940.

[14] Junkers, *Profiles with Blunt Trailing Edges, Results from Junkers Wind-Tunnel*, No. D. 7053, 1941.

[15] Gruschwitz and Schrenk, *Ueber eine einfache Moeglichkeit zur Auftriebserhoehung von Tragfluegeln (Simple Device for Increasing Maximum Lift)*, Zeitschr Flugtechnik Motorluftsch, No. 20, 1932.

[16] Erdmann, *Widerstandsbestimmung von Kegeln und Kugeln aus der Druckverteilung bei Ueberschallgeschwindigkeit (Determination of Drag from Pressure Distribution on Cones and Spheres)*, Lilienthal Report No. 139/2, p. 28.

[17] Wenzinger and Harris, *Wind-Tunnel Investigation of N.A.C.A. 23012, 23021, and 23030 Airfoils with Various Sizes of Split Flaps*, N.A.C.A. T.R. No. 668, 1939.

[18] Charters, *Some Ballistic Contributions to Aerodynamics*, Journal of the Aeronautical Sciences, p. 155, 1947.

[19] Hill and Alpher, *Base Pressure at Supersonic Velocities*, Journal of the Aeronautical Sciences, p. 153, 1949.

[20] Ferri, *Supersonic Tunnel Tests of Projectiles in Germany and Italy*, N.A.C.A. Wartime Report L-152, 1945.

[21] Charters and Turetski, *Determination of Base Pressure from Free-Flight Data*, Ballistic Research Laboratory, Report No. 653, 1948.

Lateral-Control Devices Suitable for Use with Full-Span Flaps

FRANCIS M. ROGALLO,* JOHN G. LOWRY,† AND JACK FISCHEL‡

Langley Aeronautical Laboratory, N.A.C.A.

SUMMARY

A brief history of the development of lateral-control devices suitable for use with full-span flaps is presented with special emphasis on spoiler-type controls. Recent data on the performance of spoiler-type controls on unswept wings at high subsonic speeds and a limited discussion of spoiler controls on swept wings are included. The several advantages shown for spoiler-type controls—high lift through the use of full-span flaps, good aileron effectiveness throughout the speed range, good yawing-moment characteristics, low wing torsional loads, and the possibility of low control forces—appear to warrant their consideration for use on all types of airplanes.

Application of spoiler ailerons as air brakes while simultaneously functioning as ailerons is discussed, and their performance is shown to compare favorably with that of other currently used air brakes.

INTRODUCTION

IN 1941, THE N.A.C.A. published Baker's paper[1] covering the development of the full-span flap arrangement for the Vought Kingfisher, and, in 1946, the N.A.C.A. published a similar paper by Ashkenas[2] on the development of the full-span flap and aileron arrangement for the Northrop Black Widow. Each of these papers presented coherent stories of a particular development that was carried through to completion by a particular individual or group in a relatively short time. The N.A.C.A. story of its own work on lateral-control devices suitable for use with full-span flaps, however, covers the work of many individuals during the last 20 years. Partly because of the different points of view of these individuals but mostly because of the ever changing picture of aeronautics in general during these 20 years, the N.A.C.A. story of lateral-control devices suitable for use with full-span flaps is really several stories, not always closely connected. In fact, during part of this time the use of full-span flaps was not contemplated or was of second-order importance. Some of the devices developed, however, were found to be suitable for use with full-span flaps and are therefore included in this story.

In 1931, the N.A.C.A. began a systematic wind-tunnel investigation of lateral control with special reference to the improvement of control at low air speeds and at high angles of attack. Many different lateral-control devices were subjected to the same systematic investigation in the 7- by 10-ft. wind tunnel, and the most promising devices were tested in flight. Two of the devices developed in this program—the retractable aileron and slot-lip aileron, shown in Fig. 1—would have been suitable for use with full-span flaps.

At the outset, no high-lift flaps were used, but, after the inception of the systematic research program, flaps for the reduction of landing speed or the increase of wing loading came into general use, and the research program was modified to include lateral-control devices on wings with partial-span and full-span flaps. The effect of flap span on allowable gross weight or landing speed is indicated in Fig. 2, where it is seen that

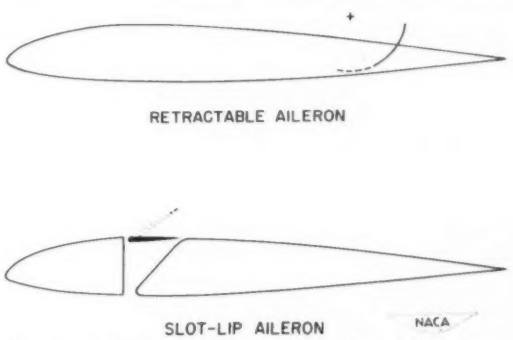

FIG. 1. Lateral-control devices on wings without flaps.

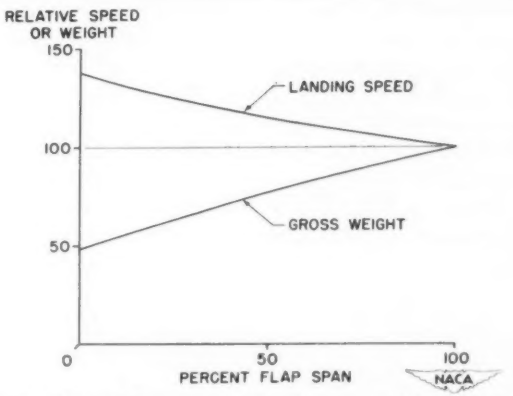

FIG. 2. Effect of flap span on allowable gross weight or landing speed.

Presented at the Aircraft Design Session, Eighteenth Annual Meeting, I.A.S., New York, January 23–26, 1950.

* Aeronautical Research Scientist, Stability Research Division.

† Aeronautical Research Scientist, Stability Research Division.

‡ Aeronautical Stability and Control Scientist, Stability Research Division.

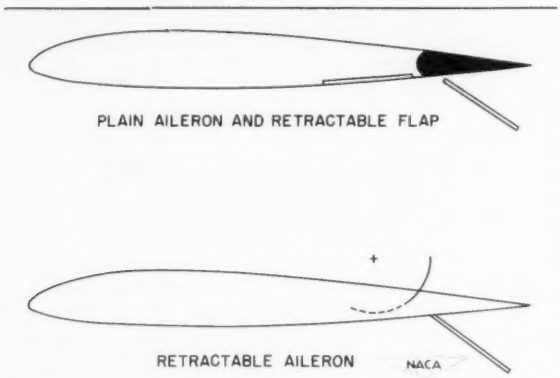

FIG. 3. Lateral-control devices on wings with full-span split flaps.

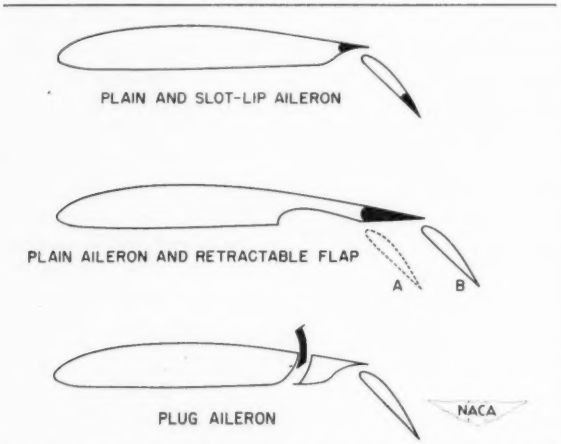

FIG. 4. Lateral-control devices on wings with full-span slotted flaps.

reducing the flap span from 100 to 50 per cent of the wing span, as might be required for conventional ailerons, would either reduce the gross weight by 22 per cent or increase the landing speed by 12 per cent. Before 1935, the plain aileron with flap retracting ahead and the retractable aileron or spoiler located at 80 per cent of the wing chord (see Fig. 3) were developed and proved in flight to be suitable for use with full-span split flaps.[3] Slotted flaps soon began to displace split flaps, however, and the program was enlarged to include such arrangements. The N.A.C.A. investigated a large number of different configurations in the 7- by 10-ft. wind tunnel[4–7] and, in 1941, recommended that the arrangements shown in Fig. 4 be flight-tested. Subsequent flight experience did not disclose any serious difficulties, and it appeared that any of these arrangements would provide satisfactory lateral control on airplanes with full-span slotted flaps.

In the work reviewed thus far, emphasis was placed on the control and performance characteristics of the aircraft at the lower end of the speed range, but, as the maximum speeds of aircraft increased, control problems were also encountered at the upper end of the speed range. The first of these was the difficulty of providing enough aerodynamic balance to keep the stick or wheel forces within the physical limits of the pilot. Although the provision of power boost was an obvious solution, the possibility of getting light forces by using a thin retractable aileron was apparent, and this arrangement was found to be satisfactory in the Northrop Black Widow night fighter.[2] The low wing torsional loads of this aileron arrangement on the Black Widow were a welcome bonus, but this characteristic was not of the major importance that it assumes when thin wings, especially those of high sweep or high aspect ratio, are used. The problem of wing twist or low aileron reversal speed has, in fact, become so great that designers are now considering the use of spoiler-type controls for the improvement of lateral control at high speed, regardless of their effect on the low-speed control or performance characteristics. That these control devices allow the use of full-span flaps may often be considered incidental, as was true in 1931 when the N.A.C.A. began the systematic investigation of such devices.

While the lateral-control research reviewed above was in progress, spoiler-type devices were also being investigated for an entirely different purpose—air brakes. This parallel line of research would have no connection with our present story if it were not for the fact that often a particular device may be used for either lateral control or air brakes. An investigation[8] has been made, moreover, of the application of spoiler-type devices as air brakes while simultaneously functioning as ailerons.

In the present paper, a brief history of the development of lateral-control devices suitable for use with full-span flaps is presented with special emphasis on spoiler-type controls. Recent information on spoiler ailerons on unswept wings, including their simultaneous use as air brakes, and a brief discussion of spoiler ailerons on swept wings are included. More complete information on all phases of the work may be found in the available references, many of which are listed.

INVESTIGATIONS ON UNSWEPT WINGS AT LOW SPEEDS

Most of the interesting low-speed test data on lateral controls for unswept wings with full-span flaps has been published by the N.A.C.A. as a collection,[9] and some discussion of results is also included in an N.A.C.A. summary of lateral-control research.[10] A large number of configurations has been investigated, and several appear to be aerodynamically satisfactory. To give an overall picture of the work, geometric and aerodynamic characteristics of the devices shown in the previous figures and problems encountered during the development of those devices will be discussed briefly. In the work leading up to the ailerons of Fig. 1, unvented spoilers located well forward on the upper

surface had prohibitive lag, but the vented or rearwardly located spoilers shown in Fig. 1 were found to have acceptable lag. It should be noted that the devices of Fig. 1 had a rather high drag because of the external hinges of the retractable ailerons and the permanently open slot of the slot-lip aileron.

The devices of Fig. 3 were concluded to be satisfactory from flight tests[3] on a Fairchild 22 airplane. A fairly complicated flap-retracting mechanism was required to allow use of the plain aileron, however, and on a larger or faster airplane some difficulties might arise from the fact that the hinge moments are greatly affected by the movement of the flap. The retractable aileron, on the other hand, had extremely small aerodynamic hinge moments regardless of flap position, but, as already mentioned, the drag of the external hinges was high. In the flap-down condition, both arrangements had yawing characteristics superior to those of plain ailerons on unflapped wings.

When the retractable aileron was modified in such a way that the hinge axis was within the wing contour (Fig. 5), an investigation in the 7- by 10-ft. tunnel[4] showed that with the split flap deflected the aileron had no effect until it was projected more than 2 per cent of the wing chord above the wing contour—a significant portion of its total projection range (see Fig. 5). Tuft studies showed that, as a result of the favorable pressure gradient established by the flap, the flow was reattaching behind the spoiler at spoiler projections less than 2 per cent wing chord. In the same investigation, a retractable aileron on a wing with a full-span slotted flap gave similar results (Fig. 5). It was found that this ineffective region could be greatly reduced by the addition of a properly shaped slot through the wing behind the spoiler.[4] To achieve this slot action during aileron operation without disruption of the wing contour with the aileron neutral, the N.A.C.A. plug aileron (see Fig. 6) was designed.[7] The powerful effect of the spoiler slot is indicated in Fig. 7, which compares the effectiveness of plug and retractable ailerons at a moderate angle of attack. The beneficial effect of the aileron slot increases with lift coefficient. The downward deflection of the aileron (Fig. 6) has little effect on the rolling and yawing moments but greatly simplifies the achievement of good stick-force or wheel-force characteristics. Ailerons of this type have undergone exhaustive wind-tunnel investigations by the N.A.C.A.[9] and have been flight-tested on several different types of airplanes. From these investigations it has been found that the maximum lift, rolling, yawing, stick-force, and wing twisting characteristics of the plug aileron and slotted flap combination are satisfactory. The principal disadvantage of the N.A.C.A. plug aileron appears to be that its installation complicates the wing structure more than a trailing-edge aileron.

To avoid the structural complication of the N.A.C.A. plug aileron, the plain and slot-lip aileron combination (see Fig. 4) was developed by the N.A.C.A.[6,11–15] and

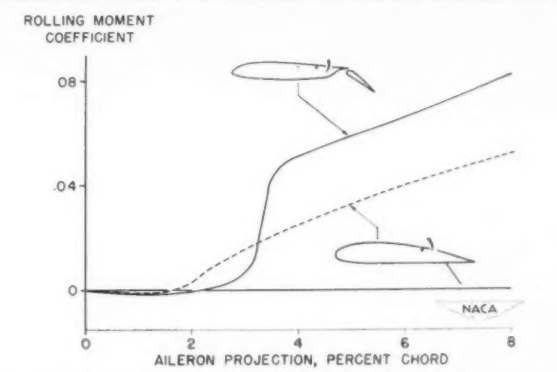

FIG. 5. Effectiveness of retractable ailerons on wings with full-span flaps.

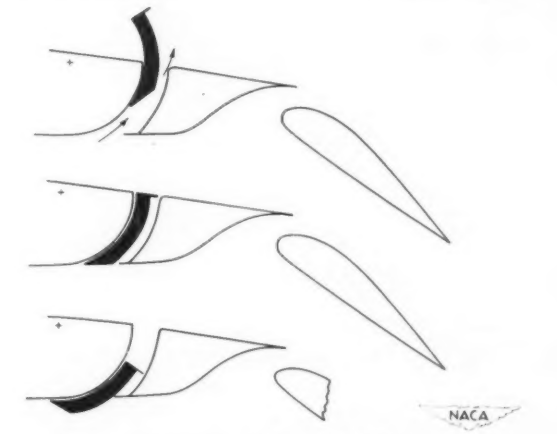

FIG. 6. Geometry of the N.A.C.A. plug aileron.

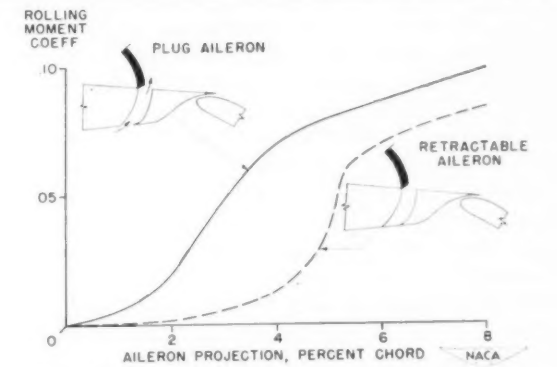

FIG. 7. Effectiveness of plug and retractable ailerons on a wing with a full-span slotted flap.

is satisfactory if one is willing to accept two separate aileron systems with a changeover from one to the other as the flap is deflected. One of these aileron systems, moreover, has restricted down-travel and high up-floating tendency, a combination that further complicates the stick-force picture.

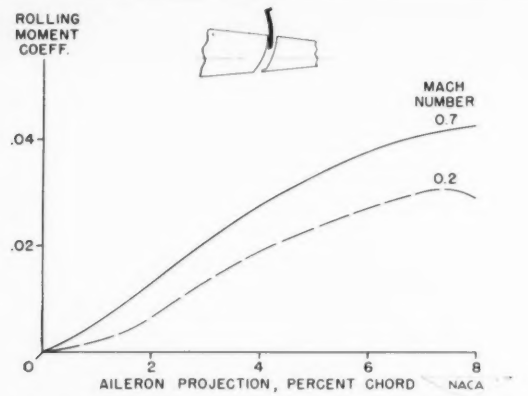

FIG. 8. Effect of Mach Number on the rolling-moment characteristics of a plug aileron on an aspect ratio 5.76 wing.

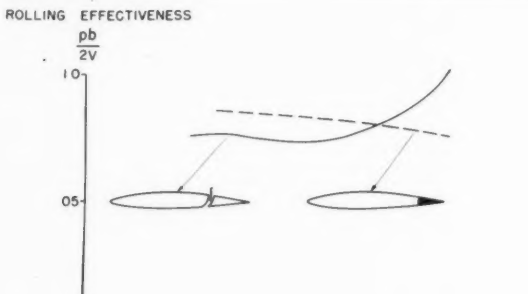

FIG. 9. Variation of rolling effectiveness with Mach Number for a plug aileron and a flap-type aileron on an aspect ratio 5.76 wing.

The plain and slot-lip aileron development by the N.A.C.A. and the Vought development of the system for the Kingfisher[1] had much in common, and the conclusions drawn are in good agreement. In addition to the development of the combination systems, incidentally, both the N.A.C.A.[16] and the Vought Company[1] investigated the possibility of utilizing the trailing-edge aileron for control with the flap at various initial settings (drooped ailerons) and found that the reduction of aileron rolling-moment coefficient and the increase of adverse aileron yawing-moment coefficient with flap deflection caused a progressive deterioration of control that became prohibitive with the flap deflected more than 20°. Although the rudder might be interconnected to offset the adverse aileron yawing moment in such a system, it seems likely that the available lateral control would decrease with reduction of airplane speed rather than increase as it may with some spoiler-type controls, a more desirable variation.

The plain aileron and retractable flap combination of Fig. 4 is another arrangement that was developed by the N.A.C.A. in an effort to retain the trailing-edge aileron while using full-span slotted flaps. Two versions of the arrangement were investigated, as indicated by flap positions A and B. When the flap-deflected condition is such that the nose of the flap is near the aileron hinge line, position A, this flap is essentially a split flap, and the characteristics of the arrangement are very much like those of the corresponding arrangement of Fig. 3. The portion of the span covered by the aileron has a high drag with the flap extended, but this drag may sometimes be tolerated if a low-drag flap, such as a Fowler[5] or an N.A.C.A. slotted flap,[17] is used inboard of the aileron. Because of the difference of flap configuration at aileron and inboard locations, this arrangement has generally been called full-span duplex flaps.

During the investigation of the duplex-flap arrangement, it became apparent that, if the flap were moved back to the wing trailing edge, position B of Fig. 4, the aileron would be a slot-lip aileron, a device already found to have good lateral-control characteristics. The flap, moreover, would then be essentially a Fowler flap, an arrangement known to have good lift and drag characteristics. Such a combination might be used over the entire wing span, resulting in some simplification relative to the duplex-flap arrangement. With these thoughts in mind, the N.A.C.A. investigated a full-span retractable flap in combination with a full-span aileron of small chord.[18,19] The arrangement was found to have good lift, drag, and control characteristics with the flap either retracted or fully extended, although a reduction of lateral control was experienced at intermediate flap positions. Obvious disadvantages of the arrangement are the required flap-supporting system and the rather high wing pitching moments resulting from flap deflection as compared with the pitching moments of other flap arrangements.[19]

From the briefly reviewed work on unswept wings at low speed, it appears that any of several different aileron arrangements will provide satisfactory control on airplanes with full-span flaps and that the choice for a given application will be determined by the overall design of the airplane and the individual preference of the designer. For high-speed airplanes, however, it will be shown that spoiler-type ailerons may have definite advantages over trailing-edge ailerons.

Investigations on Unswept Wings at High Subsonic Speeds

Because the results of any investigation of flap-type trailing-edge ailerons would be applicable in the design of full-span flap arrangements in which such ailerons are used in the flap-retracted condition (see Fig. 4), most of the high-speed investigations of devices intended specifically for use with full-span flaps have been investigations of spoiler-type ailerons.[2, 20–23] In some of these investigations, however, flap-type trailing-edge ailerons have been included for direct comparison.[24, 25]

Some investigations of spoiler ailerons at low speed have given the impression that spoiler controls located between 0.60 and 0.80 chord are ineffective at small projections in the high-speed conditions. The results of several high-speed wind-tunnel investigations,[20–22] however, show that the variation of effectiveness with projection at the higher Mach Numbers is almost linear (see Fig. 8). These high-speed investigations also showed that the spoiler-aileron effectiveness increased with increase in Mach Number (see Figs. 8 and 9) and that about the same effectiveness was exhibited at all Mach Numbers by both plug and retractable ailerons (with flap retracted). Inasmuch as spoiler ailerons also produced a linear variation of effectiveness with projection at high angles of attack and an airplane having even moderate performance characteristics would be flying at high speed at low angles of attack and at low speed at high angles of attack, it would probably have rolling characteristics that vary almost linearly with spoiler projection throughout the speed range with flap retracted. Flight-test data obtained with two spoiler-aileron arrangements on the Black Widow P-61 airplane[2, 23] (see Figs. 10 and 11) and with two spoiler-aileron arrangements on a modified Vought-Sikorsky OS2U-2 airplane,[23] in general, substantiate the wind-tunnel results. Both the flight and wind-tunnel results show that the rolling effectiveness of spoiler ailerons increased with increase in Mach Number, as contrasted to generally opposite effects obtained with flap-type ailerons (see Figs. 9 and 11).

Only recently have the high-speed hinge-moment characteristics of spoiler ailerons been reported.[20, 21] In these wind-tunnel investigations, generally the same effects and trends have been noted as were previously noted for spoiler hinge-moment characteristics at low speed[9]—namely, the hinge moments were generally somewhat irregular over the aileron projection range, varied directly as the area moment of the top edge of the aileron about the hinge axis, and could be altered somewhat by any of several possible small modifications to the aileron. As is the case with flap-type ailerons, however, power-boost systems may be used with spoiler-aileron arrangements and would obviate any necessity for special treatment of spoiler ailerons to obtain acceptable control forces.

Data obtained on the P-61 airplane[23] (Figs. 10 and 11) show that the control forces of the spoiler aileron varied smoothly and in the proper direction with spoiler projection and air speed. These data and the wind-tunnel results[20, 24] also show the small hinge moments of the spoiler controls and the small or negligible effects of Mach Number on these spoiler characteristics, in contrast to the large hinge moments of flap-type ailerons and the adverse effects of increase in Mach Number on the hinge moments of flap-type ailerons.

When considering the lateral-control characteristics of ailerons at high speeds, it is necessary to investigate

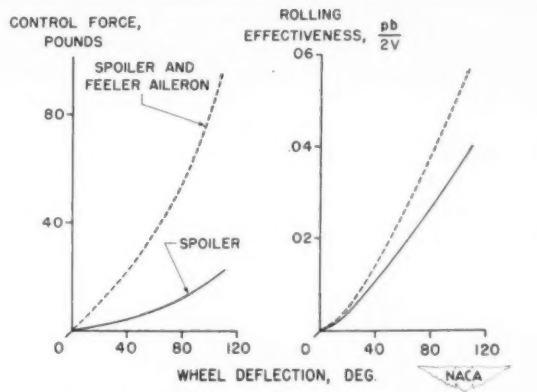

FIG. 10. Lateral-control characteristics of the P-61 airplane at an air speed of 334 m.p.h.

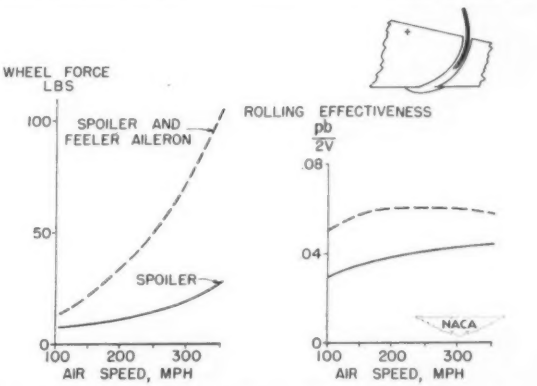

FIG. 11. Variation with air speed of the lateral-control characteristics of the P-61 airplane in the power-on, clean condition.

the wing pitching moments produced by the ailerons, because the resulting wing twist reduces the control effectiveness. For example, in an analysis of the twisting effects of flap-type ailerons on two fighter-type airplanes employed in World War II, it was found that wing flexibility was responsible for a 31 per cent loss in aileron effectiveness of one production model of the P-47 airplane and for a 65 per cent loss on the British Spitfire at an air speed of 400 m.p.h.[10]

In an investigation of the section pitching moments of flap-type and spoiler controls,[26] it was shown that, for normal spoiler-aileron locations (about 0.70 chord), the spoiler pitching moments are much less than those produced by plain flaps of equal effectiveness. The twisting effects of these control surfaces are perhaps better illustrated in Fig. 12 by a comparison of the twisting moments about an assumed wing elastic axis at 0.35 chord produced by spoiler ailerons and flap-type ailerons at high speed on an aspect ratio 5.76 wing, for which rolling-effectiveness data of the rigid wing are presented in Figs. 8 and 9. These data show that, for equal rolling effectiveness on a rigid wing, a spoiler control located at 0.70 chord produced favorable twisting moments that were relatively unaffected by

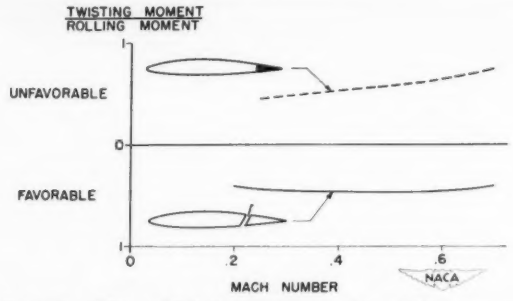

FIG. 12. Effect of Mach Number on the twisting moments (about an assumed elastic axis at 0.35 wing chord) of a flap-type aileron and a spoiler aileron on an aspect ratio 5.76 wing.

FIG. 13. Rolling effectiveness of spoilers and flap-type ailerons on swept wings.

changes in Mach Number and, on a nonrigid wing, would tend to augment the rolling effectiveness of the control, whereas a 0.20-chord plain aileron produced adverse twisting moments that became slightly larger with increase in Mach Number and would tend to reduce the aileron rolling effectiveness. These effects are such as to make the comparative rolling-effectiveness data of Fig. 9 appear even more favorable for the spoiler ailerons.

INVESTIGATIONS ON SWEPTBACK WINGS

The problems involved in designing ailerons for swept wings are the same as, but differ in magnitude and importance from, those on unswept wings. Thus, we have some or all of the following characteristics to consider: aileron effectiveness as measured by rolling moment produced by a given control on a rigid wing; variation of aileron effectiveness with speed; yawing-moment characteristics of the aileron; wing twist and the corresponding loss of aileron effectiveness; and last, but not least by far, the hinge moments of the control. Aileron effectiveness is of primary importance on both swept and unswept wings. The effects of adverse yaw and wing distortion, however, are of greater importance on thin sweptback wings than on relatively thick unswept wings, where both have often been taken care of in design calculations by a simple 0.8 factor. Thus, on swept wings either the adverse yaw effects at low speed or the wing distortion at high speed may be the determining factor in the choice of a lateral-control system. All of the factors must, therefore, be considered when laying out a new design, and no control can be discarded just because one of the characteristics is poor, for the other characteristics may outweigh this deficiency.

The lack of experience or of a reliable design procedure necessitated investigations of controls on unflapped swept wings to provide design data for the high-speed condition with little regard, as yet, for the flap-deflected condition. As a result, this discussion will be limited to the flap-retracted condition. Of the many devices already mentioned as satisfactory for use with full-span flaps (see Fig. 4), only the spoiler provides control in the flap-retracted condition by other than flap-type ailerons. Some of the characteristics of spoilers will be discussed and compared with those of flap-type ailerons.

Theoretical studies of rolling effectiveness, $pb/2V$, of flap-type ailerons on swept wings[27, 28] indicate that the rolling effectiveness for a given aileron configuration on wings of constant aspect ratio decreases with increasing sweep (Fig. 13). For comparative purposes, data from a few spoiler configurations[29, 30] are spotted on Fig. 13. Although these data are for different wing plan forms, the results indicate that spoilers of the same span as the flap-type aileron will give lower effectiveness on rigid wings at low speed and will show a more marked effect with sweep than flap-type ailerons. These adverse characteristics of spoilers may be alleviated somewhat at high speed, since unswept-wing data show that spoiler effectiveness increases more rapidly than the effectiveness of flap-type ailerons with increases in speed. Further increases in effectiveness can often be obtained by moving the spoiler inboard or by changing its alignment.[30] For example, rotating the spoiler so that it is normal to the free stream instead

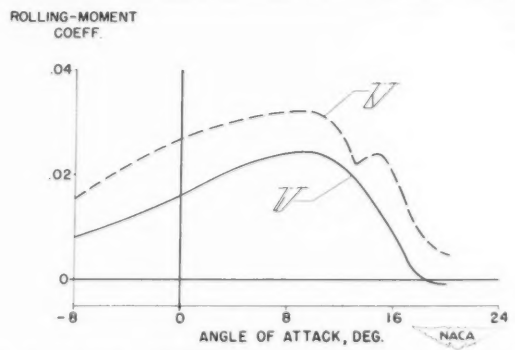

FIG. 14. Aileron effectiveness of two spoiler configurations on a 42° swept wing of aspect ratio 4.

of along a constant chord line increases the effectiveness throughout the angle-of-attack range[30] (see Fig. 14). This particular arrangement may not be the most desirable from a production point of view, but it does show what can be done by changes in spoiler location.

As was pointed out previously, the adverse yawing moments of ailerons can be detrimental to the rolling effectiveness. Studies of airplane motions[31, 32] have shown these effects to be exaggerated by large amounts of dihedral. Since sweptback wings, in general, have relatively large values of effective dihedral,[29] adverse yaw would be expected to be even more serious on sweptback wings than on unswept wings of low effective dihedral. A comparison of characteristics of a flap-type and a spoiler aileron[30] (see Fig. 15) shows that the yawing moment of the spoiler is favorable over most of the lift range and is never so adverse as that of the flap-type aileron. Since adverse yaw does, in addition to reducing the rolling effectiveness, change the airplane heading in the wrong direction, the favorable yaw over most of the lift range for the spoiler is an advantage to be considered when evaluating different aileron systems on swept wings.

The effect of elastic deformation of a sweptback wing on the rolling effectiveness is more serious than the corresponding effect on an unswept wing, since the wing bending changes the angle-of-attack distribution such as to add to the torsional deformation in reducing the rolling tendency. To further aggravate the problem of elastic deformation, some experimental results obtained on a series of untapered wings of the same span[29] (see Fig. 16) indicate increases in twisting moment with increased sweep. These results show that the twisting moments of the flap-type ailerons increase in the order of six times the value at zero sweep when the wings are swept 45°. Spoilers of the same span show the same trend, but the twisting moments are about one-third the magnitude of those shown for the flap-type ailerons. Since the data of Fig. 16 are for low speeds and the effect of twist on aileron performance becomes more serious with increasing speed, it would be desirable to see how serious these adverse twist effects would be at high subsonic speeds. To illustrate the effects, use has been made of calculations made by the U.S. Air Force.[33] In the Air Force paper, a method of estimating rolling effectiveness for elastic wings at high speeds is presented, and some sample calculations for flap-type ailerons on practical swept wings are given. Utilizing the method presented and section characteristics of spoilers,[25, 26] some calculations were made for a spoiler of the same span as the flap-type aileron and having the same effectiveness at Mach Number of 0.3. The results of these calculations, Fig. 17, show the spoilers to be considerably better than the ailerons. In fact, the spoilers lose only about 15 per cent of their effectiveness as the speed is increased to a Mach Number of 0.8, the reversal speed of the flap-type aileron. These differences in effectiveness may be more pronounced than usual because the wing aspect ratio is 9.4, but similar results, although maybe not of this magnitude, would be shown for other wings. One of the factors contributing to the performance of the spoilers is the increase in effectiveness with speed (see Fig. 9), while the effectiveness of flap-type controls, in general, shows a decrease.

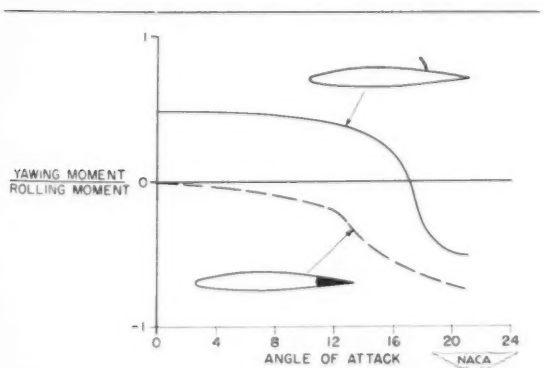

FIG. 15. Yawing-moment characteristics of spoiler and flap-type ailerons on a 42° swept wing of aspect ratio 4.

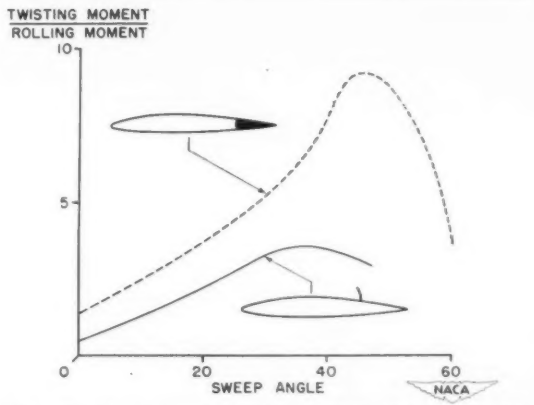

FIG. 16. Twisting moments about the 0.35 chord line for spoiler and flap-type ailerons on swept wings.

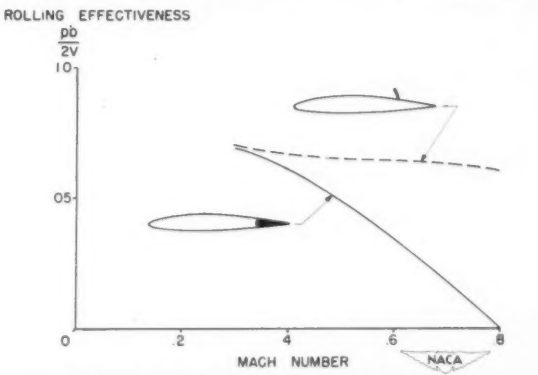

FIG. 17. Rolling effectiveness of spoiler and flap-type ailerons on an elastic 35° swept wing of aspect ratio 9.4.

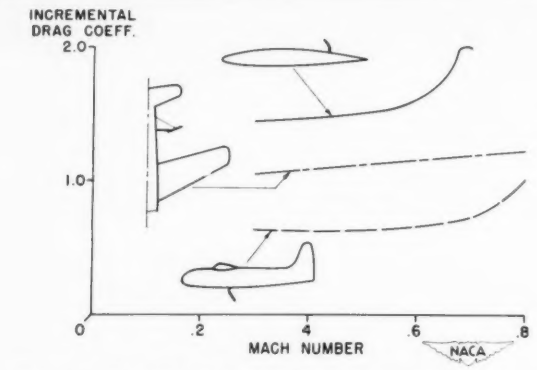

FIG. 18. Effect of Mach Number on the incremental drag coefficient due to air brakes. (Drag coefficient is based on brake area.)

Any discussion at this time of hinge moments of spoilers on swept wings and their variation with speed would be pure conjecture, since no data are available. It appears certain, however, that, if a thin circular-arc spoiler is used, the hinge moments will probably be small, since only the edges of the spoiler can produce moments about the hinge. If flap-type ailerons are used, however, the hinge-moment picture changes, and large forces might be expected.

SPOILER AILERONS USED AS AIR BRAKES

On many of the high-performance aircraft currently in operation or in the design stage, the need of suitable devices for use as aerodynamic speed brakes, glide-path controls, or both has become well recognized, and several applications of such devices to current aircraft have already been made. Speed brakes and glide-path controls are beneficial for aircraft under various normal or emergency operating conditions, such as a rapid descent from high altitude while airplane speed is being limited, reducing speed rapidly in level flight to increase firing efficiency of fighter aircraft, landing on short runways over obstacles, etc. A brief history and some of the background in the development of air brakes has been traced in a recent article,[34] and it is not the purpose of this discussion to repeat this information. However, as shown in reference 34 and the air-brake summary data in a recent N.A.C.A. publication,[35] most of the research on air brakes has been on auxiliary devices mounted on the wings of airplanes, although recently some research and employment of air brakes has been on fuselage-mounted devices. Almost a decade ago, during the course of investigating high-lift lateral-control configurations at the Langley Aeronautical Laboratory of the N.A.C.A., in order to obviate the necessity of including additional devices on the airplane, the use as speed brakes of spoiler ailerons, either alone or in conjunction with slotted flaps, was investigated at low speed and was shown to be satisfactory.[36] More recently, an investigation up to a Mach Number of 0.7 of plug and retractable ailerons for use as speed brakes or glide-path controls produced similar results,[8] and other high-speed spoiler-aileron investigations also showed the effectiveness of spoiler controls in producing drag.[22] In order to illustrate the comparative drag-producing effectiveness of several brake devices through a range of Mach Numbers, some drag data previously presented in N.A.C.A. publications[22, 35] are reproduced in Fig. 18 and show the superior drag characteristics, based on brake area, of spoiler-type devices as compared with currently used fuselage devices. Moreover, it has been shown[35] that the drag of spoiler brakes increased linearly as the brakes were extended—a much-desired characteristic.

In order to illustrate the utility and one of the advantages to be gained from the increments of drag produced by spoiler ailerons used as air brakes on an airplane, the computed descent characteristics from an altitude of 40,000 ft. of a high-performance propeller-driven airplane with and without glide-path controls, originally presented in a report of the N.A.C.A.[8] on spoiler air brakes, are reproduced in Fig. 19. The airplane had a wing loading of 63 lbs. per sq.ft., the four engines were assumed to deliver an effective thrust of zero with flap retracted, and the glide-path controls assumed for the airplane were half-span plug ailerons projected 8 per cent chord above both wings. The airplane descent was assumed to start at an altitude of 40,000 ft. and a Mach Number of 0.7, and this Mach Number was maintained until an indicated air speed of 450 m.p.h. was reached. The latter air speed was then maintained for the remainder of the descent to sea level. Fig. 19 shows that projection of the plug ailerons for use as glide-path controls appreciably decreases the time and horizontal distance required to reach sea level. This saving of time in descending from high altitudes would be particularly important for an emergency condition, such as fire or failure of cabin pressurization, and also for normal operating conditions,

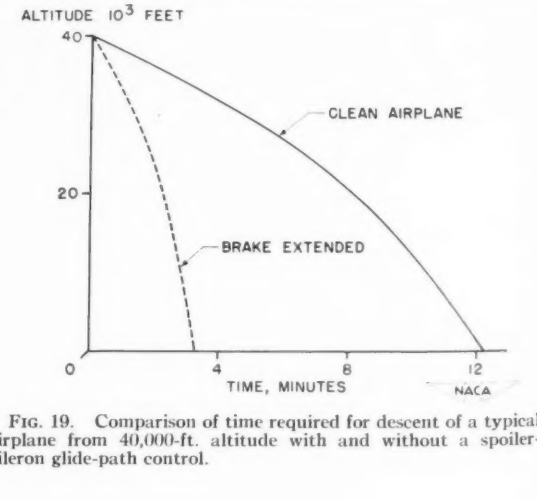

FIG. 19. Comparison of time required for descent of a typical airplane from 40,000-ft. altitude with and without a spoiler-aileron glide-path control.

such as for rapid descent from operating altitude at the termination of a long-distance flight.[37] Supplementing their action as glide-path controls, spoiler-aileron brakes provide the added advantage of decreasing wing bending moments and the possibility of wing structural failure by moving the spanwise center of loading inboard on the wings.[8]

Projection of the ailerons with the flaps deflected in a landing approach would also substantially aid the airplane in landing over high obstacles and would appreciably decrease the length of landing run.[8] The use of spoiler ailerons as speed brakes to limit or reduce airplane speed in a dive or to reduce airplane speed rapidly in order to increase firing efficiency of fighter aircraft is also feasible, as shown by spoiler-aileron drag data and performance calculations for these maneuvers.[8, 35]

Some question may arise regarding the adequacy of rolling effectiveness of the spoiler ailerons when used as glide-path controls or speed brakes. To answer that question, the rolling characteristics of spoiler ailerons from an initially projected position (as speed brakes) have been investigated and were found to compare favorably with the effectiveness of the controls from the fully retracted position.[8]

Although a detailed comparison of the characteristics of spoiler-aileron brakes and of other brake devices—beyond the comparison shown in Fig. 18—is not presented herein, several advantages of the aileron brakes are readily apparent. These advantages include: the variable braking control permitted by the aileron brakes as compared with the inflexibility of control of some of the other devices; the use of spoiler-aileron brakes would eliminate the necessity of including separate braking devices on an airplane; the aileron brakes may be used, retracted into the wing, and immediately used again, but a parachute brake, for example, can be used only once before disposal or repacking (on the ground) and is inflexible in control; and, also, the spoiler-aileron brake would not adversely affect adjoining wing controls, whereas other devices may. In addition, spoilers, when used as air brakes on unswept wings, probably would not cause tail-buffeting, inasmuch as the ailerons are placed outboard, near the tip, and the wake formed by them would be outboard of the tail surfaces.

Design Considerations

In the design of a lateral-control system, in order to compute the rolling moment produced by a control, the effective change in the angle of attack $\Delta\alpha$ (section effectiveness) produced by a given control deflection (or projection for spoiler ailerons), as well as the spanwise effectiveness, $C_l/\Delta\alpha$, of the control, must be known because the rolling-moment coefficient is the product of $C_l/\Delta\alpha$ and $\Delta\alpha$. Inasmuch as spoiler ailerons on unswept wings were found to have the same spanwise-effectiveness characteristics as flap-type ailerons,[38] the spanwise effectiveness, $C_l/\Delta\alpha$, currently used in the design of conventional ailerons[39–41] may also be used in the design of spoiler ailerons. The section effectiveness of spoiler ailerons is, however, a complex function of aileron projection, wing angle of attack, aileron geometry, chordwise location of the aileron, and the wing profile.[9] Since it is impossible to get simple design charts of spoiler effectiveness, $\Delta\alpha$, similar to those of flap-type ailerons,[39] it is necessary to use data from configurations similar to the one under study. The lack of data on spoiler controls makes it impossible to give even a preliminary design procedure for spoilers on swept wings. It is necessary, therefore, to use the available data and interpolate or extrapolate the results to encompass the proposed configuration.

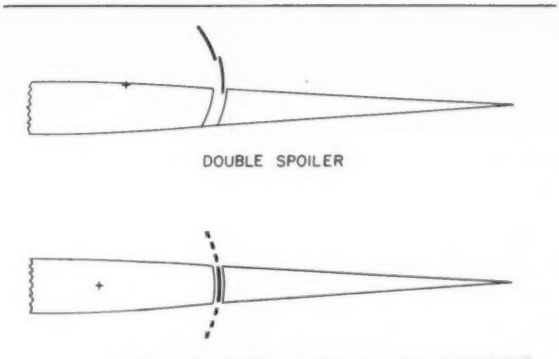

FIG. 20. Spoiler arrangements to obtain increased projection.

In addition to the aerodynamic design, it is immediately evident that it will be difficult to get sufficient projection from an internally hinged circular-arc spoiler on a thin wing. Two of the numerous solutions are shown in Fig. 20. The double spoiler retains all the advantages of spoilers by using two segments that are geared together. As shown schematically, the two segments stack within the wing and extend in the manner shown. This arrangement allows projections of about twice the wing thickness, which should, in general, be enough. Another solution requires a compromise in the yawing characteristics of spoilers but retains the advantages of low wing twist. In this arrangement, the spoiler would be able to deflect either up or down (Fig. 20). In normal operation, the spoiler on one wing would deflect through the upper surface and the spoiler on the other wing would deflect through the lower surface of the wing. In addition, this arrangement has the advantage of allowing the use of a simple linkage, since equal up and down deflections may be used.

Concluding Remarks

From the briefly reviewed work on unswept wings at low speed, it appears that any of several different aileron arrangements will provide satisfactory control

on airplanes with full-span flaps and that the choice for a given application will be determined by the overall design of the airplane and the individual preference of the designer.

For high-speed airplanes, however, it appears that spoiler ailerons have certain advantages over flap-type ailerons in that they give increased effectiveness with speed, have low hinge moments throughout the speed range, and decrease the aeroelastic problems.

From the data presented it would appear that there are no insurmountable problems associated with spoilers on thin sweptback wings.

It has been shown that spoilers can be used as air brakes while simultaneously functioning as ailerons.

References

[1] Baker, Paul S., *The Development of a New Lateral-Control Arrangement*, N.A.C.A. A.R.R., October, 1941.

[2] Ashkenas, I. L., *The Development of a Lateral-Control System for Use with Large-Span Flaps*, N.A.C.A. T.N. No. 1015, January, 1946.

[3] Soulé, H. A., and McAvoy, W. H., *Flight Investigation of Lateral Control Devices for Use with Full-Span Flaps*, N.A.C.A. T.R. No. 517, 1935.

[4] Wenzinger, Carl J., and Rogallo, Francis M., *Wind-Tunnel Investigation of Spoiler, Deflector, and Slot Lateral-Control Devices on Wings with Full-Span Split and Slotted Flaps*, N.A.C.A. T.R. No. 706, 1941.

[5] Harris, Thomas A., and Purser, Paul E., *Wind-Tunnel Investigation of Plain Ailerons for a Wing with a Full-Span Flap Consisting of an Inboard Fowler and an Outboard Retractable Split Flap*, N.A.C.A. A.C.R., March, 1941.

[6] Rogallo, Francis M., and Spano, Bartholomew S., *Wind-Tunnel Investigation of a Plain and a Slot-Lip Aileron on a Wing with a Full-Span Slotted Flap*, N.A.C.A. A.C.R., April, 1941.

[7] Rogallo, Francis M., and Swanson, Robert S., *Wind-Tunnel Development of a Plug-Type Spoiler-Slot Aileron for a Wing with a Full-Span Slotted Flap and a Discussion of Its Application*, N.A.C.A. A.R.R., November, 1941.

[8] Fischel, Jack, and Watson, James M., *Investigation of Spoiler Ailerons for Use as Speed Brakes or Glide-Path Controls on Two NACA 65-Series Wings Equipped with Full-Span Slotted Flaps*, N.A.C.A. T.N. No. 1933, August, 1949.

[9] Fischel, Jack, and Ivey, Margaret F., *Collection of Test Data for Lateral Control with Full-Span Flaps*, N.A.C.A. T.N. No. 1404, April, 1948.

[10] Langley Research Department, *Summary of Lateral-Control Research* (compiled by Thomas A. Toll), N.A.C.A. T.N. No. 1245, March, 1947.

[11] Lowry, John G., *Power-Off Wind-Tunnel Tests of the 1/8-Scale Model of the Brewster F2A Airplane*, N.A.C.A. M.R., June, 1941.

[12] Lowry, John G., *Power-On Wind-Tunnel Tests of the 1/8-Scale Model of the Brewster F2A Airplane with Full-Span Slotted Flaps*, N.A.C.A. M.R. August, 1941.

[13] Lowry, John G., *Additional Power-On Wind-Tunnel Tests of the 1/8-Scale Model of the Brewster F2A Airplane with Full-Span Slotted Flaps*, N.A.C.A. M.R., October, 1941.

[14] Lowry, John G., and Toll, Thomas A., *Power-On Longitudinal Stability and Control Tests of the 1/8-Scale Model of the Brewster F2A Airplane Equipped with Full-Span Slotted Flaps and a New Horizontal Tail*, N.A.C.A. M.R., March, 1942.

[15] Wetmore, Joseph W., and Sawyer, Richard H., *Flight Tests of F2A-2 Airplane with Full-Span Slotted Flaps and Trailing-Edge and Slot-Lip Ailerons*, N.A.C.A. A.R.R. No. 3L07, 1943.

[16] Sawyer, Richard H., *Flight Measurements of the Lateral-Control Characteristics of Narrow Chord Ailerons on the Trailing Edge of a Full-Span Slotted Flap*, N.A.C.A. T.R. No. 883, 1947.

[17] Rogallo, Francis M., and Lowry, John G., *Wind-Tunnel Investigation of a Plain Aileron and a Balanced Aileron on a Tapered Wing with Full-Span Duplex Flaps*, N.A.C.A. A.R.R., July, 1942.

[18] Rogallo, Francis M., and Lowry, John G., *Wind-Tunnel Investigation of an NACA Full-Span High-Lift Lateral-Control Combination I—Section Characteristics, NACA 23012 Airfoil*, N.A.C.A. A.R.R., July, 1942.

[19] Rogallo, Francis M., Lowry, John G., and Fischel, Jack, *Wind-Tunnel Investigation of a Full-Span Retractable Flap in Combination with Full-Span Plain and Internally Balanced Ailerons on a Tapered Wing*, N.A.C.A. A.R.R. No. 3H23, 1943.

[20] Fischel, Jack, and Schneiter, Leslie E., *High-Speed Wind-Tunnel Investigation of an NACA 65-210 Semispan Wing Equipped with Plug and Retractable Ailerons and a Full-Span Slotted Flap*, N.A.C.A. T.N. No. 1663, 1948.

[21] Fischel, Jack, *Wind-Tunnel Investigation of an NACA Semispan Wing Equipped with Circular Plug Ailerons and a Full-Span Slotted Flap*, N.A.C.A. T.N. No. 1802, 1949.

[22] Laitone, Edmund V., and Summers, James L., *An Additional Investigation of the High-Speed Lateral-Control Characteristics of Spoilers*, N.A.C.A. A.C.R. No. 5D28, 1945.

[23] Spahr, J. Richard, *Lateral-Control Characteristics of Various Spoiler Arrangements as Measured in Flight*, N.A.C.A. T.N. No. 1123, 1947.

[24] Fischel, Jack, and Schneiter, Leslie E., *High-Speed Wind-Tunnel Investigation of High Lift and Aileron-Control Characteristics of an NACA 65-210 Semispan Wing*, N.A.C.A. T.N. No. 1473, 1947.

[25] Laitone, Edmund V., *An Investigation of the High-Speed Lateral-Control Characteristics of a Spoiler*, N.A.C.A. A.C.R. No. 4C23, 1944.

[26] Purser, Paul E., and McKinney, Elizabeth G., *Comparison of Pitching Moments Produced by Plain Flaps and by Spoilers and Some Aerodynamic Characteristics of an NACA 23012 Airfoil with Various Types of Aileron*, N.A.C.A. A.C.R. No. L5C24a, 1945.

[27] Lowry, John G., and Schneiter, Leslie E., *Estimation of Effectiveness of Flap-Type Controls on Sweptback Wings*, N.A.C.A. T.N. No. 1674, 1948.

[28] Polhamus, Edward C., *A Simple Method of Estimating the Subsonic Lift and Damping-in-Roll of Sweptback Wings*, N.A.C.A. T.N. No. 1862, 1949.

[29] Letko, William, and Goodman, Alex, *Preliminary Wind-Tunnel Investigation at Low Speed of Stability and Control Characteristics of Sweptback Wings*, N.A.C.A. T.N. No. 1046, 1946.

[30] Schneiter, Leslie E., and Watson, James M., *Low-Speed Wind-Tunnel Investigation of Various Plain-Spoiler Configurations for Lateral Control on a 42° Sweptback Wing*, N.A.C.A. T.N. No. 1646, 1948.

[31] Fehlner, Leo F., *A Study of the Effect of Adverse Yawing Moment on Lateral Maneuverability at a High Lift Coefficient*, N.A.C.A. A.R.R., September, 1942.

[32] Fehlner, Leo F., *A Study of the Effects of Vertical Tail Area and Dihedral on the Lateral Maneuverability of an Airplane*, N.A.C.A. A.R.R., October, 1941.

[33] Groth, Eric, *Determination of the Rolling Effectiveness and Aileron Reversal Speed of an Elastic Wing*, U.S. Air Force, Air Materiel Command Memorandum Report MCREXA5-4595-8-10, October 7, 1949.

[34] McLarren, Robert, *Air Brakes: Standard Fighter Accessory*, Aviation Week, pp. 21–28, November 14, 1949.

[35] Stephenson, Jack D., *The Effects of Aerodynamic Brakes upon the Speed Characteristics of Airplanes*, N.A.C.A. T.N. No. 1939, 1949.

(*Continued on page 652*)

An Initial Approach to the Overall Structural Problems of Swept Wings Under Static Loads

E. E. SECHLER,* M. L. WILLIAMS,† AND Y. C. FUNG‡

California Institute of Technology

ABSTRACT

For the past 2½ years, under the sponsorship of the Air Materiel Command of the U.S. Air Force, GALCIT has been investigating the subject of the stresses in thin swept wings. The investigation has utilized theoretical, experimental, and electrical agencies on this problem. The problem has been reduced to a form amenable to theoretical analysis by assuming the wing replaced by a thin cantilever plate of uniform thickness.

A theoretical solution of a thin cantilever plate of rectangular cross section with varying angle of sweep has been obtained. Expansion of the deflection in terms of the normal modes of vibrating bars is employed, the coefficients being determined by the Rayleigh-Ritz method. Experimental data for both stress and deflection are also presented. An approximate solution yielding the qualitative behavior of the stresses in such plates is included.

The equations and circuits for the use of the electrical analog type of solution of plate problems are indicated, and a comparison is made between theoretical, experimental, and analog data, the latter being obtained by the use of a twelve-point electrical network.

INTRODUCTION

EARLY IN 1947, THE STRUCTURES GROUP at GALCIT became interested in swept-wing design, and, through the cooperation and financial assistance of the Aircraft Laboratory of the Air Materiel Command, the initial effort and thought on this problem has been magnified in both theoretical and experimental directions. While it was deemed advisable to restrict the investigation to static loadings and postpone aeroelastic and flutter considerations until a later date, the scope of the program was, nevertheless, quite broad and included theoretical solutions for idealized wing structures of high solidity, with special emphasis upon stress and deflection variation with sweep angle, and experimental data for a scale model of a typical wing. It was desired to compare these latter data with theoretical results if they were obtainable and, if not, to have sufficient data to represent adequately the phenomena taking place. As an added objective, the effects of taper in plan form and thickness were to be investigated. Finally, a study of existing design methods being employed in the aircraft industry was to be made.

Presented at the Structures Session, Eighteenth Annual Meeting, I.A.S., New York, January 23–26, 1950.

* Professor, Guggenheim Aeronautical Laboratory.

† Lecturer, Guggenheim Aeronautical Laboratory.

‡ Research Fellow, Guggenheim Aeronautical Laboratory.

It should be stated immediately, however, that the answers to all the questions posed in the contemplated program have not been obtained, although it is believed that satisfactory progress has been made. To date, four reports pertaining mostly to the introductory work have been submitted, and it is anticipated that several additional ones will be completed in the near future.

An exploratory study of possible simplifying assumptions necessary to reduce the swept aircraft wing to an idealized structure amenable to rigorous mathematical treatment, while still retaining the essential characteristics of the problem, was made by C. B. Ling, many of whose observations are included herein. Several modes of attack were proposed, but each one was essentially reduced to the study of a thin cantilever plate of constant thickness for a given plan form. For example, some of the idealized forms originally suggested were a rectangle, parallelogram, triangle, skew parabola or ellipse, and sector.

THE IDEALIZED WING

While it is not the purpose of this paper to discuss at length the reasons for choosing the idealized wing to be a thin plate of constant thickness (this matter is covered elsewhere[1]), it is apparent that the assumption of a thin wing is justifiable on the basis of the aspect and thickness ratios used on current high-speed aircraft. On the other hand, the chord cross section is not necessarily constant or solid, although in the high solidity wings being investigated the structural section is approximately rectangular. Aside from this, the mathematical complications introduced by a variable thickness plate were too involved to consider at this stage. Finally, thin plate theory is fairly well established, and extensive background material exists in the literature.

The wing has thus been replaced by a thin (cantilever) plate of uniform thickness under a normal loading. According to standard plate theory, a mathematical boundary value problem can be formulated as one in which the deflection function $w(x, y)$ is to be found from the solution of a fourth-order partial differential equation

$$\nabla^4 w(x, y) = \frac{\partial^4 w}{\partial x^4} + 2\frac{\partial^4 w}{\partial x^2 \partial y^2} + \frac{\partial^4 w}{\partial y^4} = \frac{q}{D}$$

for a given plan form where part of the boundary is clamped and part is free.

Except for certain isolated cases, exact solutions to the problem are difficult to obtain. The problems of the circular and rectangular plate with simply supported boundary conditions are relatively simple and were solved early in the nineteenth century. The solution for the rectangular plate with clamped edges is considerably more difficult and was solved during the latter part of the same century. When "mixed" boundary conditions corresponding to some edges free and some edges fixed are imposed upon the problem of the rectangular plate, the solution becomes much more elusive, although two authors have arrived at essentially the same solution independently[1, 2] using energy methods.

Approximate Solutions

The exact solution of the problem in question is generally difficult in the sense that such a solution is usually intractable mathematically. Presumably, the problem would be made easier if one or more of the conditions to be satisfied were relaxed. Suppose, for instance, that the condition of satisfying the differential equation exactly is relaxed and, instead, an alternate condition—namely, the condition of minimum energy—is added. Under such less stringent requirements, a system of functions can often be found which satisfies the so-called "rigid" boundary conditions only.* The resulting solution is then expressed as a linear combination of the system of these functions, and the arbitrary constants associated with the functions are adjusted to satisfy the condition of minimum energy. The minimizing process presents no special difficulty mathematically. This method is the well-known Rayleigh-Ritz energy method.

It may be noted that in this method the boundary value problem outlined previously is, in fact, substituted by a variational problem. Such a change in the nature of a problem usually serves to provide a lead to a solution originally intractable.

* The "rigid" boundary conditions are those not derivable from the corresponding variational integral, such as the imposed specific edge deflections or slopes. On the other hand, those derivable from the variation of the energy integral are called the "natural" boundary conditions, to which belong the imposed specific edge moments and reactions. In the Rayleigh-Ritz method, only the rigid boundary conditions must be satisfied by the constituent solutions. The natural boundary conditions will be satisfied in the limit as a result of the variational procedure.

The energy in a thin plate is given by the following integral:

$$V = \frac{1}{2}\int\int_R D\left\{[\nabla^2 w]^2 - 2(1-\nu)\left[\frac{\partial^2 w}{\partial x^2}\frac{\partial^2 w}{\partial y^2} - \left(\frac{\partial^2 w}{\partial x\,\partial y}\right)^2\right]\right\} dx\,dy - \int\int_R qw\,dx\,dy + \int M_n \frac{\partial w}{\partial n}\,ds - \int\left(Q_n - \frac{\partial H_{nt}}{\partial S}\right) w\,ds$$

where the double integration extends over the entire region R of the plate and the last two line integrals are extended over the free edges of the plate. The first integral represents the total strain energy stored in the plate, while the others represent the amount of work done by the external loading acting on the plate.

If the elementary solutions are infinite in number and form a *complete* system in the mathematical sense, the solution found by the Rayleigh-Ritz method is exact in the limit. Otherwise, the solution obtained is *approximate*. Such approximation is usually deemed necessary in order to simplify the actual calculation difficulties. By properly choosing the set of functions, the results are usually substantially correct, even though only the first few functions of the system are used.

If each of such functions belongs to an *orthogonal* system, great simplification will result when minimizing the energy integral. In the procedures used in reference 1, the constituent solutions are chosen as the products of two systems of vibration modes of a bar of uniform cross section with suitable end conditions. In this manner, certain orthogonality relations are utilized to facilitate the computations. To be explicit, the deflection surface is assumed to be of the form

$$w(x, y) = \sum_{m,\,n}^{\infty} a_{mn}\, w_{mn}(x, y)$$

where

$$w_{mn}(x, y) = f_m(x)\, g_n(y)$$

In this expression, $f_m(x)$ is the mth free vibration mode of a thin elastic bar of length L, clamped at the end $x = 0$, and free at the end $x = L$; $g_n(y)$ is the nth mode of a bar of length a with both the ends $y = \pm a/2$ free. For rectangular plates, x is the spanwise dimension measured from the root, and y is the chordwise dimension measured from the mid-chord. For swept plates (x, y) are replaced by the oblique coordinates (ξ, η).

Upon substituting $w(x, y)$ in this form into the energy expression, the first variation of the energy may be taken with respect to the coefficients a_{mn}. On equating this first variation to zero, a doubly infinite number of equations in the same number of unknowns are obtained; these, in general, cannot be solved. An approximation is made by arbitrarily taking only the first few terms. Assuming rapid convergence of the series that was satisfactory for the cases investigated (of

the order of ten terms), the a_{mn} can be obtained and the approximate deflection function determined. This work has been carried out in detail, including tabulated values for necessary calculations and complete procedural steps for both the swept and unswept rectangular plate.[3]

It may happen that the solution is still intractable even after relaxing the differential equation. Alternately, a solution may be constructed which satisfies the differential equation but leaves some of the boundary conditions imperfectly satisfied. The latter procedure is usually described as the Trefftz method. In this procedure, the arbitrary constants involved in the solution are adjusted such that the line integral taken around the whole boundary—or the square of the error arising due to imperfectly satisfying the boundary conditions—becomes a minimum. This implies, in fact, that the solution thus obtained is the best solution obtainable under the circumstances.

A procedure applying this method to the deflection of a rectangular cantilever plate under static loading, using the elementary solutions of the plate equation in rectangular coordinates, in the form of products of trigonometric and hyperbolic functions, has been worked out.[1] The actual calculation is laborious and the convergency rather uncertain. Another example, which is unpublished, using the elementary solutions in polar coordinates (for plates with a sector plan form), in the form of products of a polynominal or logarithmic function and a trigonometric function, also indicates slow unsatisfactory convergence. Thus, the effectiveness of the Trefftz procedure, though well demonstrated for harmonic equations (such as the torsion problem), is not readily extended to problems involving biharmonic equations of the cantilever plate. In this connection, one may reflect that, in the former case, many exact solutions are obtained directly as elementary solutions, while, in the cantilever plate case, no exact solution is known expressible as such simple elementary solutions in finite terms. Hence, before some special functions particularly suitable to the cantilever plate are demonstrated, the relaxation of boundary conditions may be regarded as impractical except in isolated cases.

It is to be observed that in all the preceding solutions, exact as well as approximate, the general procedure followed is to find the deflection function first and then to derive the stress from the deflection function. As the stress is at least a second differential coefficient of the deflection function, any error introduced in the deflection function, either inherently or accidently, would be magnified in the stress expression. Since it is the stress that is of primary concern in practical design, one naturally prefers to estimate the stress directly, instead of indirectly, from the deflection.

For this purpose, the compatibility conditions of the plate may be relaxed in order to find a system of solutions which satisfies the equations of equilibrium and the boundary conditions of imposed external tractions. To choose among the infinite number of solutions the one that solves the problem, the complementary energy theorem (or in particular cases with suitable boundary conditions, the Castigliano theorem) is applied so as to minimize the total strain energy in the plate. The result thus obtained will give a direct approximation to the stresses.

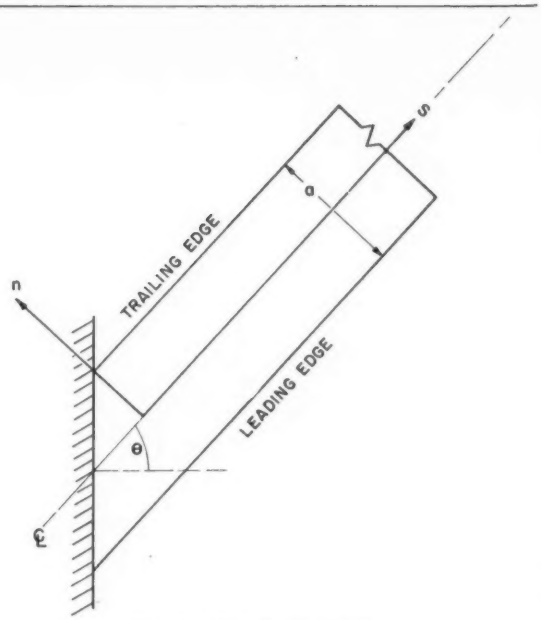

FIG. 1. Coordinate system.

Such a direct method, systematically developed by introducing some stress functions,[1] however, is still too lengthy to be elegant. A different formulation of the plate problem using stress functions suitable for the cantilever plate problem, to be solved by the relaxation method, is more attractive. This will be mentioned in the last section of this paper concerning future work. In these procedures, stresses are obtained by a single differentiation of the stress functions, instead of the second and third derivatives of the deflection function.

A Simplified Analysis of the Stresses in Swept Plates

A simplified analysis,[3] aiming at an approximate prediction of the stresses in a cantilever swept plate, is based on the complementary energy method. A swept cantilever plate of fairly large aspect ratio and of the practical thickness ratio is usually regarded as a simple cantilever beam. In such plates, the stress pattern differs appreciably from that given by the simple beam analysis only in the neighborhood of the clamped edge. To take the effect of sweep into account, the simple beam analysis is modified by introducing two parameters into a system of solutions which satisfies the equations of equilibrium but modifies the stress distribution

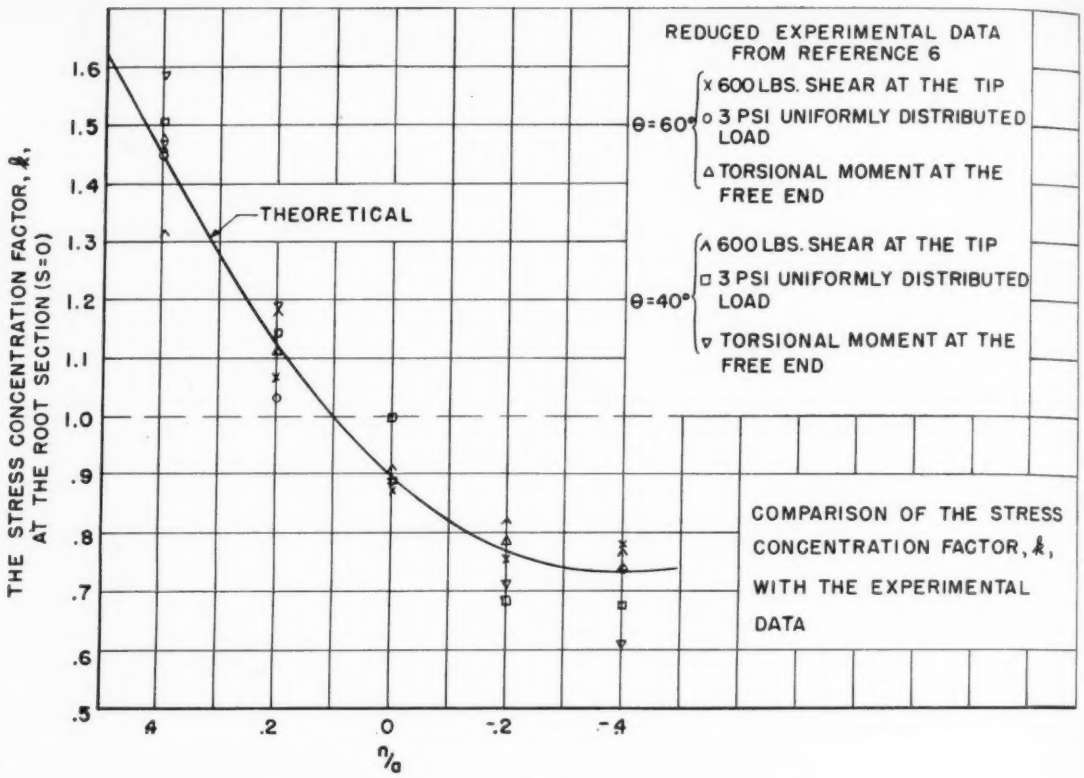

FIG. 2.

near the clamped edge. The parameters are determinable by minimizing the strain energy integral. Let

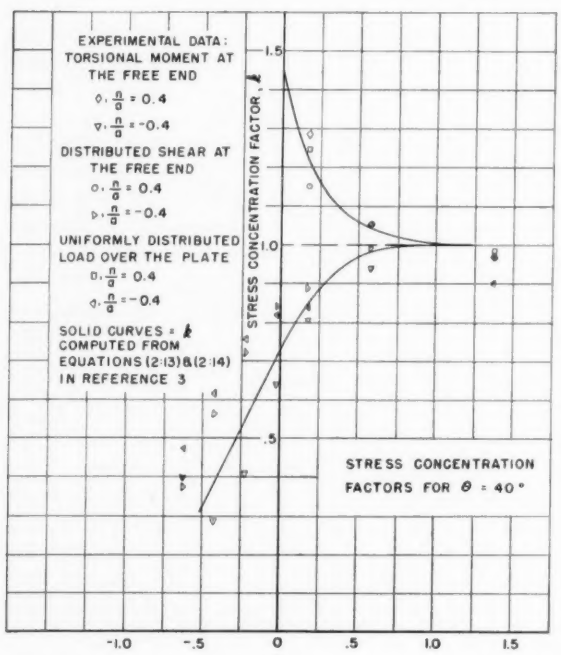

FIG. 3.

a set of rectangular coordinates (s, n) be introduced, with the s-axis coinciding with the center line of the plate and the n-axis passing through the inner corner of the root of the plate (see Fig. 1). Let us define a "stress concentration factor" as the ratio of the maximum local principal stress to the average stress at a section. The average bending and torsional moment being defined as the total bending or torsional moment at a section (s = constant) divided by the chord length, the average bending and torsional stresses are computed accordingly. When $s = 0$—i.e., in the section where the trailing edge ($n/a = 0.5$) intersects the clamped edge—the stress concentration factor plotted against n/a is a single curve for all sweep angles. Hence, the stress concentration factor near the re-entrant corner of the clamped edge is almost independent of the angle of sweep. At definite n/a, the stress concentration factor gradually changes into the uniform value of 1 when s/a increases. The root effect is quickly damped out when the sweep angle is small and is more slowly damped out when the sweep angle is large. Fig. 1 shows the coordinate system used in this analysis. Fig. 2 shows the comparison of the stress concentration factor k with the experimental data, at the root section $s = 0$, plotted across the chord. Fig. 3 shows the comparison with the experimental data, for a swept plate with 40° sweep, of the stress concentration factors along the 10 per cent chord line (from the leading edge) and along the 90 per

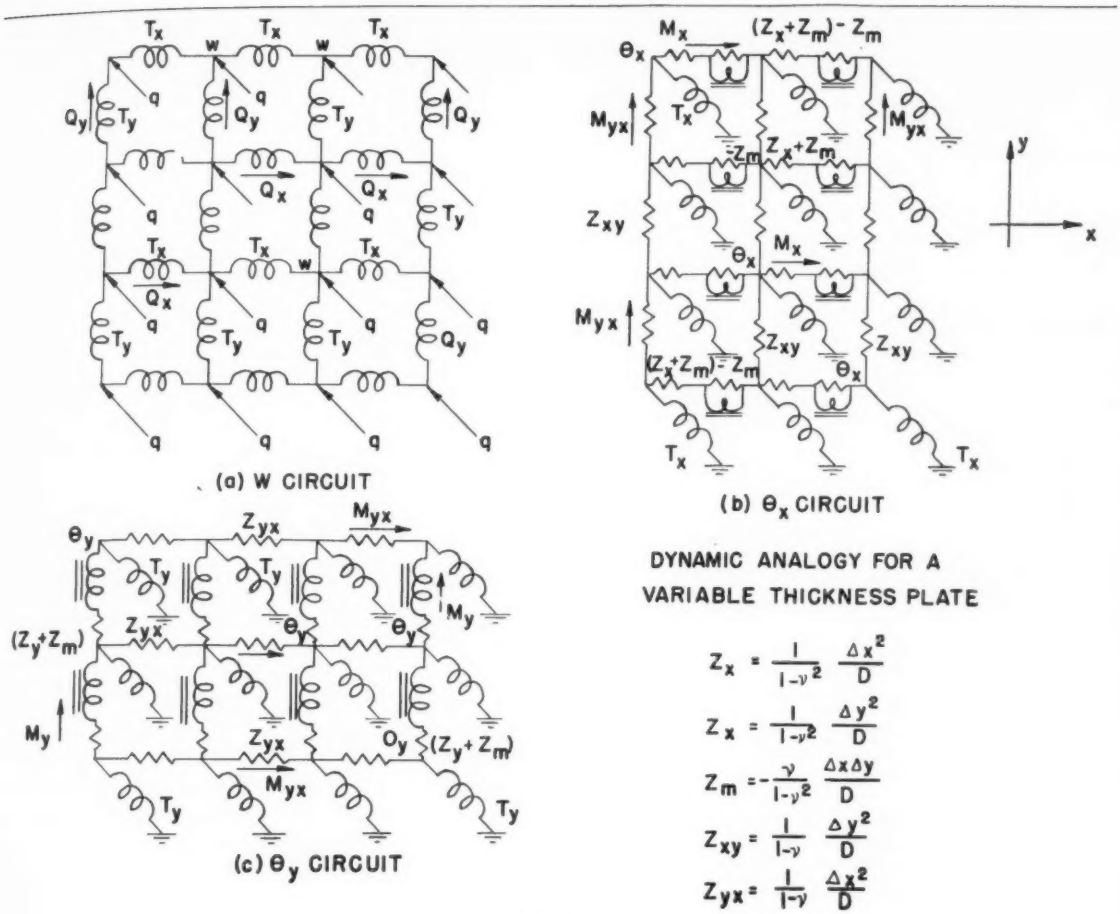
(a) W CIRCUIT
(b) Θ_x CIRCUIT
(c) Θ_y CIRCUIT
DYNAMIC ANALOGY FOR A VARIABLE THICKNESS PLATE
$Z_x = \frac{1}{1-\nu^2}\frac{\Delta x^2}{D}$
$Z_x = \frac{1}{1-\nu^2}\frac{\Delta y^2}{D}$
$Z_m = -\frac{\nu}{1-\nu^2}\frac{\Delta x \Delta y}{D}$
$Z_{xy} = \frac{1}{1-\nu}\frac{\Delta y^2}{D}$
$Z_{yx} = \frac{1}{1-\nu}\frac{\Delta x^2}{D}$

FIG. 4.

cent chord line. It shows the damping of k to the limiting value of unity as s/a increases. In the root sector (ABC in Fig. 1), the stresses decrease quickly as the distance from the re-entrant corner is increased.

These conclusions cannot be regarded as quantitatively accurate. However, they offer a simple picture of the stress distribution in a swept plate.

THE USE OF ELECTRICAL ANALOGIES

Aside from the application of direct mathematical methods for solving plate problems, the use of electric analogies has also been investigated by means of the Electric Analog Computer in the Analysis Laboratory. It has been found possible to devise an electric circuit consisting only of passive elements, including transformers, which is suitable for dynamic and transient studies as well as for the calculation of static load deflections. Furthermore, plates of varying thickness and irregular plan form present no basic difficulty.

In this approach, deflections and slopes are analogous to voltages, while the shears and bending moments are represented by currents. It should be noted that, inasmuch as all the physical quantities desired may be measured directly, an inherent advantage is apparent over the straight mathematical approach in which the stresses are obtained by two differentiations with a resultant loss in accuracy. The network used, applicable for variable thickness plates, is given in Fig. 4, while the representation of clamped, supported, free, and elastically constrained edges are worked out in reference 5. As a matter of record, it may be mentioned that a convenient list of finite difference equivalents, useful for plate work in general and electrical analogies in particular, has been prepared by the Defense Research Laboratory.[4]

Because of the limited number of high-quality transformers available, it was possible to represent only twelve points of a finite difference network. With this limitation, solutions were obtained for the following specimens: (1) simply supported rectangular plate, (2) rectangular plate clamped on all edges, (3) cantilever rectangular plate, and (4) swept cantilever rectangular plate.

The results obtained appear satisfactory considering the few number of points available in the network, al-

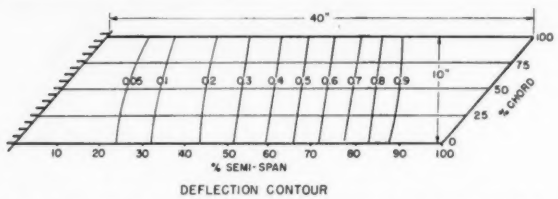

FIG. 5. 24 ST aluminum plate specimen of uniform 1-in. thickness swept back 40°, with a normal shear force of 600 lbs. uniformly distributed along the tip. NOTE: Deflection in inches.

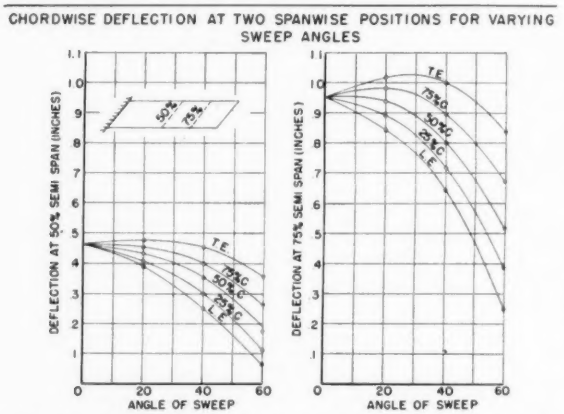

FIG. 6. 24 ST aluminum plate specimen of uniform 1-in. thickness swept back 40°, with a normal shear force of 600 lbs. evenly distributed along the tip.

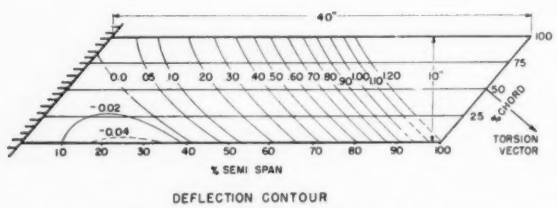

FIG. 7. 24 ST aluminum plate specimen of uniform 1-in. thickness swept back 40°, with a 45,000-in.lb. torque applied perpendicular to the tip. NOTE: Deflection in inches.

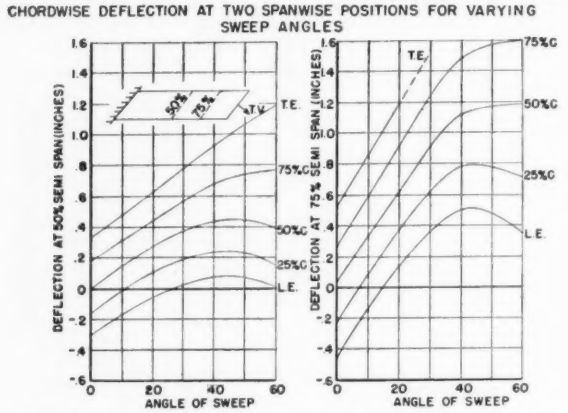

FIG. 8. 24 ST aluminum plate specimen of uniform 1-in. thickness swept back 40°, with a 45,000-in.lb. torque applied perpendicular to the tip.

though the work is not being continued because of lack of equipment. Additional information in much greater detail than included herein is furnished in reference 5.

EXPERIMENTAL INVESTIGATION

While it was not part of the original purpose to enter into an extensive experimental investigation of the stresses and deflections in swept wings or the idealized structure, it was thought advisable to obtain enough data to check any proposed theoretical solution. Also, should particular phases of the analysis prove intractable, it was desired to have at hand sufficient experimental data to admit of a qualitative understanding of the plate behavior and perhaps even furnish semi-empirical design formulas based, for instance, upon beam theory—or, alternately, show the magnitude of the beam theory approximation.

For these reasons, therefore, a fairly careful experimental program was planned, and subsequently carried out, primarily upon a plate specimen of 24 ST, whose dimensions outside of the support in the unswept position were 50 by 10 by 1 in. In addition to its unswept position, the plate was tested at various aspect ratios and several angles of sweep up to 60°. Strain gage rosettes were liberally placed over the surface of the plate upon which a rectangular grid had been inscribed. It was thus possible to record both stress and deflection readings for all sweep angles tested. In general, three different types of loadings were used: uniformly distributed, concentrated tip, and tip torque load.

Without going into detail regarding the technique or apparatus used in the experimental setup, the accuracy of the measurements may be summarized with respect to the stress and deflection data. For the former, it is believed that the overall error is within ±5 per cent, with approximately half of this figure due to possible zero drift of the readings. Accuracy of the deflection data cannot be quoted too easily in percentage because of the small deflections near the root. In this region, care was taken to hold the measurements ±0.003 in., but further outboard a deviation of ±0.005 in. was allowed since here the percentage error was small.

In the report covering this phase of the investigation,[6] the deflection data were presented in the form of contours. For the most part, the data confirmed earlier qualitative ideas regarding the deflection pattern over the plate and furnished the qualitative information. A typical deflection contour for the case of a 40° swept plate under a uniformly distributed shear at the tip is given in Fig. 5, while the variation of deflection with sweep angle at two spanwise positions is given in Fig. 6 for the same loading. Similar curves are presented in Figs. 7 and 8 for the case of a pure torque applied at the tip of the plate.

In keeping with the desire to present primarily a factual report,[6] it was decided to present the strain gage data in terms of principal stress direction and magnitude

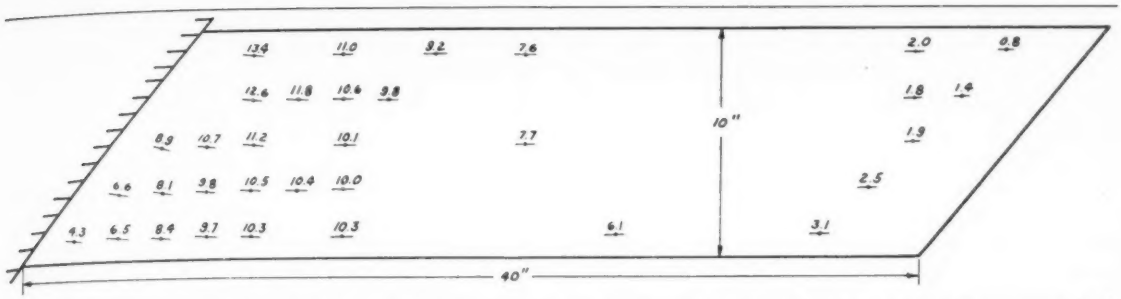

FIG. 9. Directions and magnitudes of principal stress. 24 ST aluminum plate specimen of uniform 1-in. thickness swept back 40°, with a normal shear force of 600 lbs. uniformly distributed along the tip. NOTE: Solid lines at gage points indicate directions of principal stress; the numbers indicate magnitude in kips.

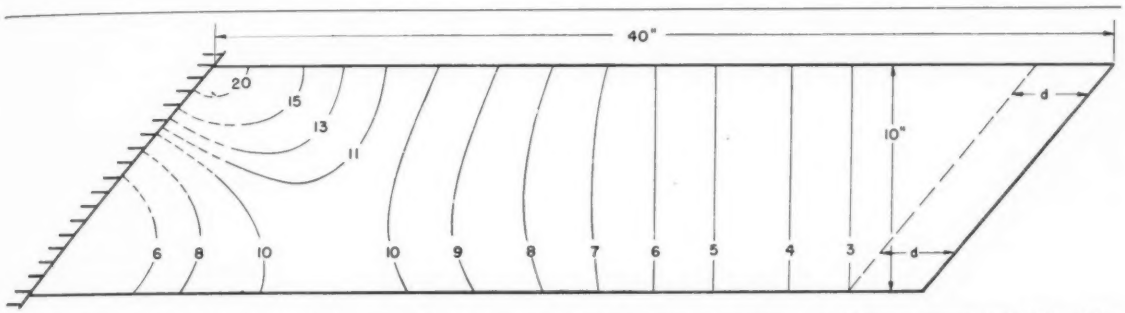

FIG. 10. Contour of maximum principal stress. 24 ST aluminum plate specimen of uniform 1-in. thickness swept back 40°, with a normal shear force of 600 lbs. uniformly distributed along the tip. NOTE: The numbers indicate magnitude in kips.

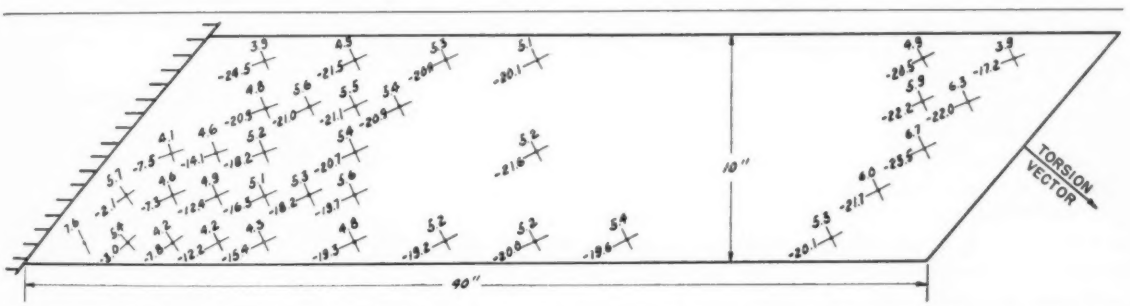

FIG. 11. Directions and magnitudes of principal stress. 24 ST aluminum plate specimen of uniform 1-in. thickness swept back 40°, with a 45,000-in.lb. torque applied perpendicular to the tip. NOTE: Solid lines at gage points indicate directions of principal stress; the numbers indicate magnitude in kips.

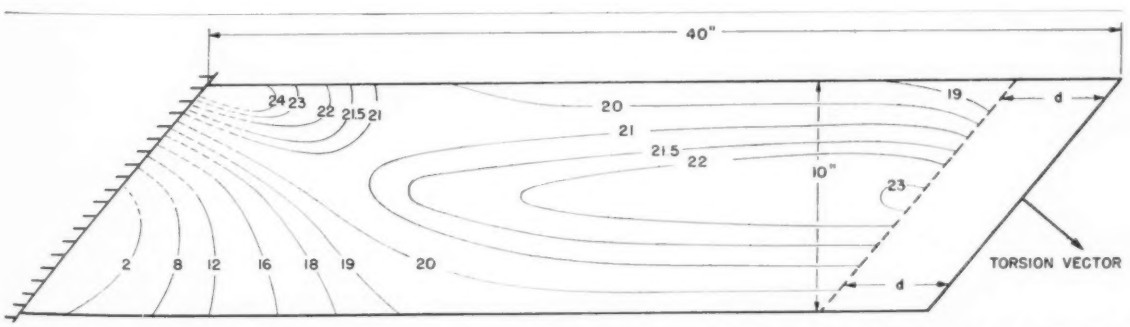

FIG. 12. Contour of maximum principal stress. 24 ST aluminum plate specimen of uniform 1-in. thickness swept back 40°, with a 45,000-in.lb. torque applied perpendicular to the tip. NOTE: The numbers indicate magnitude in kips.

at the points where the gages were located. As one example, Fig. 9 shows the data as recorded for the case of a 40° swept plate under the tip shear load. The stress data may also be cross-plotted and presented in the form of contours of maximum principal stress magnitude, as has been done in Fig. 10. Here, it should be added that additional root stress data have been used in order to extend the contours to the fixed edge. It is believed that contours of this type, coupled with the known theoretical knowledge of the direction of the principal stress, will prove to be of the most value, since one's intuitive feeling of stress concentrations is borne out by the pattern of the contours in the vicinity of the reentrant corner. Similar stress data for the torque loading are given in Figs. 11 and 12.

In some respects, the stress data are more interesting than the deflection data, although one's point of view is, of course, influenced by the use to which the data will be put. From the strength point of view, consideration of the stresses will be the more important, and, since there are so many ways one may wish to cross-plot stress variations with sweep angle, no attempt has been made to do so, leaving the matter to those interested. In concluding the remarks upon this experimental work it should be briefly noted that the root stress variations with sweep, being possibly of the greatest interest, have been made the subject of a separate theoretical and experimental investigation, results of which are not ready for presentation at this time.

Future Work

As was indicated earlier, the work upon this program is still under way, and it is appropriate to conclude this paper with some remarks relative to work in progress. First of all, relaxation methods have been under consideration for some time, with applications to triangular and sector plan forms and plates of variable thickness, because of the considerable amount of experimental and theoretical work already completed upon the cantilever sector plate. Also, some numerical examples for low aspect ratio, swept rectangular plates and hollow, thick-walled, boxlike sections are contemplated. Then, finally, some experimental data are being accumulated for a swept box beam with thick cover plates. As work on various phases of this project is completed, additional reports will be prepared under the same Air Force Technical Report number—namely, AF-TR-5761.

One of the more important parts of this swept-wing program pertains to a design method analysis wherein it is hoped that a correlation between practical design and mathematical theory can be achieved. While the study of plates may lead far afield from the complex wing structures in present-day use, it is nevertheless an advantage to treat one example—even a limiting case—in a rigorous fashion and thus provide at least one check upon the analysis or approximation. In order to carry out this design study, GALCIT, with the cooperation of the Air Materiel Command and other Government agencies, has requested aircraft companies and research organizations to provide reports and references upon the subject. Their assistance in this undertaking is greatly appreciated.

Conclusions

The purpose of this paper has been to outline, in general terms, the problems not yet solved and some of the methods of solution that have been tried. Inasmuch as four formal reports have already been submitted upon the preliminary phases and are available for the detailed study of those interested in this problem, it was thought more relevant to outline briefly their content and indicate how they fit into the broad integrated program than to try and cover the detailed mathematics of specific analyses.

References

[1] Fung, Y. C., *Theoretical and Experimental Effect of Sweep Upon the Stress and Deflection Distribution in Aircraft Wings of High Solidity. Part I—Elastostatic and Aeroelastic Problems Relating to Thin Wings of High Speed Airplanes*, AFTR 5761, August, 1948.

[2] Young, D. H., *Application of Ritz's Energy Method to Problems in the Vibration, Buckling and Bending of Rectangular Plates*, Defense Research Laboratory DRL-209, April 30, 1949.

[3] Fung, Y. C., *Theoretical and Experimental Effect of Sweep Upon the Stress and Deflection Distribution in Aircraft Wings of High Solidity. Part II—Stress and Deflection Analysis of Swept Plates*, AFTR 5761-2, June, 1949.

[4] Barton, M. V., *Finite Difference Equations for the Analysis of Thin Rectangular Plates with Combinations of Fixed and Free Edges*, Defense Research Laboratory DRL-175, August 6, 1948.

[5] MacNeal, R. H., *Theoretical and Experimental Effect of Sweep Upon the Stress and Deflection Distribution in Aircraft Wings of High Solidity. Part IV—Application of the Electric Analog Computer to the Elastic Plate Problem*, AFTR 5761-4, June, 1949.

[6] DeGroff, H. M., *Theoretical and Experimental Effect of Sweep Upon the Stress and Deflection Distribution in Aircraft Wings of High Solidity. Part III—Experimental Investigation of the Effect of Sweep Upon the Stress and Deflection Distribution in Cantilever Plates of Constant Chord and Thickness*, AFTR 5761-3, June, 1949.

Transient Loading of Supersonic Rectangular Airfoils*

JOHN W. MILES†

University of California at Los Angeles

SUMMARY

The results of earlier papers are used to calculate the lift and moment coefficients for a rectangular airfoil that experiences a sudden change in angle of attack (without rotation) in an otherwise uniform supersonic stream or which enters a sharp-edged gust. The results are valid when the Mach lines from the leading-edge corners do not intersect the opposite side edges. Numerical results are given in the form of curves.

(1) INTRODUCTION

THE INDICIAL ADMITTANCE of a system is defined as its response to a step function excitation. In the present situation, it is desired to calculate the pressure distribution along a spanwise strip x of a rectangular airfoil due to an angle of attack along a second spanwise strip ξ, which has the value zero before $t = t_0(\xi)$ and unity thereafter. This result, which is essentially the Green's function for the problem, may then be used to find the response of the airfoil to an excitation that has an arbitrary distribution in space and time.

NOTATION

A.R. = aspect ratio (ratio of span to chord)
C_L = lift coefficient, Eq. (2.10)
C_M = moment coefficient, Eq. (2.11)
J_0 = Bessel function, first kind, zero order
M = Mach Number (ratio of free-stream velocity to sonic velocity)
U = free-stream velocity
T = time required to reach steady state, Eq. (4.3)
a = indicial admittance, Eqs. (2.7), (3.4), and (3.6)
f = chordwise velocity distribution, Eq. (2.3)
k = Green's function for harmonic excitation, Eq. (2.2)
m = $(M - 1)/M$
n = $(M + 1)/M$
p = gage pressure
t = time
t_0 = time at which disturbance arises at point ξ, Eq. (2.5)
w = $(x - \xi)/U(t - t_0)$
x = chordwise coordinate (Fig. 1)
α = downwash angle (Fig. 1)
β = $(M^2 - 1)^{1/2}$
γ = dimensionless pressure, Eqs. (2.8) and (2.9)
δ = Dirac delta function, Eq. (2.4)
ϵ = small, positive, real constant, Eq. (2.5b)
θ = Mach angle ($\sin^{-1} 1/M$, Fig. 1)
ξ = running value of x
ρ = air mass density
τ = dimensionless time, Eq. (4.4)
ω = angular frequency

The indicial admittance for the two-dimensional supersonic airfoil has been obtained by several writers[1–5] through a variety of approaches. The method to be used in the present analysis is that of reference 4, wherein the indicial admittance was determined from the transfer function—which is to say that the response to a step function excitation was obtained from the response to a harmonic excitation. This method is chosen principally because of the availability of the latter result[6] but also because of the pedagogic emphasis that it places on the equivalence of the two results, either of which may be used to analyze arbitrary distributions of the excitation in time, by virtue of the Duhamel and Fourier methods of superposition, respectively, for linearized systems.

(2) STATEMENT OF PROBLEM

The chordwise (gage) pressure distribution—i.e., the force per unit chord acting on a spanwise strip at x—on a rectangular airfoil of aspect ratio A.R., leading edge

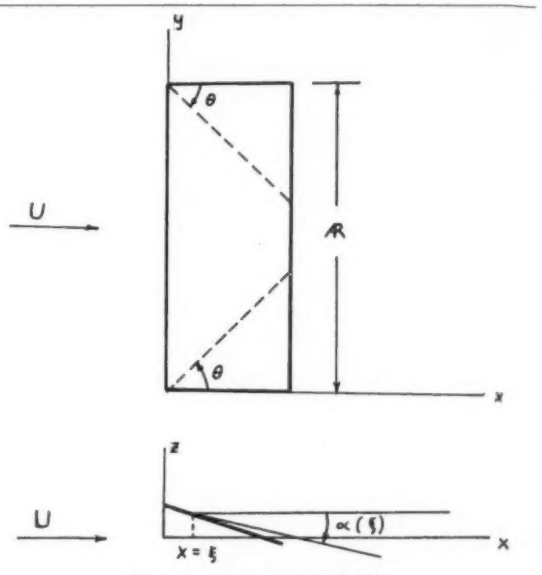

FIG. 1. Rectangular airfoil.

Received September 28, 1949.

* The author wishes to thank Irven Naiman, of the Aerodynamics Section, USNOTS, for his assistance in editing and checking the manuscript and in supervising the computation and preparation of the graphs.

† Associate Professor of Engineering. Also, Consultant, U.S. Naval Ordnance Test Station, Inyokern, Calif.

$x = 0$, and trailing edge $x = 1$ in a supersonic flow directed along the positive x axis with velocity U and Mach angle θ (Mach Number, $M = \csc\theta$), as shown in Fig. 1, due to a downwash *angle* distribution

$$\alpha(\xi, t) = \alpha(\xi) \exp(i\omega t)$$

is given by[6]

$$p(x, t) = -\left(\frac{\rho U^2}{\beta}\right)\int_0^x k(x-\xi)\alpha(\xi, t)d\xi \quad (2.1)$$

$$k(x) = k_0(x) - (\beta\text{A.R.})^{-1}k_1(x) \quad (2.2a)$$

$$k_0(x) = \delta(x-\xi) + \left(\frac{\partial}{\partial x} + \frac{i\omega}{U}\right)\times \left[\exp\left(\frac{-i\omega M^2 x}{\beta^2 U}\right) J_0\left(\frac{\omega M x}{\beta^2 U}\right)\right] \quad (2.2b)$$

$$k_1(x) = \left(\frac{\partial}{\partial x} + \frac{i\omega}{U}\right)\times \left[\left(\frac{\beta^2 U}{\omega M}\right)\exp\left(\frac{-i\omega M^2 x}{\beta^2 U}\right)\sin\left(\frac{\omega M x}{\beta^2 U}\right)\right] \quad (2.2c)$$

$$\beta = (M^2 - 1)^{1/2} \quad (2.3)$$

$$\lim_{\epsilon \to 0^+}\int_{x-\epsilon}^{x+\epsilon}\delta(x-\xi)d\xi = 1 \quad (2.4)$$

where J_0 is Bessel's function of the first kind and order zero and $\delta(x-\xi)$ is the Dirac delta function. The unit of length is taken as the chord of the airfoil, the notation having been slightly modified from that of references 4 and 6. The result is linearized and holds only when the Mach lines from the leading-edge corners do not intersect on the wing. The latter restriction is met by demanding the inequality $\beta\text{A.R.} \geq 2$, although it can be shown[6] that the final results for the lift and moment coefficients are valid provided only that $\beta\text{A.R.} \geq 1$, which implies that the aforementioned Mach lines do not intersect the opposite wing edges.

The downwash distribution to be considered is given by

$$\alpha(\xi, t) = f(\xi)\,\mathbf{1}[t - t_0(\xi)] \quad (2.5a)$$

$$= \frac{f(\xi)}{2\pi}\lim_{\epsilon \to 0^+}\int_{-\infty}^{\infty} d\omega(\epsilon + i\omega)^{-1}\exp[i\omega(t - t_0)] \quad (2.5b)$$

$\mathbf{1}(t - t_0)$ is the Heaviside step function, and Eq. (2.5b) introduces its Fourier representation in the ω spectrum. This distribution is introduced in Eq. (2.1), and the pressure may be expressed in the form

$$p(x, t) = -\left(\frac{\rho U^2}{\beta}\right)\int^x a[x - \xi\ t - t_0(\xi)]f(\xi)d\xi \quad (2.6)$$

$$a(x, t) = a_0(x, t) - (\beta\text{A.R.})^{-1}a_1(x, t) \quad (2.7a)$$

$$a_{0,1}(x, t) = \frac{1}{2\pi}\lim_{\epsilon \to 0+}\int_{-\infty}^{\infty} d\omega\,(\epsilon + i\omega)^{-1}k_{0\ 1}(x)\exp(i\omega t) \quad (2.7b)$$

The function $a[x - \xi, t - t_0(\xi)]$ is defined as the indicial admittance of the airfoil and gives the (dimensionless) pressure at station x due to a downwash increment at station ξ, which vanishes for time earlier than $t_0(\xi)$ and has the magnitude $f(\xi)$ for time later than $t_0(\xi)$. The first term, a_0, gives the two-dimensional response, and the second term, a_1, gives the defect in the three-dimensional response, relative to its two-dimensional value, due to induction effects. Since the two-dimensional problem has been solved previously,[1-5] it suffices herein to consider the three-dimensional effects, as described by a_1.

In the remainder of this paper it will be convenient to make the pressure dimensionless by writing

$$p(x, t) = -(\rho U^2/\beta)\gamma(x, t) \quad (2.8)$$

$$\gamma(x, t) = \gamma_0(x, t) - (\beta\text{A.R.})^{-1}\gamma_1(x, t) \quad (2.9a)$$

$$\gamma_{0,1}(x, t) = \int_0^x a_{0,1}[x - \xi, t - t_0(\xi)]f(\xi)d\xi \quad (2.9b)$$

The problem to be solved may now be posed as: Given $f(\xi)$, find $\gamma_1(x, t)$; this problem has been reduced to two successive quadratures, as indicated by Eqs. (2.7) and (2.9).

While some applications may require a direct knowledge of the pressure over the airfoil, the lift and moment coefficients are generally the items of principal interest. The increments in these coefficients are given by

$$-\delta C_L(t) = (\rho U^2/2)^{-1}\int_0^1 [-2p_1(x, t)]dx \quad (2.10a)$$

$$= (4/\beta^2\text{A.R.})\int_0^1 \gamma_1(x, t)\,dx \quad (2.10b)$$

$$-\delta C_M(t) = (\rho U^2/2)^{-1}\int_0^1 [-2p_1(x, t)](1/2 - x)dx \quad (2.11a)$$

$$= -\frac{1}{2}\delta C_L - \left(\frac{4}{\beta^2\text{A.R.}}\right)\int_0^1 x\gamma_1(x, t)\,dx \quad (2.11b)$$

The moment coefficient is taken about the mid-chord, and the reference moment arm is the chord ($= 1$).

(3) Indicial Admittance

Consider first the integration of Eq. (2.7b), assuming that reversing the order of the integrations with respect to ξ and ω is justifiable, which may be verified a posteriori. Carrying out the indicated differentiation in Eq. (2.2c) and substituting in Eq. (2.7b) yields

$$a_1(x, t) = (1/2\pi)\lim_{\epsilon \to 0+}\int_{-\infty}^{\infty}(\epsilon + i\omega)^{-1}\times \exp\left[i\omega\left(t - \frac{M^2 x}{\beta^2 U}\right)\right]\times \left[\cos\frac{\omega M x}{\beta^2 U}\right) - \left(\frac{i}{M}\right)\sin\left(\frac{\omega M x}{\beta^2 U}\right)\Big]\,d\omega \quad (3.1)$$

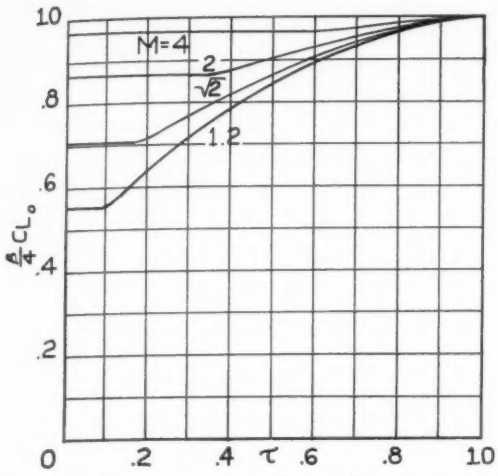

FIG. 2. Two-dimensional lift coefficient for sudden (unit) change in angle of attack.

If the trigonometric functions in Eq. (3.1) are replaced by their exponential equivalents, the result may be written

$$a_1(x, t) = \frac{1}{4\pi} \lim_{\epsilon \to 0+} \int_{-\infty}^{\infty} (\epsilon + i\omega)^{-1} \times \left\{ m \exp\left[i\omega \left(t - \frac{x}{nU} \right) \right] + n \exp\left[i\omega \left(t - \frac{x}{mU} \right) \right] \right\} d\omega \tag{3.2}$$

$$m = (M - 1)/M \tag{3.3a}$$

$$n = (M + 1)/M \tag{3.3b}$$

The integrals may be directly interpreted as step functions [cf., Eq. (2.5)], whence

$$a_1(x, t) = \frac{m}{2} \mathbf{1}\left(Ut - \frac{x}{n} \right) + \frac{n}{2} \mathbf{1}\left(Ut - \frac{x}{m} \right) \tag{3.4}$$

It is evidently convenient to introduce the single variable (x/Ut) and restate Eq. (2.9) in the form

$$\gamma_1(x, t) = \int_0^x a_1 \left\{ \frac{x - \xi}{U[t - t_0(\xi)]} \right\} f(\xi) d\xi \tag{3.5}$$

$$a_1(w) = 0, \quad w < 0 \tag{3.6a}$$

$$= 1, \quad 0 \leq w \leq m \tag{3.6b}$$

$$= m/2, \quad m \leq w \leq n \tag{3.6c}$$

$$= 0, \quad w \geq n \tag{3.6d}$$

(4) Sudden Change in Angle of Attack

The simplest transient problem of practical interest is the sudden change of angle of attack (without rotation) over the entire wing. [Physically this might arise from a suddenly imposed, vertical (downward) velocity, but the primary value of the solution is as a basis for Duhamel integration.] Consider, therefore, the downwash distribution [cf. Eq. (2.5)],

$$f(\xi) \equiv 1 \tag{4.1a}$$

$$t_0(\xi) \equiv 0 \tag{4.1b}$$

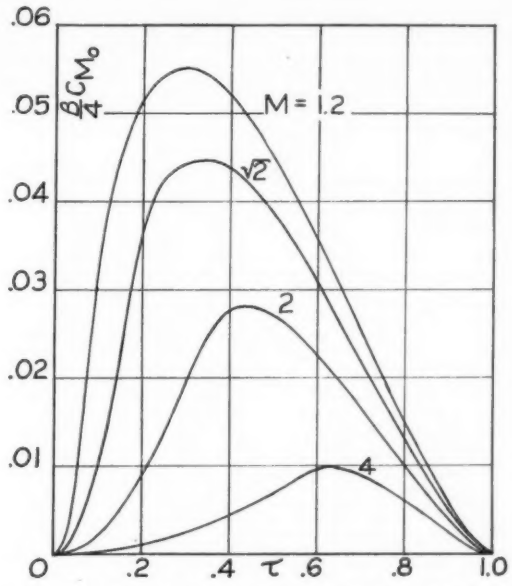

FIG. 3. Two-dimensional moment coefficient for sudden (unit) change in angle of attack.

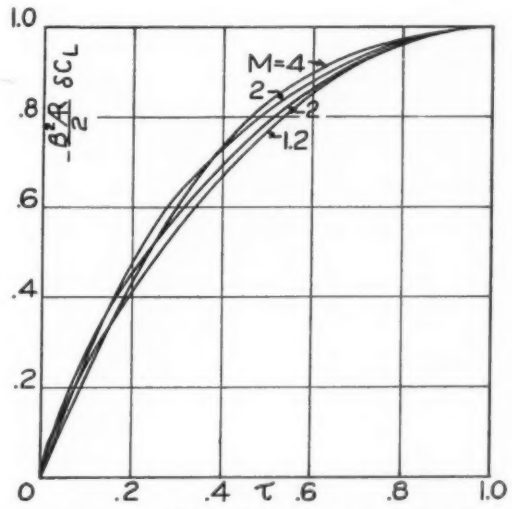

FIG. 4. Increment of lift coefficient due to induction effects for sudden (unit) change of angle of attack.

for which Eq. (3.4) reduces to

$$\gamma(x, t) = \int_0^x a_1 \left(\frac{x - \xi}{Ut} \right) d\xi \tag{4.2}$$

It is evident that the steady-state pressure will exist over the entire airfoil $(0 < x < 1)$ after a time T given by

$$T = M \times (\text{chord})/(M - 1)U \tag{4.3}$$

and it is convenient to introduce the dimensionless time parameter

$$\tau = (t/T) = m\ Ut = [(M - 1)/M]\, Ut \tag{4.4}$$

By substituting the indicial admittance from Eq. (3.5), Eq. (4.2) yields

$$\gamma_1(x, t) = x, \quad x \leq \tau \tag{4.5a}$$

$$= \frac{m}{2} x + \frac{n}{2} \tau, \quad \tau \leq x \leq (n/m)\tau \tag{4.5b}$$

$$= n\tau, \quad x \geq (n/m)\tau \tag{4.5c}$$

The lift and moment coefficients due to the pressure distribution [Eq. (4.5)] are given by Eqs. (2.10) and (2.11). Adding to these results the two-dimensional coefficients of reference 4 (allowing for the differences in notation), it is found that

$$\frac{\beta}{4} C_L = (mn)^{1/2} - (2\beta \text{A.R.})^{-1} \left[2n\tau - \left(\frac{n}{m}\right)\tau^2 \right], \quad \tau \leq \frac{m}{n} \tag{4.6a}$$

$$= \frac{1}{\pi} \cos^{-1} [M(1 - n\tau)] + \frac{(mn)^{1/2}}{\pi} \cos^{-1} \left[M \left(1 - \frac{m}{\tau}\right) \right] + \frac{1}{\pi} (2n\tau - n^2\tau^2 - mn)^{1/2} - (2\beta \text{A.R.})^{-1} \times \left[\frac{m}{2} + n\tau - \frac{n}{2}\tau^2 \right], \quad \frac{m}{n} \leq \tau \leq 1 \tag{4.6b}$$

$$= 1 - (2\beta \text{A.R.})^{-1}, \quad \tau \geq 1 \tag{4.6c}$$

$$\frac{\beta}{4} C_M = \frac{m^{-3/2} n^{1/2} (1 - m)^2}{4} \tau^2 + (12\beta \text{A.R.})^{-1} \left[3 \left(\frac{n}{m}\right) \tau^2 - 2 \left(\frac{n}{m^2}\right) (2 - 2m + m^2) \tau^3 \right], \quad \tau \leq \frac{m}{n} \tag{4.7a}$$

$$= \frac{m^{-3/2} n^{1/2} (1 - m)^2}{4\pi} \tau^2 \cos^{-1} \left[M \left(1 - \frac{m}{\tau}\right) \right] + \frac{1}{4\pi} \left(1 - \frac{\tau}{m}\right) (2n\tau - n^2\tau^2 - mn)^{1/2} + (12\beta \text{A.R.})^{-1} \left(\frac{m}{2} + \frac{3n}{2} \tau^2 - n\tau^3 \right), \quad \frac{m}{n} \leq \tau \leq 1 \tag{4.7b}$$

$$= (12\beta \text{A.R.})^{-1}, \quad \tau \geq 1 \tag{4.7c}$$

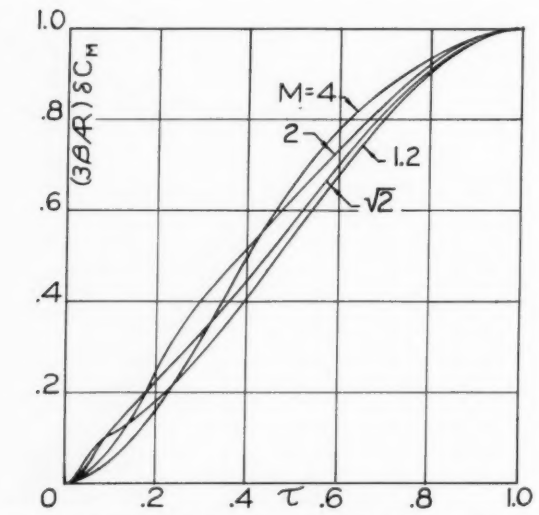

FIG. 5. Increment of moment coefficient due to induction effects for sudden (unit) change of angle of attack.

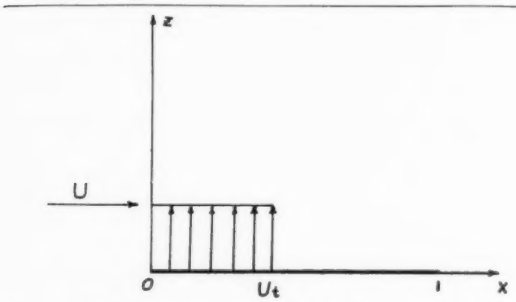

FIG. 6. Velocity distribution on airfoil at time t after entering sharp-edged gust.

The two-dimensional results C_{L_0} and C_{M_0}, as taken from reference 4, are plotted in Figs. 2 and 3. The three-dimensional increments δC_L and δC_M, defined in

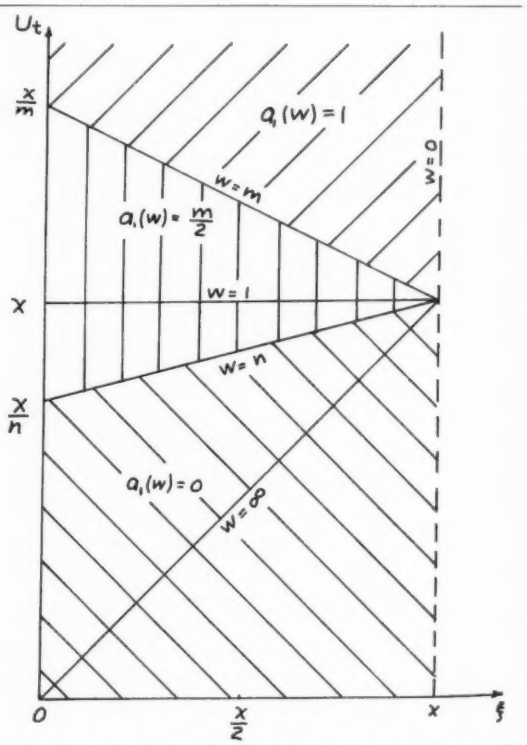

FIG. 7. Ut vs. ξ, as given by Eq. (5.3b), and $a_1(w)$, as given by Eq. (3.5).

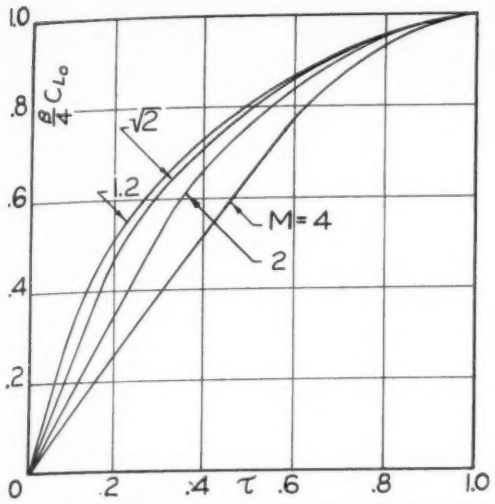

FIG. 8. Two-dimensional lift coefficient for uniform (unit) gust entry.

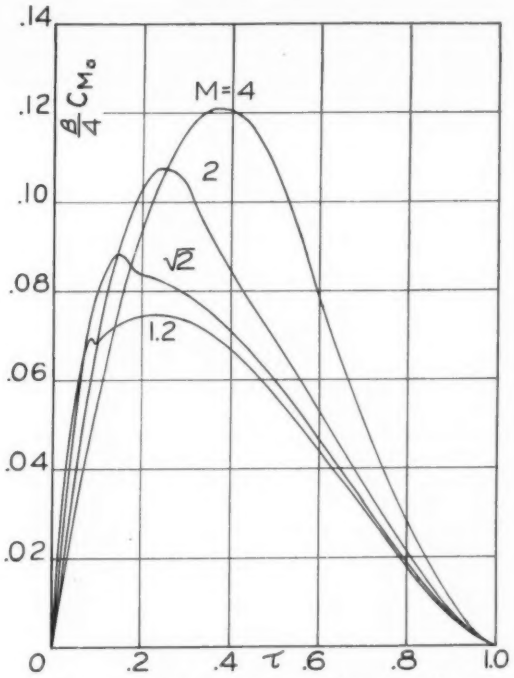

FIG. 9. Two-dimensional moment coefficient for uniform (unit) gust entry.

accordance with the relations

$$C_L = C_{L_0} + \delta C_L \tag{4.8a}$$
$$C_M = C_{M_0} + \delta C_M \tag{4.8b}$$

are plotted in Figs. 4 and 5.

(5) Gust Loading

A second special case of practical importance is the entry of the airfoil into a sharp-edged gust. In this case, the downwash distribution, which is depicted in Fig. 6, is given by Eq. (2.5), where

$$f(\xi) \equiv 1 \tag{5.1a}$$
$$Ut_0(\xi) \equiv \xi \tag{5.1b}$$

and Eq. (3.5) reduces to

$$\gamma_1(x, t) = \int_0^x a_1\left(\frac{x-\xi}{Ut-\xi}\right) d\xi \tag{5.2}$$

In carrying out the integrations in Eq. (5.2), it is expedient to examine the behavior of w in the (Ut, ξ) plane—viz.,

$$w = (x-\xi)/(Ut-\xi) \tag{5.3a}$$
$$Ut = [x + (w-1)\xi]/w \tag{5.3b}$$

Eq. (5.3b) represents a one-parametric family of straight lines, the lines of dominant importance being shown in Fig. 7, together with the domains of $a_1(w)$ which they delineate.

Carrying out the integration indicated by Eq. (5.2) with the aid of Fig. 6 yields

$$\gamma(x, t) = x, \quad x \le \tau \tag{5.4a}$$
$$= \frac{1}{2}\left(\frac{m}{m-1}\right)x + \frac{1}{2}\left(\frac{n}{n-1}\right)\tau, \quad \tau \le x \le \frac{n}{m}\tau \tag{5.4b}$$
$$= 0, \quad x \ge (n/m)\tau \tag{5.4c}$$

Adding the results of substituting this result [Eq. (5.4)] in Eqs. (2.10) and (2.11) to the two-dimensional lift and moment coefficients of reference 4* yields

$$\frac{\beta}{4}C_L = \left(\frac{n}{m}\right)^{1/2}\tau - (2\beta\text{A.R.})^{-1}\left(\frac{n}{m}\right)\tau^2, \quad \tau \le \frac{m}{n} \tag{5.5a}$$
$$= \frac{1}{\pi}\cos^{-1}[M(1-n\tau)] + \frac{1}{\pi}\left(\frac{n}{m}\right)^{1/2}\tau\,\cos^{-1}\left[M\left(1-\frac{m}{\tau}\right)\right] - (2\beta\text{A.R.})^{-1}M\left(-\frac{m}{2} + n\tau - \frac{n}{2}\tau^2\right),$$
$$m/n \le \tau \le 1 \tag{5.5b}$$
$$= 1 - (2\beta\text{A.R.})^{-1}, \quad \tau \ge 1 \tag{5.5c}$$

* Eq. (28b) of reference 4 should have contained an additional factor of $1/\pi$ in the last term, for which reason Fig. 6 therein is incorrect.

$$\frac{\beta}{4} C_M = \frac{1}{2}\left(\frac{n}{m}\right)^{1/2} \tau \left(1 - \frac{\tau}{m}\right) + (12\beta \text{A.R.})^{-1}\left[-3\left(\frac{n}{m}\right)\tau^2 + 4\left(\frac{n}{m^2}\right)\tau^3\right], \quad \tau \leq \frac{m}{n} \tag{5.6a}$$

$$= \frac{1}{2\pi}\left(\frac{n}{m}\right)^{1/2} \tau \left(1 - \frac{\tau}{m}\right) \cos^{-1}\left[M\left(1 - \frac{m}{\tau}\right)\right] + \frac{1}{2\pi}\frac{\tau}{m}(2n\tau - n^2\tau^2 - mn)^{1/2} +$$

$$(12\beta \text{A.R.})^{-1} M\left[-\frac{m}{2} + \left(\frac{3n}{2}\right)\tau^2 - n\tau^3\right], \quad \frac{m}{n} \leq \tau \leq 1 \tag{5.6b}$$

$$= (12\beta \text{A.R.})^{-1}, \quad \tau \geq 1 \tag{5.6c}$$

The results of Eqs. (5.5) and (5.6) are plotted in Figs. 8–11, in accordance with Eqs. (4.8).

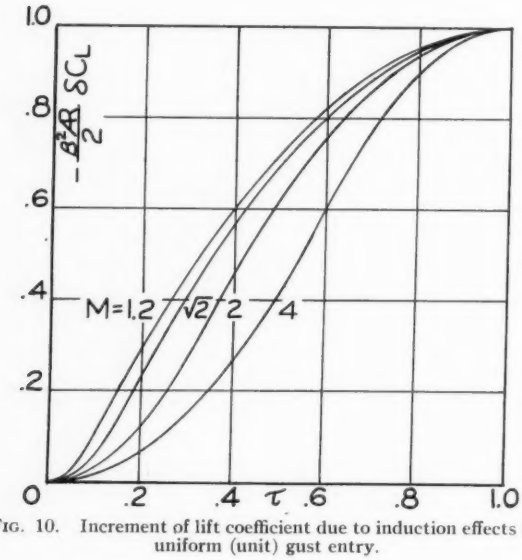

FIG. 10. Increment of lift coefficient due to induction effects for uniform (unit) gust entry.

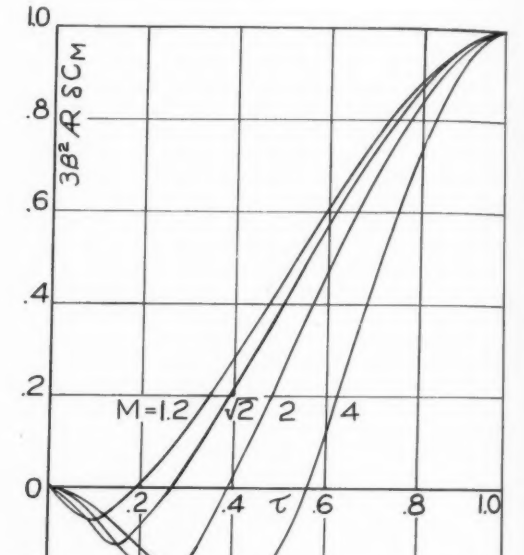

FIG. 11. Increment of moment coefficient due to induction effects for uniform (unit) gust entry.

REFERENCES

[1] Biot, M. A., *Loads on a Supersonic Wing Striking a Sharp-Edged Gust*, Journal of the Aeronautical Sciences, Vol. 16, pp. 296–301, 1949.

[2] Chang, C. C., *The Transient Reaction of an Airfoil Due to Change in Angle of Attack at Supersonic Speed*, Journal of the Aeronautical Sciences, Vol. 15, pp. 635–655, 1948.

[3] Heaslet, M. A., and Lomax, H., *Two-Dimensional Unsteady Lift Problems in Supersonic Flight*, N.A.C.A. T.N. No. 1621, 1948.

[4] Miles, J. W., *Transient Loading of Airfoils at Supersonic Speeds*, Journal of the Aeronautical Sciences, Vol. 15, pp. 592–598, 1948.

[5] Schwarz, L., *Plane Non-Stationary Theory of the Wing at Supersonic Speed*, U.S.A.A.F. Translation, F-TS-934-RE, Wright Field, Dayton, Ohio, 1947.

[6] Naval Ordnance Test Station, *The Oscillating Rectangular Airfoil at Supersonic Speeds*, by J. W. Miles, Inyokern, Calif., NOTS, 1 June, 1949 (Technical Memorandum RRB-15). (Also in press, Quart. Appl. Math.)

Lateral Control Devices Suitable for Use with Full-Span Flaps

(*Continued from page 638*)

[36] Rogallo, Francis M., *Aerodynamic Characteristics of a Slot-Lip Aileron and Slotted Flap for Dive Brakes*, N.A.C.A. A.C.R., April, 1941.

[37] Shevell, Richard S., *Operational Aerodynamics of High-Speed Transport Aircraft*, Journal of the Aeronautical Sciences, Vol. 15, No. 3, pp. 133–143, March, 1948.

[38] Fischel, Jack, and Tamburello, Vito, *Investigation of Effect of Span, Spanwise Location, and Chordwise Location of Spoilers on Lateral Control Characteristics of a Tapered Wing*, N.A.C.A. T.N. No. 1294, 1947.

[39] Weick, Fred E., and Jones, Robert T., *Résumé and Analysis of NACA Lateral Control Research*, N.A.C.A. T.R. No. 605, 1937.

[40] Pearson, Henry A., and Jones, Robert T., *Theoretical Stability and Control Characteristics of Wings with Various Amounts of Taper and Twist*, N.A.C.A. T.R. No. 635, 1938.

[41] Gilruth, R. R., and Turner, W. N., *Lateral Control Required or Satisfactory Flying Qualities Based on Flight Tests of Numerous Airplanes*, N.A.C.A. T.R. No. 715, 1941.

The Gyroscopic Effect of a Rigid Rotating Propeller on Engine and Wing Vibration Modes

R. H. SCANLAN* AND JOHN C. TRUMAN†

Rensselaer Polytechnic Institute

SUMMARY

In many wing vibration analyses it is found necessary to take into account the effect of flexibly mounted engines. Hence, it is reasonable to ask what vibratory gyroscopic effect this flexibility may give rise to when propellers are whirling. An engine mount may be thought of as a horizontal beam cantilevered from the wing, having both horizontal and vertical flexibility. If this beam were infinitely rigid horizontally, then, when it vibrated, the gyroscopic moments induced in the propeller due to the resultant pitching motion of its axis would not produce propeller axis yaw. However, engine-mount lateral stiffness (which allows propeller axis yaw) may actually be less than vertical stiffness, so that gyroscopic effects will play a role as the propeller axis undergoes pitching vibrations at the tip of the cantilever engine mount. The purpose of this paper is to investigate this role under the assumption that the propeller itself is a rigid disc.

The paper is divided into four parts. Part (I) deals briefly with classical gyroscope theory. Part (II) presents engine vibration mode studies—experimental photographic techniques on a model gyroscope mounted at the ends of two different cantilever beams. Part (III) presents the theory of the coupled motion of an elastic wing upon which a gyroscope is mounted to simulate an engine-propeller system on an airplane. Part (IV) consists of an example of the theory of Part (III), in which, by taking what are thought to be reasonable parameters, results are obtained showing how the whirling of a rigid propeller may materially affect wing normal mode shapes and frequencies.

(I) BASIC GYROSCOPE THEORY

CONSIDER A GYROSCOPE (Fig. 1) with one point at the origin 0 of a rectangular coordinate system 0-*X*-*Y*-*Z* fixed in space. Let 0 also be the origin of a rectangular coordinate system 0-1-2-3 fixed in the gyroscope. Assume that the gyroscope has mass moments of inertia I_1, I_2, and I_3, respectively, about its axes 1, 2, and 3 and that it is symmetric about axis 3—that is, $I_1 = I_2$. It is assumed that the "axis of figure" is then the 3-axis and that the gyroscope is spinning about this axis. Under these conditions, the position of the gyroscope at any time t is uniquely defined by the three Euler angles—θ, φ, and ψ.

It is of interest to the present discussion to conceive of a "universal joint" at 0 with a built-in spring system having the sole effect of providing a restraint against nutation. Let the spring constant there be K so that the restoring torque becomes

$$M_\theta = -K\theta \tag{1}$$

If no other torques act on the gyroscope, the equations of motion become (in the absence of gravity)

$$\left.\begin{aligned} I_1\ddot{\theta} + K\theta &= I_1\dot{\varphi}^2 \sin\theta\cos\theta - I_3\dot{\varphi}\sin\theta\,(\dot{\psi} + \dot{\varphi}\cos\theta) \\ p_{\varphi_0} &= \text{const.} = I_1 \sin^2\theta\dot{\varphi} + I_3\cos\theta\,(\dot{\psi} + \dot{\varphi}\cos\theta) \\ p_{\psi_0} &= \text{const.} = I_3(\dot{\psi} + \dot{\varphi}\cos\theta) \end{aligned}\right\} \tag{2}$$

At time $t = 0$, let the following representative initial conditions hold:

$$\left.\begin{aligned} \theta &= \theta_0 \neq 0 \\ \dot{\theta} &= 0 \\ \varphi &= \varphi_0 = \pi/2, \quad \dot{\varphi} = 0 \\ \dot{\psi} &= \dot{\psi}_0 = \Omega \neq 0 \end{aligned}\right\} \tag{3}$$

Then, initially, also

$$\begin{aligned} p_{\psi_0} &= I_3\dot{\psi}_0 = I_3\Omega = p_0 \\ p_{\varphi_0} &= p_0\cos\theta_0 \end{aligned}$$

The solutions of Eqs. (2) for θ and φ, under the as-

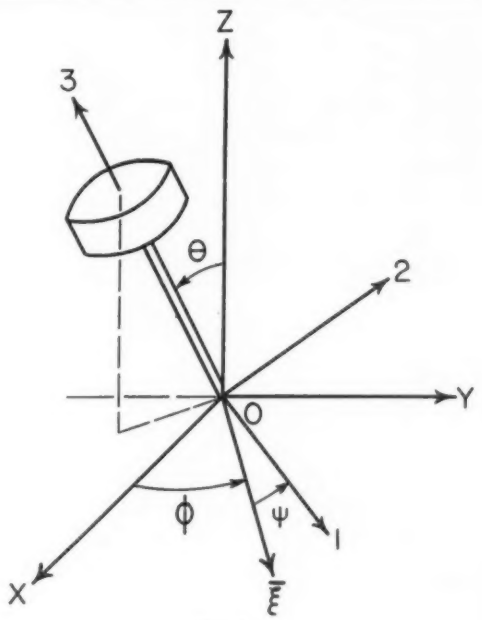

FIG. 1.

Presented at the Aeroelasticity Session, Eighteenth Annual Meeting, I.A.S., New York, January 23–26, 1950.

* Associate Professor of Aeronautical Engineering.

† Instructor, Physics Department. Now, Development Engineer, Thermal Power Systems Division, General Electric Company.

sumption of small nutation angle θ, are

$$\theta = \theta_0 \left[\frac{1}{1 + (1/P)} + \frac{1}{1 + P} \cos \omega t \right] \quad (4)$$

$$\varphi = \frac{-p_0 \theta_0}{I_1 \sin \theta_0} \left(\frac{1}{1 + P} \right) \left(t - \frac{\sin \omega t}{\omega} \right) + \pi/2 \quad (5)$$

where $P = p_0^2/KI_1$ is nondimensional and $\omega^2 = (K/I_1)(1 + P)$. Thus, the small motions of nutation are sinusoidal about some θ-value, and the value of ω^2 indicates that nutation frequency increases with increasing gyroscope spin.

Two limiting cases are of interest: first, when $P \gg 1$ and, second, when $P \ll 1$—i.e., where $p_0 \gg \sqrt{KI_1}$ or $p_0 \ll \sqrt{KI_1}$, respectively. In the first case, nutation is almost nonexistent, since θ maintains a near-constant value θ_0. In the second case, the gyroscope nutates about a θ-value near zero with appreciable amplitude.

Therefore, with nutation small, the gyroscope precesses in a quasi-steady fashion, the variation about a steady state being sinusoidal. In the limiting cases above noted, when P is large, the rate of precession is diminished, while the variation from a steady value becomes faster and of lesser amplitude. At extremely large values of P, there is effectively no precession. On the other hand, when P is small, precession is more rapid and has oscillatory motion of large amplitude superimposed.

The equations of motion given above may be replaced by equations in another useful set of coordinates. This proves to be fruitful for two purposes: The first is the discussion of the motion of, say, the c.g. of the gyroscope as seen by an observer looking down along the Z-axis—i.e., the projection of the motion of the c.g. on the x-y plane; the second is the discussion of the gyroscope motion when the previous "universal" spring constant in the nutation direction is replaced by two independent spring constants acting in the mutually perpendicular fixed planes z-y and z-x, respectively. Such spring constants will be alluded to in the practical examples to follow.

In terms of the approximate "projection coordinates,"

$$\left.\begin{aligned} x &= R\theta \sin \varphi \\ y &= -R\theta \cos \varphi \end{aligned}\right\} \quad (6)$$

the equations of motion of the gyroscope can be shown to be

$$\left.\begin{aligned} I_1 \ddot{x} + p_{\psi_0} \dot{y} + K_x x &= 0 \\ I_1 \ddot{y} - p_{\psi_0} \dot{x} + K_y y &= 0 \end{aligned}\right\} \quad (7)$$

where now the universal nutation spring of stiffness K has been replaced by the two stiffnesses K_x and K_y in perpendicular planes (K_x and K_y are measured, for example, in inch pounds per radian).

The general solutions of Eqs. (7) are each sums of four terms having factors like $\epsilon^{\pm i\mu t}$, $\epsilon^{\pm i\nu t}$, and may be expressed in the form

$$x = A \cos (\mu t - \epsilon_1) + B \cos (\nu t - \epsilon_2)$$

with a similar equation for y, where A, B, ϵ_1, ϵ_2 are appropriate constants.

The entire discussion to this point follows classical lines[1-3] and is included to serve as introduction to subsequent parts.

(II) Applications of Classical Gyroscope Theory

The questions that originally motivated the present study were to determine the dynamic effect of spin on an elastically mounted rotating body and, in particular, the effect of a spinning propeller on the vibration modes of an aircraft engine mounted on a cantilever engine mount.

Bennett[4] has examined this problem partially for a typical small, high-speed, shock-mounted motor, such as an aircraft accessory. However, it is felt that the present discussion improves and extends his treatment. He does not discuss the vibratory *modes*, which are of greatest interest to the problem; nor does he evaluate properly the role of the spring supports, which are not generally oriented simply in the nutation direction as he assumes. Finally, intermediate steps in his numerical evaluation of the increase in nutational frequency due to spin appear to be in error.*

For the discussion of the case of the aircraft engine, the z-axis, Fig. 1, will be assumed horizontal pointing forward in the direction of propeller thrust. The x-axis will be taken positive vertically downward, while the y-axis is horizontal positive to the left of an observer looking in the direction of positive z.

The cantilever engine mount may be assumed effectively as a simple cantilever beam. The aircraft or aircraft wing supporting the system will be considered completely rigid and stationary in space, as for example a rigid test stand. It is readily shown that a single force or moment acting at the free end of a cantilever beam causes the beam to slope so that the tangent line to the beam at its free end passes through an effective "rotation point" about which the end of the bent beam appears to pivot for varying load. Associated with this rotation point is, then, an effective radius R from the pivot to the beam tip. When both forces and moments act simultaneously on the beam and vary with time as well, they must bear a constant proportionality to each other in order to maintain, at all times, the same effective rotation point for the beam tip. In harmonic oscillations, this constant proportionality is satisfied, and it will be assumed approximated in the practical cases to be discussed here. The validity of this approximation is akin to that of the usual assump-

* Bennett appears to give an incorrect value $C/A = I_3/I_1 = 0.019$ for the rotor in his example. The present authors find this value to be 0.0085, which, taking $K = 0$ in $\omega^2 = (K/I_1) + (p_0/I_1)^2$, yields $f = \omega/2\pi = 0.85$ cycles per sec., a value comparable to Bennett's 0.95 cycles per sec.

tions of effective elastic axes of wings or empennages in flutter analyses, etc.

Thus, the propeller and engine parts that rotate will be assumed to be an effective rigid rotor; this rotor, pivoting for nutational motion about the effective rotation point described above, then forms a classical symmetric gyroscope, with point 0 of Fig. 1 now at the pivot point. The effect of gravity on the horizontal gyroscope can be ruled out by considering the equilibrium position to be the actual steady position of the system with rotor spinning and gravity acting. Under these assumptions, the effect of the spinning propeller on the vibrational characteristics of the system may be calculated, employing the theory of Part (I).

A model was built to study qualitatively what the gyroscopic effect on engine vibration mode shapes is likely to be (Figs. 2 and 3). The gyroscope spin axis was hung vertically downward, rather than horizontal as for an engine-propeller system, thus providing the opportunity to employ relatively flexible supports in the role of gyroscope mount without unwanted distortion due to gravity. This allowed correspondingly large gyroscopic motions so that the modal shapes could be clearly ascertained.

Under the model and attached to it, as shown in Figs. 2 and 3, was mounted a strontium arc lamp that provided an effective point source of light. A portrait camera mounted vertically beneath the lamp photographed traces of the gyroscope motion over specified time intervals, the camera shutter being left open in darkness during the entire interval. Figs. 4–10 show typical traces obtained in this manner. As these traces actually lie in the x,y or "projection" coordinates, they illustrate motion of the type represented by Eqs. (7).

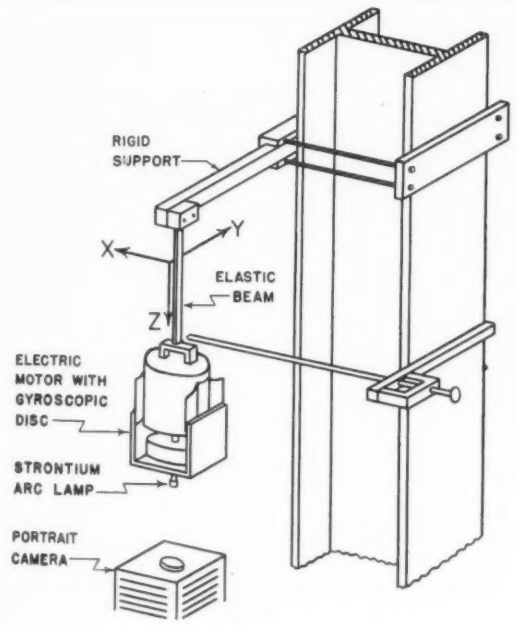

FIG. 2.

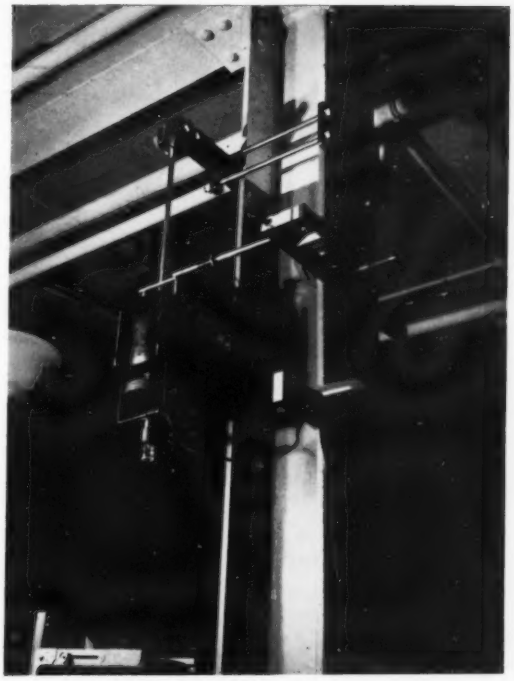

FIG. 3.

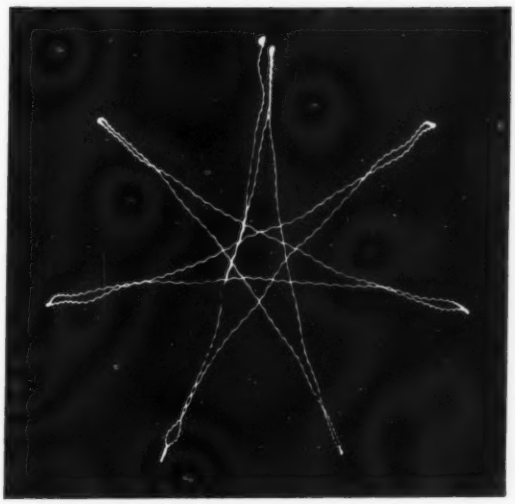

FIG. 4.

Fig. 4 is a trace of the motion of the gyroscope mounted on a beam of square cross section and given an initial displacement (nutation) with no initial precession. Figs. 5 and 6 show the corresponding motion of a beam of rectangular section, not square, initially displaced in the direction of lesser and of greater stiffness, respectively. Fig. 7 indicates motion under more general initial conditions, the gyroscope having an initial displacement together with an initial precessional ve-

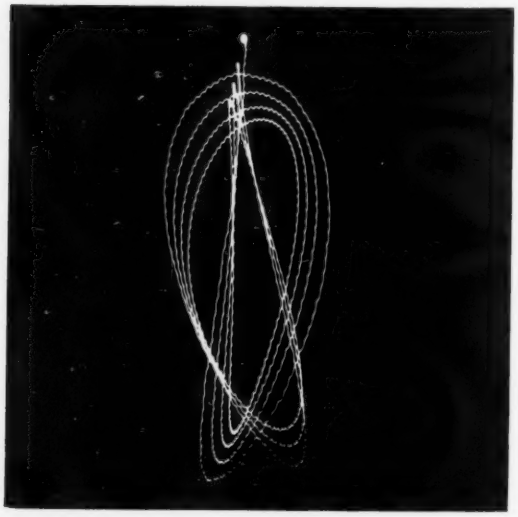

FIG. 5.

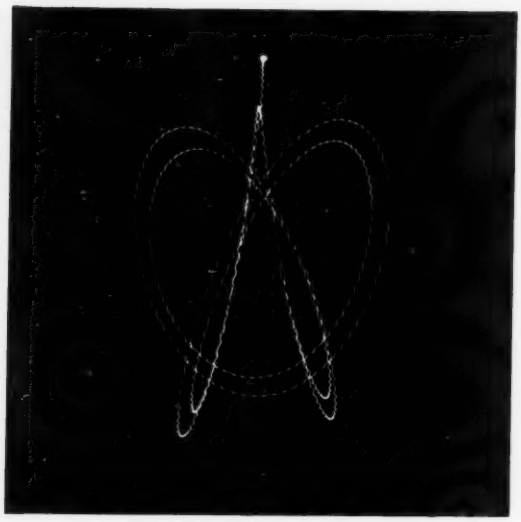

FIG. 6.

locity. Figs. 4, 6, and 7 covered a period of 1.5 sec., while Fig. 5 was for 3.0 sec.

Figs. 8, 9, and 10 show damping of the oscillations, resulting in a decrease of amplitude as the characteristic figure precesses. This damping has not been considered in the theory presented herein but may be taken into account by the introduction, for example, of a dissipation function into the kinetic potential. Fig. 8 is a trace of the same motion as that of Fig. 4 for a period of 15 sec., while Figs. 9 and 10 correspond to Figs. 5 and 6, respectively, for a period of 10 sec. The small oscillations observed on all experimental traces result from vibrations in the gyroscope at its spin frequency.

It should be realized that the traces presented herein are by no means general for all systems but depend for their shape on the various parameters of the particular system—namely, I_1, I_3, Ω, K_x, and K_y—as well as the initial conditions of the motion. It was found possible to predict qualitatively the motion indicated in Fig. 4, for example, using the theory of Part (I). No theoretical obstacle would prevent the point-for-point verification of Figs. 4–10 if this were desired, although the process is laborious.

(III) Theory of the Gyroscope with Elastically Mounted Pivot

The gyroscopic theory and experiments of Parts (I) and (II) provide a firm basis for undertaking a further problem—that of the gyroscopic beam system mounted on an elastic, rather than a rigid, base. The system of Parts (I) and (II) simulates a propeller-engine-mount system attached to a rigid jig or foundation. Here,

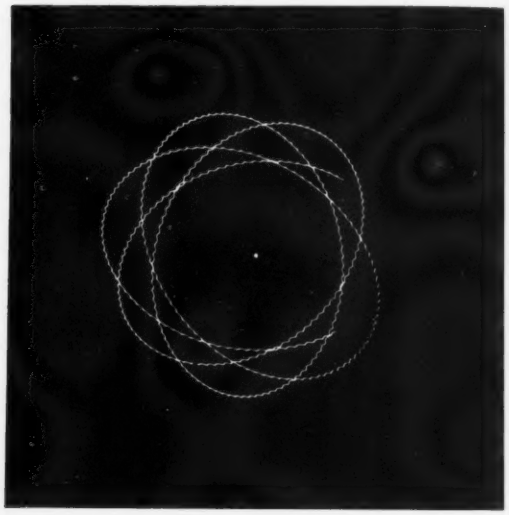

FIG. 7.

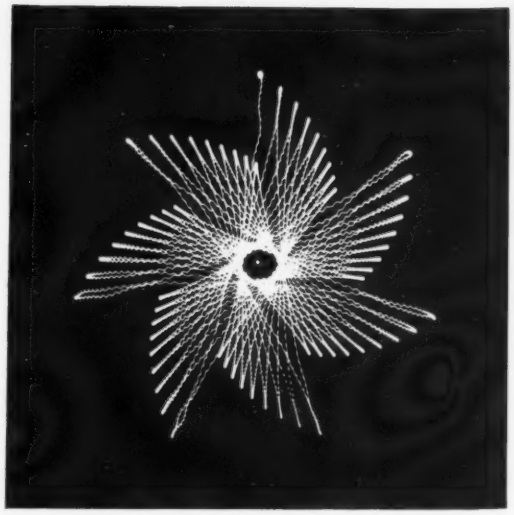

FIG. 8.

this foundation becomes elastic, playing the role of the aircraft wing. In particular, the gyroscope will be taken in the orientation of a rigid propeller with axis horizontal as described in Part (II). However, the pivot point (origin of x, y, and z coordinates) will now be assumed to move vertically, with deflection h_a as part of a vibrating aircraft wing (Fig. 11).

If, as in many modern vibration analyses,[5] the wing is approximated by a series of N individual masses m_k, then the kinetic energy of the wing with elastically mounted engine, but with propeller not rotating, is

$$T_W = (1/2) \sum_{k=1}^{N} m_k \dot{h}_k^2 \tag{8}$$

Although a greater number of normal modes may enter, for simplification it will be assumed here that only two normal modes of the wing are brought into action by the presence of the spinning propeller. Thus,

$$h_k = h_{k1}\xi_1 + h_{k2}\xi_2 \tag{9}$$

where h_{k1} and h_{k2} are the nondimensional values of the displacement of mass m_k in the first and second normal modes, respectively, while ξ_1, ξ_2 are the associated generalized coordinates (with dimensions of length). Therefore,

$$T_W = (1/2) \sum_{k=1}^{N} m_k(h_{k1}^2\dot{\xi}_1^2 + h_{k2}^2\dot{\xi}_2^2) = (1/2)(A_1\dot{\xi}_1^2 + A_2\dot{\xi}_2^2) \tag{10}$$

since orthogonality between normal modes implies that

$$\sum_{1}^{N} m_k h_{k1} h_{k2} = 0 \tag{11}$$

Then the potential energy of this motion is

$$U_W = (1/2)\omega_1^2 A_1 \xi_1^2 + (1/2)\omega_2^2 A_2 \xi_2^2 \tag{12}$$

where ω_1 and ω_2 are the circular frequencies of the first two normal modes.

Let the linear horizontal engine mount spring constant be $k_y = K_y/R^2$, so that energy stored by y deflection is $(1/2)k_y y^2$. Let h_g be the vertical displacement in space of the engine-propeller mass and h_a be the vertical displacement in space of the pivot point of the gyroscope system. Under these assumptions, the kinetic potential of the entire system is

$$\Phi = \frac{1}{2}\frac{I_1}{R^2}(\dot{x}^2 + \dot{y}^2) + p_{\dot{\psi}_0}\left[\frac{x\dot{y} - y\dot{x}}{x^2 + y^2} \times \left(1 - \frac{x^2 + y^2}{2R^2}\right)\right] - \frac{-p_{\dot{\psi}_0}^2}{2I_3} - \frac{1}{2}k_y y^2 + T_W - U_W \tag{13}$$

where

$$x = h_g - h_a = \bar{a}_1\xi_1 + \bar{a}_2\xi_2 \tag{14}$$

Thus, Φ is a function of ξ_1, ξ_2, and y. Application of Lagrange's equations in ξ_1, ξ_2, and y yields three equations of motion, the coefficients of which are constants

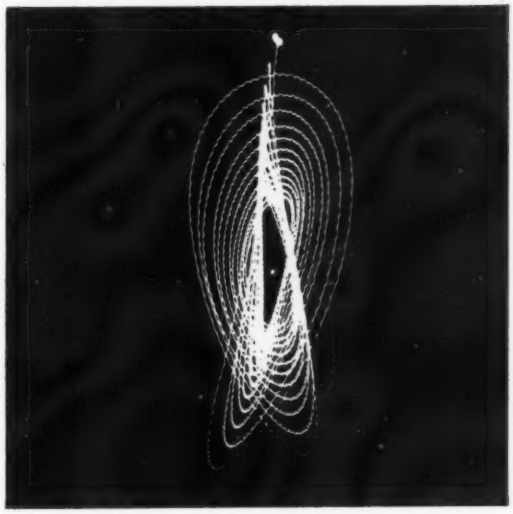

FIG. 9.

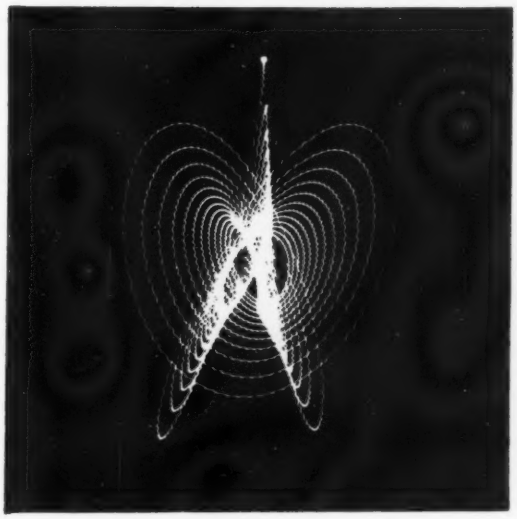

FIG. 10.

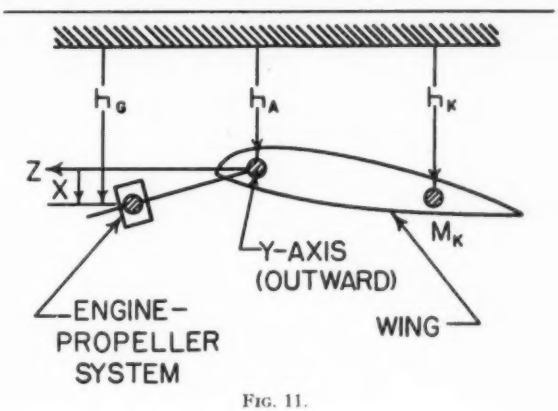

FIG. 11.

of the system. The equations of motion are thus expressed as

$$\left.\begin{aligned} a_1\ddot{\xi}_1 + b_1\ddot{\xi}_2 + c_1\dot{y} + d_1\xi_1 &= 0 \\ a_2\ddot{\xi}_1 + b_2\ddot{\xi}_2 + c_2\dot{y} + d_2\xi_2 &= 0 \\ ey + f\dot{\xi}_1 + g\dot{\xi}_2 + ky &= 0 \end{aligned}\right\} \quad (15)$$

where

$$\left.\begin{aligned} a_1 &= \frac{I_1\bar{a}_1^2}{R^2} + A_1, & a_2 &= \frac{I_1\bar{a}_1\bar{a}_2}{R^2} \\ b_1 &= \frac{I_1\bar{a}_1\bar{a}_2}{R^2}, & b_2 &= \frac{I_1\bar{a}_2^2}{R^2} + A_2 \\ c_1 &= \frac{\bar{a}_1 p_{\psi_0}}{R^2}, & c_2 &= \frac{\bar{a}_2 p_{\psi_0}}{R^2} \\ d_1 &= \omega_1^2 A_1, & d_2 &= \omega_2^2 A_2 \\ e &= I_1/R^2 \\ f &= -p_{\psi_0}\bar{a}_1/R^2 \\ g &= -p_{\psi_0}\bar{a}_2/R^2 \\ k &= k_y \end{aligned}\right\} \quad (16)$$

It may be noted that the case of zero gyroscope effect present can be obtained by theoretically moving the propeller off to infinity in the z-direction—i.e., $R \to \infty$. The equations then reduce to those of two noncoupled normal modes, and the value of horizontal engine propeller displacement y is found to be zero, as expected. The terms with denominator R^2 are thus the gyroscopic coupling terms in this instance. It is seen that their effect is generally increased if any of the parameters in them cause the terms themselves to increase. In particular, large engine-propeller pitching inertia (I_1) about the rotation point, or large propeller rotational inertia (I_2), and small distance to effective pivot point (R) will tend to increase the gyroscopic coupling effect of the rotating propeller. The solutions

$$\xi_1 = \xi_{10}e^{\lambda t}, \quad \xi_2 = \xi_{20}e^{\lambda t}, \quad y = y_0 e^{\lambda t} \quad (17)$$

FIG. 12.

TABLE 1a
Normal Modes of XR60-1 Wing

f_1 = 122.8 Cycles per Min.

f_2 = 144.1 Cycles per Min.

TABLE 1b
Gyroscopically Modified Modes of XR60-1 Wing

$\bar{f}_1$ = 122.0 Cycles per Min.

$\bar{f}_2$ = 134.3 Cycles per Min.

Mass	h_1	h_2	$\bar{h}_1$	$\bar{h}_2$
1	4.6664	−0.7938	3.2270	−1.2306
2	4.6757	−0.4114	3.3346	−0.8183
3	2.4974	−0.6292	1.6731	−0.8794
4	2.5740	−0.1365	1.8594	−0.3533
5	1.3136	−0.3741	0.8687	−0.5091
6	1.3826	−0.06373	1.0013	−0.1794
7	0.4604	−0.3758	0.2400	−0.4427
8	0.6701	+0.4345	0.6080	+0.4157
9	1.0000	+1.0000	0.0000	+1.0000
10	−0.1423	−0.2562	−0.1723	−0.2654
11	−0.1167	+0.01035	−0.08321	+0.02051
12	−0.4662	−0.2304	−0.4041	−0.2116
13	−0.4872	+0.09644	−0.3334	+0.1431
14	−0.6962	+0.4338	−0.3983	+0.5242
15	−0.6379	−0.09191	−0.4940	−0.04824

TABLE 2
Inertia Properties of Idealized Wing
(Masses in Slugs)

m_1 = 13.20	m_8 = 45.45
m_2 = 13.20	m_9 = 210.8
m_3 = 20.05	m_{10} = 228.1
m_4 = 20.05	m_{11} = 228.1
m_5 = 214.6	m_{12} = 88.9
m_6 = 214.6	m_{13} = 88.9
m_7 = 45.45	m_{14} = 210.8

m_{15} = 1215.3

may be assumed for these equations, from which are obtained the characteristic values λ—i.e., solutions of the sextic in λ—

$$\begin{vmatrix} a_1\lambda^2 + d_1 & b_1\lambda^2 & c_1\lambda \\ a_2\lambda^2 & b_2\lambda^2 + d_2 & c_2\lambda \\ f\lambda & g\lambda & e\lambda^2 + k \end{vmatrix} = 0 \quad (18)$$

This sextic proves to be a cubic in λ^2, with all roots negative. Hence, the solutions are of the form

$$\xi_1 = \xi_{10}e^{\mp i\bar{\omega}t} \quad (19)$$

etc., where $\bar{\omega}$ is a characteristic frequency; the motion is thus seen to be stable simple harmonic. The three frequencies $\bar{\omega}_1$, $\bar{\omega}_2$, and $\bar{\omega}_3$ represent the frequencies of the gyroscope-coupled system.

(IV) EXAMPLE—VIBRATION OF A WING WITH A SINGLE ROTATING PROPELLER

Reference 5 presents a convenient example for study in the XR60-1 wing, normal vibration modes of which have been calculated assuming flexibly mounted engines.

The plan form of the masses as given in reference 5 is shown in Fig. 12. Table 1a gives the first two normal modes as calculated in reference 5, both modes being normalized on mass m_9. Table 2 gives the values of all masses in slugs.

For simplification, it will be assumed that only a single propeller is rotating, although there are two

engines and propellers on the wing. The outboard propeller will be assumed as rotating; this is located at m_9. It will be further assumed that m_8 is the location of the pivot point for the gyroscope (rigid propeller). Thus, $R = 3.28$ ft. The value of x is given by $x = h_9 - h_8$ or

$$x = \bar{a}_1\xi_1 + \bar{a}_2\xi_2 \tag{20}$$

where

$$\bar{a}_1 = h_{91} - h_{81}, \qquad \bar{a}_2 = h_{92} - h_{82}$$

The example to be worked will contain the following parameters:

$\bar{a}_1$	$= 0.3299$
$\bar{a}_2$	$= 0.5655$
I_1	$= 200$ slugs-ft.^{2}
I_3	$= 235$ slugs-ft.^{2}
R	$= 3.28$ ft.
k	$= 91{,}875$ lbs. per ft. (taken as 75 per cent of vertical stiffness)
A_1	$= 2{,}500.079$
A_2	$= 346.234$
p_0	$= 39{,}375$ (propeller speed is 1,600 r.p.m.)
$f_1 = (60/2\pi)\omega_1$	$= 122.8$ cycles per min.
$f_1 = (60/2\pi)\omega_2$	$= 144.1$ cycles per min.

In assuming propeller inertias, the values of I_3, and especially of I_1 (which are based on simple geometric estimates), are probably much less than those actually to be encountered. The calculated effect is thus thought to be on the conservative side. The value of R cannot be known with accuracy except when more detailed data are given.

The determinant [Eq. (18)] becomes

$$\begin{vmatrix} (2{,}502.102\lambda^2 + 413{,}433) & 3.46817\lambda^2 & 1207.411\lambda \\ 3.46817\lambda^2 & (352.179\lambda^2 + 78{,}841.3) & 2069.69\lambda \\ -1{,}207.411\lambda & -2069.69\lambda & (18.59012\lambda^2 + 91{,}875) \end{vmatrix} = 0$$

The solutions for λ are

$$\lambda_1 = 12.7816i = i\bar{\omega}_1$$
$$\lambda_2 = 14.0674i = i\bar{\omega}_2$$
$$\lambda_3 = 75.6010i = i\bar{\omega}_3$$

and, therefore, the characteristic frequencies are

$$\bar{f}_1 = 122.05 \text{ cycles per min.}$$
$$\bar{f}_2 = 134.33 \text{ cycles per min.}$$
$$\bar{f}_3 = 721.93 \text{ cycles per min.}$$

The first two of these may be compared to given normal mode frequencies of 122.8 and 144.1 cycles per min.

Upon entering λ_1 into the equations of motion [Eqs. (15)], the first modified mode is obtained, wherein it is found that

$$\xi_{20} \cong +0.358\xi_{10}$$

whence the new mode is represented by

$$h_k = (h_{k1} + 0.358h_{k2})\xi_1$$

Hence, the new first mode contains about 36 per cent of the original second. Therefore, in the modified second mode, which is obtained by solving the equations of motion with λ_2 known, there is obtained

$$h_k = [h_{k1}(-0.074) + h_{k2}]\ \xi_2$$

Thus, the new second mode contains 7 per cent of the original first mode. The new modes as modified are given in Table 1b.

The frequency shift is seen to be negligible in the first mode and approximately $7\frac{1}{2}$ per cent in the second. This is of the order of magnitude encountered in many cases wherein engine vertical flexibility alone is deemed worthy of inclusion in the vibration calculation.

The magnitudes of the effects shown in the present example must not be taken too seriously, since the assumptions involved are strong. The point of the situation appears to be, however, that it is not unreasonable to expect propeller gyroscopic effects, say in flight, to modify the results of either calculations or ground vibration tests. Whether the modifications will be large or small depends on the particular system parameters involved. The present analysis suggests that the modifications may, on occasion, be large if some of the following factors are encountered: (a) large values of propeller-engine pitching inertia; (b) small effective radius to "pivot point" of gyroscopic system; (c) large propeller rotational inertia; (d) more than a single engine running; and (e) low engine-mount lateral stiffness. The fact that the propeller is not rigid may be an alleviating factor.

The analysis can be extended directly to cases of two engines running and more wing modes if the higher degree equations that result are no barrier; what is needed in this problem is merely the additive collection of two gyroscope kinetic potentials plus the other usual energies in analogous fashion to Eq. (13), from which the equations of motion are subsequently obtained as before.

The casting of the gyroscope problem in the x-y-coordinate system rather than the usual Euler coordi-

(*Continued on page 666*)

Approximate Solution of Compressible Fluid-Flow Problems by Galerkin's Method

CHI-TEH WANG* AND R. F. BRODSKY†

New York University

SUMMARY

The Galerkin's method has been used in the literature for the approximate solution of elasticity and vibration problems. In this paper, its application to compressible fluid-flow problems is carried out. It is found that, for compressible flow problems, Galerkin's method has two advantages over the Rayleigh-Ritz method, which was previously worked out by one of the authors. First, it is not necessary to formulate variational integrals for various new problems; therefore, these problems can be treated without any mathematical difficulty. Second, there is no restriction on the value of the ratio of specific heats, γ, to be used, a fact that is necessary in the discussion of some irrotational flow problems.[4] The nonlinear problem of compressible flow passing a circular cylinder is carried out as a numerical example. The results are found to be in good agreement with other methods. An extension of Galerkin's method to the general case of flow passing arbitrary bodies is briefly indicated. For these irrotational flow problems, however, Galerkin's method seems to suffer the disadvantage of requiring more work in carrying it out than the Rayleigh-Ritz method. The application of the Galerkin's method to laminar boundary-layer problems is discussed, and the boundary-layer problem of a compressible flow past a flat plate is formulated. A numerical example is carried out to illustrate the method.

SYMBOLS

a	=	velocity of sound
c_p	=	specific heat at constant pressure
c_v	=	specific heat at constant volume
c_f	=	skin friction coefficient
H, h	=	enthalpy
I	=	the variational integral
k	=	coefficient of heat conduction
M	=	Mach Number
p	=	pressure
R_x	=	$u_1\rho_1 x_r/\mu_1$, Reynolds Number at $x = x_r$
R	=	specific gas constant
r, θ	=	polar coordinates
T	=	absolute temperature
u	=	velocity component in x-direction
U	=	free-stream velocity
v	=	velocity component in y-direction
x, y	=	rectangular coordinates
γ	=	ratio of specific heats $= c_p/c_v$
μ	=	the coefficient of viscosity
ρ	=	density
σ	=	Prandtl Number $= \mu c_p/k$
τ	=	viscous stress
ϕ	=	the velocity potential
ω	=	defined by $\mu \propto T^\omega$

Subscripts:

0	=	free-stream conditions
1	=	quantities measured at outer edge of boundary layer
w	=	quantities measured at wall

Received November 18, 1949.

* Associate Professor of Aeronautical Engineering, Daniel Guggenheim School of Aeronautics, College of Engineering.

† Instructor, Department of Mechanical Engineering, College of Engineering.

INTRODUCTION

IN PREVIOUS PAPERS,[1,2] one of the present authors has applied the variational method to the compressible fluid-flow problems following the Rayleigh-Ritz procedure. The results show surprisingly good agreement between the variational method and the other approximate methods. A study of the results also reveals that the variational method gives good approximate solutions at both high and low Mach Numbers and for flows past both thick and thin bodies. The variational method has been applied to steady, nonviscous, irrotational flow past arbitrary bodies without any difficulty. A variational procedure for transonic flows with shock waves has been proposed,[3] but numerical examples are yet to be worked out. For viscous and other flows, it is necessary to formulate new variational principles that are not always easy to accomplish.

On the other hand, in carrying out the variational method, the ratio of the specific heats, γ, has to be such that $\gamma/(\gamma - 1)$ is an integer. For simplicity in computation, $\gamma = 2$ was used in such calculations. This assumption leads to a slight increase in the final velocities[2] but has practically no effect on the final pressure. Nevertheless, this is a point open to objection, especially when it is necessary to use some constants in which γ plays an important role.[4]

In order to overcome these difficulties, Galerkin's[5] method has been applied by the authors to compressible flow problems.[6] Galerkin's procedure does not require the formulation of any new variational principles, and there is no restriction in the value of γ to be used. The only difficulties appear to be the choosing of a function that satisfies the boundary conditions for flow past arbitrary bodies and the method of solution of the resulting nonlinear simultaneous algebraic equations. Methods to surmount these difficulties have already been discussed in detail in references 1 and 2. When the authors first worked on the method,[6] it was thought that the application of Galerkin's method to compressible flow problems was a new venture. It was discovered later that the method was used previously by Akita.[7] However, it appears that the method was

incorrectly carried out in Akita's paper because of an oversight in the integration process.

Galerkin's Method

The Galerkin method has been used in the literature for the approximate solution of elasticity and vibration problems. However, in these problems, other methods for their solutions are available, and Galerkin's method has not received wide attention.

Consider the case of a steady, irrotational compressible flow; the proof for Galerkin's method may be carried out as follows:

In reference 1, the problem of taking the first variation of the variational integral

$$I = \int\int_R F(\phi_x, \phi_y)dx\,dy \tag{1}$$

and setting $\delta I = 0$ was seen to lead to

$$\int\int_R L(\phi)\eta(x, y)dx\,dy = 0 \tag{2}$$

where

$$L(\phi) = -(\partial F_{\phi_x}/\partial x) - (\partial F_{\phi_y}/\partial y) = 0 \tag{3}$$

is the Euler equation associated with the variational problem and $\eta(x, y)$ is an arbitrary function or the first variation of ϕ. After differentiation and simplification, Eq. (3) becomes

$$L(\phi) = (a^2 - \phi_x^2)\phi_{xx} + (a^2 - \phi_y^2)\phi_{yy} - 2\phi_x\phi_y\phi_{xy} = 0 \tag{4}$$

where

$$a^2 = a_0^2 + [(\gamma - 1)/2]\,(U^2 - \phi_x^2 - \phi_y^2)$$

In the above equations, ϕ is the velocity potential, a is the velocity of sound, U is the free-stream velocity, the subscript 0 refers to quantities at infinity, and the subscripts x, y denote partial differentiation.

Eq. (2) can be interpreted as stating that the Euler expression $L(\phi)$ is orthogonal to every variation $\epsilon\eta(x, y)$, where ϵ is an arbitrary small parameter. Assume that ϕ can be approximated by the series

$$\phi_N(x, y) = \sum_{i=1}^{N} c_i f_i(x, y) \tag{5}$$

where the functions $f_i(x, y)$ satisfy the boundary conditions imposed on $\phi(x, y)$ and c_i are undetermined coefficients. Eq. (2) will, in general, no longer be valid for an arbitrary variation $\epsilon\eta(x, y)$, since this would imply that $\phi_N(x, y)$ satisfies the Euler Eq. (4) and, hence, is the exact solution of the boundary-value problem. Although the variation in I does not vanish for an arbitrary variation $\epsilon\eta(x, y)$, the constants c_i in Eq. (5) can be so chosen that the variation in I is zero for the N variations $\epsilon f_i(x, y)$. If, now, N becomes infinite and the functions $f_i(x, y)$ form a complete system of functions, then the set of all relations

$$\int\int L(\phi_N)f_i\,dx\,dy = 0 \quad (i = 1, 2, \ldots, \infty) \tag{6}$$

becomes equivalent to the arbitrary relation (2) and $\phi_N(x, y)$ becomes an exact solution.

The above proof is essentially the one given by Sokolnikoff.[8] Duncan,[9] on the other hand, has given an interesting proof that shows that the Galerkin's method can be derived from the method of least mean square error. Duncan's proof, however, is valid only in the case of linear problems.

The Galerkin process may now be summarized as follows: First, assume a series of functions that satisfy the boundary conditions exactly but with undetermined parameters. For example, in subsonic irrotational compressible flow, the velocity potential ϕ may be expressed as follows:

$$\phi = \phi_0 + \sum_m \sum_n A_{mn}\phi_{mn} \tag{7}$$

where ϕ_0 and ϕ_{mn} satisfy the boundary conditions and A_{mn} are the undetermined parameters. Substitute the assumed expression into the differential Eq. (4). Eq. (4) vanishes if Eq. (7) is the exact solution of the problem. Otherwise $L(\phi_N)$ is a function of x and y and therefore can be taken as a measure of the error associated with the approximation ϕ_N. Multiply $L(\phi_N)$ by ϕ_{mn}, integrate the resulting expression over the domain, and equate to zero. If there are N coefficients, N algebraic equations are obtained which may be solved simultaneously, and the coefficients A_{mn} are thus determined.

Irrotational Compressible Flow Past a Circular Cylinder

As an example, the problem of compressible flow past a circular cylinder has been carried out. The fundamental differential equation of a compressible fluid in polar coordinates is as follows:

$$L(\phi) = \left[a_0^2 + \frac{\gamma - 1}{2}\left(U^2 - \phi_r^2 - \frac{\phi_\theta^2}{r^2}\right) - \phi_r^2\right]\phi_{rr} + \left[a_0^2 + \frac{\gamma - 1}{2}\left(U^2 - \phi_r^2 - \frac{\phi_\theta^2}{r^2}\right) - \frac{\phi_\theta^2}{r^2}\right]\frac{\phi_{\theta\theta}}{r^2} + \left[a_0^2 + \frac{\gamma - 1}{2}\left(U^2 - \phi_r^2 - \frac{\phi_\theta^2}{r^2}\right) + \frac{\phi_\theta^2}{r^2}\right]\frac{\phi_r}{r} - 2\phi_r\phi_\theta\frac{\phi_{r\theta}}{r^2} = 0 \tag{8}$$

where the subscripts r, θ indicate partial differentiation. The boundary conditions are

$$[\phi_r^2 + r^{-2}\phi_\theta^2]^{1/2} = U \text{ at } r = \infty \text{ and } \phi_r = 0 \text{ at } r = 1 \tag{9}$$

The radius of the cylinder is taken to be unity. To satisfy the boundary conditions, ϕ may be assumed as

$$\phi = U\left(r + \frac{1}{r}\right)\cos\theta + \frac{\kappa}{2\pi}\theta + \sum_{m=1}^{\infty}\sum_{n=1}^{\infty}\left[\frac{1}{mr^m} - \frac{1}{(m+2)r^{m+2}}\right](A_{mn}\cos n\theta + B_{mn}\sin n\theta) \tag{10}$$

where κ is the strength of circulation and A_{mn}, B_{mn} are undetermined parameters. Then, the Galerkin equations for determining the parameters A_{mn} and B_{mn} are

$$\left.\begin{aligned}\int_{r=1}^{r=\infty}\int_{\theta=0}^{\theta=2\pi} L(\phi_N)\left[\frac{1}{mr^m} - \frac{1}{(m+2)r^{m+2}}\right]\cos n\theta\, r\, dr\, d\theta = 0\\ \int_{r=1}^{r=\infty}\int_{\theta=0}^{\theta=2\pi} L(\phi_N)\left[\frac{1}{mr^m} - \frac{1}{(m+2)r^{m+2}}\right]\sin n\theta\, r\, dr\, d\theta = 0\end{aligned}\right\} \tag{11}$$

where $L(\phi_N)$ is the resulting Eq. (8) when the assumed ϕ with N parameters [Eq. (10)] has been substituted. If the assumed ϕ is the exact solution of the differential Eq. (8), then $L(\phi_N)$ is equal to zero. In general, of course, ϕ cannot be the exact solution; then, $L(\phi_N)$ will not be zero.

In the case of the flow past a circular cylinder without circulation, the flow must be symmetrical. The unsymmetrical terms in ϕ can therefore be discarded. Taking four parameters, we have

$$\phi = U\left(r + \frac{1}{r}\right)\cos\theta + A_{11}\left(\frac{1}{r} - \frac{1}{3r^3}\right)\cos\theta + A_{13}\left(\frac{1}{r} - \frac{1}{3r^3}\right)\cos 3\theta + A_{31}\left(\frac{1}{3r^3} - \frac{1}{5r^5}\right)\cos\theta + A_{33}\left(\frac{1}{3r^3} - \frac{1}{5r^5}\right)\cos 3\theta \tag{12}$$

Eqs. (11) then become

$$\left.\begin{aligned}\int\int L(\phi_4)\left(\frac{1}{r} - \frac{1}{3r^3}\right)\cos\theta\, r\, dr\, d\theta = 0, \quad \int\int L(\phi_4)\left(\frac{1}{r} - \frac{1}{3r^3}\right)\cos 3\theta\, r\, dr\, d\theta = 0\\ \int\int L(\phi_4)\left(\frac{1}{3r^3} - \frac{1}{5r^5}\right)\cos\theta\, r\, dr\, d\theta = 0, \quad \int\int L(\phi_4)\left(\frac{1}{3r^3} - \frac{1}{5r^5}\right)\cos 3\theta\, r\, dr\, d\theta = 0\end{aligned}\right\} \tag{13}$$

Carrying out the integration and taking $\gamma = 1.405$, the following equations are obtained:

$$\left.\begin{aligned}(0.51851844a_0^2 - 0.6819993U^2)A_{11} + 0.4205556U^2A_{13} + (0.0814814a_0^2 - 0.0902122U^2)A_{31} + 0.0271777U^2A_{33} = K_1\\ + 0.7841668U^2A_{11} + (3.3333328a_0^2 - 3.5691657U^2)A_{13} + 0.1182662U^2A_{31} + (0.3999998a_0^2 - 0.4778126U^2)A_{33} = K_2\\ (0.0814814a_0^2 - 0.0928529U^2)A_{11} + 0.0772793U^2A_{13} + (0.0225185a_0^2 - 0.0152367U^2)A_{31} + 0.0081639U^2A_{33} = K_3\\ + 0.0972529U^2A_{11} + (0.3999998a_0^2 - 0.4950988U^2)A_{13} + 0.0174196A_{31} + (0.0693329a_0^2 - 0.0789673U^2)A_{33} = K_4\end{aligned}\right\} \tag{14}$$

where K_1, K_2, K_3, and K_4 are sums of nonlinear terms in A_{11}, A_{13}, A_{31}, and A_{33}; their complete expressions are given in Appendix I. The order of Eqs. (14) follows from that of Eqs. (13), respectively. These equations can be solved as follows: First, assume the values of A's to be zero in the K's. Eq. (14) then becomes a system of linear simultaneous equations which can be solved by the Crout method.[10] The values of A's so computed may be taken as the first approximation. Use the values of A's obtained to compute K's, and solve for these parameters again. This gives the second approximation. Repeat the cycle until the values of A's computed in two consecutive cycles are the same. An example of the calculation may be found in reference 1. At $M_0 = 0.4$, the solution of Eq. (14) is

$$\left.\begin{aligned}A_{11}/a_0 = 0.09664, \quad A_{13}/a_0 = -0.02194\\ A_{31}/a_0 = -0.04563, \quad A_{33}/a_0 = -0.01975\end{aligned}\right\} \tag{15}$$

TABLE 1
Velocity Distribution on the Surface of a Circular Cylinder at $M_0 = 0.4$

q/U / θ	Galerkin Method ($\gamma = 1.405$) 1 Term	2 Terms	3 Terms	4 Terms	Linearized solution	Variational Method $\gamma = 2$ (4 Terms)	Rayleigh-Janzen Method $\gamma = 1.405$
0	0	0	0	0	0	0	0
10	0.3714	0.3125	0.3119	0.3078	0.3106	0.3022	0.3104
30	1.0696	0.9534	0.9517	0.9435	0.9483	0.9347	0.9588
45	1.5127	1.5108	1.5088	1.4956	1.4962	1.4937	1.4154
60	1.8526	1.8608	1.8584	1.8583	1.8541	1.8663	1.8355
80	2.1068	2.2208	2.2183	2.2254	2.2142	2.2460	2.2269
90	2.1393	2.2697	2.2672	2.2753	2.2632	2.2979	2.284

TABLE 2
Velocity Distribution at $\theta = \pi/2$ from Various Methods

q/U / r/b	Galerkin Method ($\gamma = 1.405$) 1 Term	2 Terms	3 Terms	4 Terms	Linearized solution	Variational Method $\gamma = 2$ (4 Terms)	Taylor Experimental Method $\gamma = 1.407$	Rayleigh-Janzen Method $\gamma = 1.405$
1.0	2.1393	2.2697	2.2672	2.2753	2.2632	2.2979	...	2.284
1.04	2.0582	2.1833	2.1810	2.1887	2.1770	2.210	2.13	2.197
1.2	1.8059	1.9104	1.9099	1.9144	1.9052	1.931	1.89	1.920
1.5	1.5235	1.5976	1.5990	1.6000	1.5940	1.610	1.60	1.603
2.0	1.2979	1.3427	1.3412	1.3437	1.3406	1.349	1.35	1.345
3.0	1.1335	1.1544	1.1560	1.1547	1.1534	1.157	1.18	1.155

TABLE 3
Values of A_{mn} When One, Two, Three, and Four Parameters Are Taken

A_{11}'	A_{13}'	A_{31}'	A_{33}'
0.0836000			
0.0892318	−0.0242009		
0.0969708	−0.0242472	−0.0469989	
0.0966415	−0.0219423	−0.0456325	−0.0197478
Linearized Values			
0.09352	−0.02158	−0.04462	−0.01425

The velocity distribution on the surface of the cylinder and that at $\theta = \pi/2$ computed by Galerkin's method are tabulated in Tables 1 and 2, together with the Taylor[11] electrical analog results, the third approximation of the Rayleigh-Janzen method by Imai,[12] and the variational method following Rayleigh-Ritz procedure.[1, 2] The results show close agreement with those previously obtained. In order to get an idea of the convergence of the series, the velocity distributions at these points are also computed by taking only one parameter A_{11}; two parameters A_{11}, A_{13}; and three parameters A_{11}, A_{13}, A_{31}. It may be mentioned that if only A_{11} is taken, the first equation of Eqs. (14) must be used for solving for A_{11}. If two parameters, A_{11} and A_{13}, are taken, the first two equations of Eqs. (14) are to be used, etc. The values of A_{mn} are different when different combinations of parameters are taken. At $M_0 = 0.4$, the parameters A_{mn}/a_0 are given in Table 3, and the velocity distributions computed by taking one, two, and three parameters are tabulated in Tables 1 and 2 for comparison. It appears that the rapidity of convergence of the values for velocities is satisfactory.

As mentioned previously, the velocity distributions computed by the Galerkin procedure show good agreement with those obtained by the Rayleigh-Ritz procedure. This confirms the fact that the use of $\gamma = 2$ in the computation has only a slight effect on the magnitude of the velocities. Now let us compare the necessary amount of computational labor in these two methods. It is found that Galerkin's procedure requires much more work, especially when flow past an arbitrary body is to be studied. Therefore, in the case of irrotational steady flows past arbitrary bodies, the variational method following Rayleigh-Ritz procedure is recommended. If only the velocity and pressure distributions are to be computed, the linearized variational integral may be used to give good approximate results with only a small amount of work. This fact has already been discussed in reference 4. As an additional example to show that the method of linearization suggested in reference 4 also gives good results in the present approach, the velocity distributions computed from the linearized solution are also included in Tables 1 and 2. It can be seen that the agreement between these results is good.*

LAMINAR BOUNDARY-LAYER PROBLEMS IN COMPRESSIBLE FLOW

The motion of a compressible fluid in laminar boundary layer is to be determined from the following governing equations:

* The authors are indebted to Messrs. P. C. Chou, R. N. House, Jr., and J. Van Name for their help in carrying out and checking the integration.

(1) Equations of motion,

$$\rho u u_x + \rho v u_y = (\mu u_y)_y - p_x \tag{16}$$

$$p_y = 0 \tag{17}$$

(2) Equation of continuity,

$$(\rho u)_x + (\rho v)_y = 0 \tag{18}$$

(3) Equation of energy,

$$\rho u H_x + \rho v H_y = [(\mu H_y)_y/\sigma] + \mu u_y{}^2 + u p_x \tag{19}$$

(4) Equation of state,

$$p = R\rho T \tag{20}$$

where μ is the coefficient of viscosity, $H = \int c_p\, dT$ is the specific enthalpy, c_p is the specific heat at constant pressure, T is the absolute temperature, $\sigma = \mu c_p/k$ is the Prandtl Number, k is the coefficient of heat conduction, and R is the specific gas constant. For a perfect gas, c_p is a constant and $H = c_p T$. Eqs. (16) to (20) are five equations in terms of the five variables u, v, p, ρ, and T.

The coefficient of viscosity μ is a function of T only. An approximate relation between T and μ may be written as

$$\mu \propto T^{\omega} \tag{21}$$

where ω varies according to the range of T in which we are interested. By means of Crocco's transformation,[13] Eqs. (16) to (20) may be reduced to the following two equations in the variables H and τ:

$$u(\rho\mu/\tau)_x + \tau_{uu} - p_x(\mu/\tau)_u = 0 \tag{22}$$

$$\left(\frac{1-\sigma}{\sigma}\right) H_u \tau\tau_u + \frac{(H_{uu} + \sigma)\tau^2}{\sigma} - u\rho\mu H_u + \mu(H_u + u)p_x = 0 \tag{23}$$

where $\tau = \mu u_y$. A summary of Crocco's work may be found in a report by Young.[14]

In the case of the flat plate at zero incidence, Eqs. (22) and (23) may further be reduced to ordinary equations in terms of a single independent variable. This variable is of the form $\xi = cy/\sqrt{2x}$, where c is a constant. In this case, we may write $H = H(u)$, $\rho = \rho(u)$, $\mu = \mu(u)$, and

$$\tau = \mu u_y = \mu u \xi\, \xi_y = f(u)/\sqrt{2x} \tag{24}$$

where $f(u)$ indicates a function u. Eqs. (22) and (23) therefore become

$$ff'' + u\rho\mu = 0 \tag{25}$$

$$(H'' + \sigma)f + (1 - \sigma)H' f' = 0 \tag{26}$$

where primes denote differentiation with respect to u. Note that $p_x = 0$ in this case. Then, introduce the following nondimensional parameters:

$$u/u_1 = \bar{u},\ H/H_1 = h,\quad \rho/\rho_1 = \bar{\rho}$$

$$\mu/\mu_1 = \bar{\mu},\quad F(\bar{u}) = f(u)\sqrt{2/\rho_1\mu_1 u_1{}^3}$$

where the subscript 1 refers to quantities in the main stream. From the equation of state [Eq. (20)], we have

$$\bar{\rho} = \rho/\rho_1 = T_1/T = H_1/H = 1/h$$

and

$$\bar{\mu} = \mu/\mu_1 = (T/T_1)^{\omega} = h^{\omega}$$

With these relationships, Eqs. (25) and (26) may be put in the following form:

$$FF'' + 2\bar{u}h^{-(1-\omega)} = 0 \tag{27}$$

$$(h'' + \sigma u_1{}^2/H_1)F + (1 - \sigma)h'F' = 0 \tag{28}$$

where the primes now denote differentiation with respect to $\bar{u}$, noting that

$$u_1{}^2/H_1 = (\gamma - 1)M_1{}^2$$

The boundary conditions are

$$\left.\begin{aligned} F' &= 0,\quad h = H_w/H_1 \text{ (when } \bar{u} = 0) \\ F &= 0,\quad h = 1 \text{ (when } \bar{u} = 1) \end{aligned}\right\} \tag{29}$$

where the subscript w denotes quantities measured at the wall.

By a laborious trial-and-error method, Crocco integrated Eqs. (27) and (28) step by step for different values of σ, ω at various M_1. Approximate solutions, however, can be more easily obtained by the Galerkin method. In this case, Galerkin's method may be carried out as follows: First, assume F in terms of a series of functions that satisfy the boundary conditions but with undetermined parameters. Then, Eq. (28) becomes a linear ordinary differential equation in h and can be solved analytically. Now, the solution of h is obtained which contains the undetermined parameters assumed in F. These parameters can be determined from Eq. (27) by means of the Galerkin method.

Define the skin friction coefficient c_f to be $2\tau_w/\rho_1 u_1{}^2$; the local skin friction coefficient at a point distant x from the leading edge of the plate may be computed from the following equation:

$$c_f = F(0)/\sqrt{R_x} \tag{30}$$

where $R_x = u_1\rho_1 x/\mu_1$ and $F(0)$ denotes the value of F at $\bar{u} = 0$. Eq. (30) may be easily derived from Eq. (24). Once $F(\bar{u})$ is determined, the relation between y and u is given by Eq. (24), and, hence,

$$y = \int \mu du/\tau(x, u)$$

which reduces to

$$u_1\rho_1 y/\mu_1 = 2\sqrt{R_x}\int^{\bar{u}} h^{\omega} d\bar{u}/F(\bar{u}) \tag{31}$$

As a numerical example, assume

$$F = A(1 - \bar{u}^2)^{1/2} \tag{32}$$

where A is an undetermined parameter. Note that Eq. (32) satisfies the boundary conditions. Substituting Eq. (32) into Eq. (28) and solving, one obtains

$$h = 1 - h'(0)\, C(\bar{u}, \sigma) + \sigma \frac{u_1^2}{H_1}\, D(\bar{u}, \sigma) \qquad (33)$$

where

$$C(\bar{u}, \sigma) = \int_{\bar{u}}^{1} (1 - \bar{u}^2)^{(\sigma-1)/2}\, d\bar{u}$$

and

$$D(u, \sigma) = \int_{\bar{u}}^{1} (1 - \bar{u}^2)^{(\sigma-1)/2} \times \left[\int^{\bar{u}} (1 - \bar{u}^2)^{(1-\sigma)/2}\, d\bar{u}\right] d\bar{u}$$

The parameter A may be determined from the Galerkin method by substituting into Eq. (27) the assumed expression for F and the expression h given by Eq. (33), by multiplying the resulting expression by $(1 - \bar{u}^2)^{1/2}$, integrating over the region of $\bar{u}$, then setting the resulting expression to zero. Therefore, we obtain

$$A^2 = \left[\int_0^1 2\bar{u}h^{-(1-\omega)} (1 - \bar{u})^{1/2}\, d\bar{u}\right] \div \left[\int_0^1 (1 - \bar{u}^2)^{-1/2}\, d\bar{u}\right] \qquad (34)$$

For various values of σ and ω, Eq. (34) can, in general, be integrated by numerical methods.

If $\sigma = 1$ and $\omega = 1$, Eq. (34) can be easily integrated to give

$$A = 0.652, \quad c_f = 0.652/\sqrt{R_x}$$

The value of A computed by the present method is seen to compare favorably with the value 0.664 arrived at by Crocco for one side of the plate.

References

[1] Wang, Chi-Teh, *Variational Method in the Theory of Compressible Fluid*, Journal of the Aeronautical Sciences, Vol. 15, No 11, pp. 675–685, November, 1948.

[2] Wang, Chi-Teh, *Two-Dimensional Subsonic Compressible Flows Past Arbitrary Bodies by the Variational Method*, report submitted to N.A.C.A., June, 1949.

[3] Wang, Chi-Teh, *A Variational Method for Transonic Flows with Shock Waves*, report submitted to N.A.C.A., June, 1949.

[4] Wang, Chi-Teh, and Rao, G. V. R., *A Study of the Nonlinear Characteristics of Compressible Flow Equations by Means of Variational Methods*, Journal of the Aeronautical Sciences, Vol. 17, No. 6, pp. 343–348, June, 1950.

[5] Galerkin, B. G., *Series Solution of Some Problems of Elastic Equilibrium of Rods and Plates*, Vestnik Inghenerov, Vol. I, pp. 879–908, 1915 (in Russian).

[6] Wang, Chi-Teh, and Brodsky, R. F., *Application of Galerkin's Method to Compressible Fluid Flow Problems*, Journal of Applied Physics, Vol. 20, No. 12, pp. 1255–1256, December, 1949.

[7] Akita, Y., *On the Nonlinearity of Gas Dynamics*, J. Soc. Appl. Mech. Japan, Vol. 1, pp. 48–56, March, 1948 (in Japanese). English review appeared in J. of App. Mech. Rev., Vol. 2, No. 7, p. 158, July, 1949.

[8] Sokolnikoff, I. S., and Specht, R. D., *Mathematical Theory of Elasticity*, pp. 313–316; McGraw-Hill Book Company, Inc., New York, 1946.

[9] Duncan, W. T., *Galerkin's Method in Mechanics and Differential Equations*, British A.R.C., R. & M. No. 1798, August, 1937.

[10] Crout, P. D., *A Short Method for Evaluating Determinants and Solving Systems of Linear Equations with Real or Complex Coefficients*, Transactions of A.I.E.E., Vol. 60, 1941.

[11] Taylor, G. I., and Sharman, C. F., *A Mechanical Method for Solving Problems of Flow in Compressible Fluids*, Proc. Royal Society, Series A, Vol. 121, p. 194, 1928.

[12] Imai, I., *On the Flow of a Compressible Fluid Past a Circular Cylinder, II*, Proc. of the Physico-Math. Society of Japan, Third Series, Vol. 23, No. 3, pp. 180–193, March, 1941.

[13] Crocco, L., *Lo Strato Limite Laminare Nei Gas*, Monografie Scientifiche di Aeronautica, Roma, Italy, No. 3, December, 1946. (Translated by I. Hodes and J. Castelfranco, Report CF-1038, Aerophysics Laboratory, North American Aviation, Inc., July 15, 1948.)

[14] Young, A. D., *Skin Friction in the Laminar Boundary Layer in Compressible Flow*, The Aeronautical Quarterly (Royal Aeronautical Society, London), Vol. 1, Part II, pp. 137–164, August, 1949.

Appendix I

$$K_1 = 0.5277779U^3 + 0.1578077UA_{11}^2 + 0.0114401A_{11}^3 - 0.0793961A_{13}A_{11}^2 + 0.0031080A_{31}A_{11}^2 - 0.0068258A_{33}A_{11}^2 + 1.3192771UA_{13}^2 + 0.1905871A_{11}A_{13}^2 + 0A_{13}^3 - 0.0069812A_{31}A_{13}^2 + 0A_{33}A_{13}^2 + 0.0008986UA_{31}^2 + 0.0175325A_{11}A_{31}^2 + 0.0476120A_{13}A_{31}^2 - 0.0000715A_{31}^3 - 0.0009874A_{33}A_{31}^2 + 0.0380331UA_{33}^2 + 0.0034900A_{11}A_{33}^2 + 0A_{13}A_{33}^2 - 0.0016714A_{31}A_{33}^2 + 0A_{33}^3 - 0.3242225UA_{11}A_{13} + 0.3373647UA_{11}A_{31} - 0.0498134UA_{11}A_{33} - 0.0739787UA_{13}A_{31} - 0.0397553A_{11}A_{13}A_{31} + 0.3072313A_{13}A_{31}A_{33} + 0.4331232UA_{13}A_{33} + 0.0506732A_{11}A_{13}A_{33} - 0.0144869UA_{31}A_{33} + 0.0298569A_{11}A_{13}A_{32} + 0Ua_0^2$$

$$K_2 = -0.8333333U^3 - 0.1672530UA_{11}^2 - 0.0085908A_{11}^3 + 0.2978344A_{31}A_{11}^2 - 0.0002069A_{21}A_{11}^2 + 0.0389466A_{33}A_{11}^2 + 0UA_{13}^2 + 0A_{11}A_{13}^2 + 1.2948582A_{13}^3 + 0A_{31}A_{13}^2 + 0.6152349A_{33}A_{13}^2 + 0.0002484UA_{31}^2 - 0.0165082A_{11}A_{31}^2 + 0.0106790A_{13}A_{31}^2 + 0.0001667A_{31}^3 + 0.0013032A_{33}A_{31}^2 + 0UA_{33}^2 + 0A_{11}A_{33}^2 + 0.2591467A_{13}A_{33}^2 + 0A_{31}A_{33}^2 + 0.0054076A_{33}^3 + 1.9752402UA_{11}A_{13} - 0.0380053UA_{11}A_{31} + 0.2912086UA_{11}A_{33} + 0.2862628UA_{13}A_{31} + 0.1029188A_{11}A_{13}A_{31} + 0A_{13}A_{31}A_{33} + 0UA_{13}A_{33} + 0A_{11}A_{13}A_{33} + 0.0399478UA_{31}A_{33} + 0.0501962A_{11}A_{13}A_{33} + 0Ua_0^2$$

$$K_3 = 0.0788884U^3 + 0.0229610UA_{11}^2 + 0.0025854A_{11}^3 - 0.0108586A_{13}A_{11}^2 + 0.0101780A_{31}A_{11}^2 - 0.0108677A_{33}A_{11}^2 + 0.1835371UA_{13}^2 + 0.0387298A_{11}A_{13}^2 + 0A_{13}^3 + 0.1617810A_{31}A_{13}^2 + 0A_{33}A_{13}^2 - 0.0001661UA_{31}^2 + 0.0002916A_{11}A_{31}^2 - 0.0007270A_{13}A_{31}^2 + 0.0000385A_{31}^3 - 0.0001291A_{33}A_{31}^2 + 0.0058676UA_{33}^2 + 0.0009858A_{11}A_{33}^2 + 0A_{13}A_{33}^2 - 0.0001042A_{31}A_{33}^2 + 0A_{33}^3 - 0.0539584UA_{11}A_{13} + 0.0052325UA_{11}A_{31} - 0.0097463UA_{11}A_{33} - 0.0114135UA_{13}A_{31} + 0.0479104A_{11}A_{13}A_{31} - 0.0005767A_{13}A_{31}A_{33} + 0.0654494UA_{13}A_{33} + 0.0113346A_{11}A_{13}A_{33} - 0.0028457UA_{31}A_{33} - 0.0010434A_{11}A_{31}A_{33} + 0Ua_0^2$$

$$K_4 = -0.1000001U^3 - 0.0276360UA_{11}^2 - 0.0017326A_{11}^3 + 0.0500488A_{13}A_{11}^2 - 0.0090943A_{31}A_{11}^2 + 0.0260358A_{33}A_{11}^2 + 0UA_{13}^2 + 0A_{11}A_{13}^2 + 0.2164743A_{13}^3 + 0A_{31}A_{13}^2 + 0.1892152A_{33}A_{13}^2 - 0.0003166UA_{31}^2 + 0.0002075A_{11}A_{31}^2 + 0.0020334A_{13}A_{31}^2 + 0.0000382A_{31}^3 + 0.0003830A_{33}A_{31}^2 + 0UA_{33}^2 + 0A_{11}A_{33}^2 + 0.0186546A_{13}A_{33}^2 + 0A_{31}A_{33}^2 + 0.0010804A_{33}^3 + 0.3104708UA_{11}A_{13} - 0.0081622UA_{11}A_{31} + 0.0497816UA_{11}A_{33} + 0.0484180UA_{13}A_{31} + 0.0184274A_{11}A_{13}A_{31} + 0A_{13}A_{31}A_{33} + 0UA_{13}A_{33} + 0A_{11}A_{13}A_{33} + 0.0073674UA_{31}A_{33} + 0.0031616A_{11}A_{31}A_{33} + 0Ua_0^2$$

The Gyroscopic Effects of a Rigid Rotating Propeller on Engine and Wing Vibration Modes

(*Continued from page 659*)

nates is advantageous for other problems. For example, the effect on aircraft stability in flight of the high-speed rotor of a jet engine can readily be treated. Whether these effects will be large or small has not been investigated by the present authors. Could gyroscopic moments be a partial cause of some "snaking" effect in jet aircraft observed while trying to hold them on course?

The application of the considerations of this paper to other spring-mounted, rotating machinery is also direct. It should be noted, in passing, that the rotor problem treated here is *not* the same as the well-known one of the gyroscopic effect on critical speeds of overhanging shafts, etc. In such problems, rotation and precession are usually locked together, while nutation is nonexistent.

References

[1] Klein, F., and Sommerfeld, A., *Theorie des Kreisels;* Teubner, Leipzig, 1910.

[2] Webster, A. G., *The Dynamics of Particles and of Rigid, Elastic, and Fluid Bodies*, 3rd Ed.; Hafner, N.Y. (Reprint, 1949).

[3] Slater, J. C., and Frank, N. H., *Mechanics;* McGraw-Hill Book Company, Inc., New York, 1947.

[4] Bennett, G. S., *Gyroscopic Effects in a Vibratory System*, Journal of Applied Physics, Vol. 18, December, 1947.

[5] Bisplinghoff, Isakson, Pian, Flomenhoft, and O'Brien, *An Investigation of Stresses in Aircraft Structures under Dynamic Loading*, M.I.T.-Navy Contract No. NOa(s) 8790, Report.

First U. S. National Congress of Applied Mechanics

Plans have now been formulated to hold the First U.S. National Congress of Applied Mechanics on June 11–16, 1951, at Chicago, Ill. The Illinois Institute of Technology will be host to the Congress.

Members of the Institute, one of the sponsoring societies, are cordially invited to submit papers, which should constitute original research in applied mechanics. (Their length must not exceed 5,000 words or the equivalent in equations, tables, and diagrams.) Abstracts must be submitted to the Chairman of the Editorial Committee before April 14, 1951; complete papers must be submitted prior to June 11, 1951.

Additional information about the Congress may be obtained by writing to N. M. Newmark, Secretary of the Congress, University of Illinois, Urbana, Ill. All members are invited to attend.

Readers' Forum

BRIEF REPORTS of investigations in the aeronautical sciences and discussions of papers published in the JOURNAL are presented in this special department. The publication will be completed approximately 8 weeks after receipt of the material. The Editorial Committee does not hold itself responsible for the opinions expressed by the correspondents. Contributions should not exceed 800 words in length

On Boundary-Layer Growth in a Compressible Flow Between Radial Walls

J. Conrad Crown
U.S. Naval Ordnance Laboratory, White Oak, Silver Spring, Md.
June 28, 1950

THE SOLUTION FOR the laminar flow field about a flat plate in a uniform stream is well known. However, it is also of interest to study other flows—e.g., ones in which streamwise pressure gradients are present. We shall consider here the compressible laminar radial flow between radial, two-dimensional walls[1] and through an axially symmetric conical nozzle. In particular, we shall concern ourselves with the displacement thickness of the boundary layer.

For two-dimensional steady flow, the equation of continuity in polar coordinates is

$$(\partial \rho u r/\partial r) + (\partial \rho v/\partial \theta) = 0$$

where u and v are the components of velocity in the directions r and θ, respectively, and ρ is the density.

If the flow is radial, $v \equiv 0$. Then

$$\rho u = f(\theta)/r$$

where $f(\theta)$ is so far undetermined except that it is a function only of θ, Reynolds Number, and wall divergence angle. Let $\theta = 0$ be the centerline of the flow and such quantities be designated with a subscript "1." Let $\theta = \pm\alpha$ be the boundary along which $u = 0$.

The displacement thickness is defined by

$$\delta^* = \int_0^\alpha \left(1 - \frac{\rho u}{\rho_1 u_1}\right) r \, d\theta$$

and for radial flow becomes

$$\delta^* = r \int_0^\alpha \{1 - [f(\theta)/f(0)]\} d\theta$$

Thus it can be seen that the boundary-layer displacement thickness grows linearly with the radius. The proportionality constant depends on the Reynolds Number and wall divergence angle. No restrictions have been imposed here on Mach Number.

Similarly, if we consider radial, axially symmetric flow through a pipe or nozzle, we find that the displacement thickness also grows linearly with the radius.

It is interesting to note that, in a supersonic nozzle (with radial walls), in spite of the favorable pressure gradient, the boundary layer grows faster than over a flat plate with no gradient. In this comparison it should be borne in mind that in the nozzle the displacement thickness is based on centerline flow characteristics that vary along the nozzle while that of the flat plate is referred to free-stream conditions that are constant.

REFERENCE

[1] Goldstein, Sidney, *Modern Developments in Fluid Dynamics*, Vol. 1, p. 105; Oxford, 1938.

On Virtual Mass and Wave Drag at Subsonic Speeds

John W. Miles
Associate Professor, Department of Engineering, University of California at Los Angeles
June 20, 1950

THE PROBLEM OF IMPULSIVE MOTION of a body in an ideal, incompressible fluid has been discussed by Lamb, Larmor, Kelvin, and others.[1] As might be expected from the concept of virtual mass,[2] an impulsive force is required to generate impulsive motion, insofar as the fluid is assumed to be incompressible. However, if the compressibility of the fluid is taken into account, the force required to generate impulsive motion may be expected to remain bounded and to vanish only asymptotically with time. Moreover, the concept of virtual mass, while still valid for the description of the energy and momentum of the fluid flow in the steady state, is of no direct aid in computing the transient response. In particular, we find that the work required to generate impulsive motion is not entirely recoverable, so that the process is irreversible, and some part of the starting force must be regarded as "wave drag." (Indeed, the present remarks were motivated by a brief discussion of just this question with Prof. Th. von Kármán, who raised the question of the validity of the virtual mass concept in a compressible fluid. Our thanks also are due to Prof. H. K. Forster, with whom we discussed the same question. Professor Forster pointed out the similarity between the present situation and the acceleration of an electron, with which is associated radiation.)

As a simple example, we consider certain aspects of the sudden acquisition of a velocity v by a body in an ideal, nearly incompressible fluid. First, after equilibrium is attained, the flow will be potential, and there will be no resultant force on the body. Second, if m is the virtual mass of the body in this potential flow, the final momentum of the associated flow will be mv, whence the total impulse required to impart the motion is given by

$$I = \int_0^\infty F(t)\, dt = mv \tag{1}$$

(Of course, if the fluid is truly incompressible, the time required is zero and the force infinite, but this indeterminacy does not affect the integrated results.) Third, since this force acts at a constant velocity, the total work done is given by

$$W = \int_0^\infty F(t) v \, dt = mv^2 \tag{2}$$

Fourth, the kinetic energy of the associated flow, after equilibrium has been established, is given by

$$\text{K.E.} = (1/2)mv^2 \tag{3}$$

It follows that an equal amount of energy $[(1/2)\, mv^2]$ has become unavailable during the period of transient motion. Moreover, if the body were to be stopped suddenly, the remaining $(1/2)mv^2$ also would be rendered unavailable. The agency of dissipation, in both cases, is radiation, and the associated force is appropriately designated as "wave drag," although this term generally is applied only to supersonic configurations.

We remark that a result somewhat analogous to the foregoing arises in the rather more transparent problem of a linear system of one degree of freedom. Thus, if an ideal capacitor is charged by a suddenly applied constant voltage source, the final energy stored in the capacitor is only half that delivered by the source,

even though there is no (ohmic) resistance in the circuit. In both cases, we have irreversibilities, albeit without *direct* degradation of energy.

In seeking an explicit solution to the foregoing problem, dimensional consideration leads us to write

$$F(t) = mv(c/l)f(ct/l) \tag{4}$$

where l is a characteristic length and (l/c) is a characteristic time, the characteristic velocity being chosen as the sonic velocity c. Similarly, if a constant force F is suddenly applied to a body, we write for the resulting acceleration

$$(d/dt)v(t) = (F/m)g(ct/l) \tag{5}$$

In the case of a circular cylinder of radius a, moving normal to its axis, we find on the basis of the acoustic approximation $(v/c \ll 1)$

$$f(x) = 1 - \frac{1}{2}x - \frac{1}{16}x^2 + \frac{5}{48}x^3 + 0(x^4) \tag{6a}$$

$$= -2x^{-3} - [62 - 24 \ln (2x)]x^{-5} + 0(x^{-7} \ln^2 x) \tag{6b}$$

$$g(x) = \delta(x) + \frac{1}{2} + \frac{3}{8}x + 0(x^2) \tag{7a}$$

$$= 1 - x^{-2} + [4.232 - 3 \ln (4x)]x^{-4} + 0(x^{-6} \ln^2 x) \tag{7b}$$

where $\delta(x)$ is the Dirac delta function, and the characteristic length is a. It is of particular interest that $f(x)$ changes sign. In connection with $g(x)$, we remark that the actual apparent mass is initially zero, jumps immediately to $2m$, decreases in accordance with $2m[1 - (3\tau/4)]$ and is asymptotic to m as $(1 + \tau^{-2})$, where $\tau = ct/a$. More detailed calculations are in progress but await the availability of certain tabulated integrals, to which we have been referred by Prof. A. Erdelyi.

If a constant force acts for time t_1 on a circular cylinder, we find that the work done for small and large values of τ_1 is given by

$$W = \frac{mv^2}{2}[2\tau_1^{-1} + \frac{1}{2} + \frac{1}{8}\tau_1 + 0(\tau_1^2)] \tag{8a}$$

$$= \frac{mv^2}{2}[1 + 2\tau_1^{-2} \ln (2\tau_1) + \tau_1^{-4} - 2\tau_1^{-4} \ln (4\tau_1) + 0(\tau_1^{-6} \ln^2 \tau_1)] \tag{8b}$$

where v is the *final* velocity. Hence, if a body is accelerated rapidly, the starting efficiency is vanishingly small; while, if it is accelerated slowly, the efficiency approaches unity.

References

[1] Lamb, H., *Hydrodynamics*, pp. 10, 11, 160–167; Dover Press, New York, 1945.

[2] Lamb, H., *loc. cit.*, pp. 77, 160–180.

Effect of Wing Parameters on Load Intensity in Wing Skin

B. E. Gatewood
Department of Mechanics, U.S.A.F. Institute of Technology, Wright-Patterson Air Force Base, Dayton, Ohio
June 19, 1950

The load intensity P_i (lbs. per in.) is extremely useful in preliminary wing design as a guide to the type of wing structure that should be used. At any wing section

$$P_i = M/hd \tag{1}$$

where M is maximum beam moment on the section, h is the average height of the structural section, and d is the length of the structural section. The equivalent skin thickness for the top or bottom surface of the wing is P_i divided by the allowable stress. Thus, in preliminary design, a large P_i indicates the possibility of using heavy skin without stringers, while a small P_i indicates thin skin with stringers. Naturally, the shear flow q_t (lbs. per in.) from the torque T, where

$$q_t = T/2hd \text{ (approx.)} \tag{2}$$

must be considered in conjunction with P_i.

Since in many cases in preliminary design the bending moment M in Eq. (1) is not known or requires considerable calculation to obtain, it is desirable to express M (and, hence, P_i) in terms of the wing parameters. This can be done without difficulty if the section lift coefficient is assumed constant and the wing dead weight section coefficient is assumed constant. The P_i thus obtained is sufficiently accurate for preliminary design. The formula for P_i is

$$P_i = \frac{nb\left(\frac{W}{S}\right)(\text{A.R.})(1+\lambda)[1-(2y/b)]^2[1+2\lambda-(1-\lambda)(2y/b)]}{576\left(\frac{t_s}{c}\right)\left(\frac{c_s}{c}\right)[1-(1-\lambda)(2y/b)]^2} \tag{3}$$

where

y = distance along semispan from fuselage centerline
b = structural span (ft.)
λ = taper ratio $= c_T/c_R$
c_T = tip chord
c_R = root chord

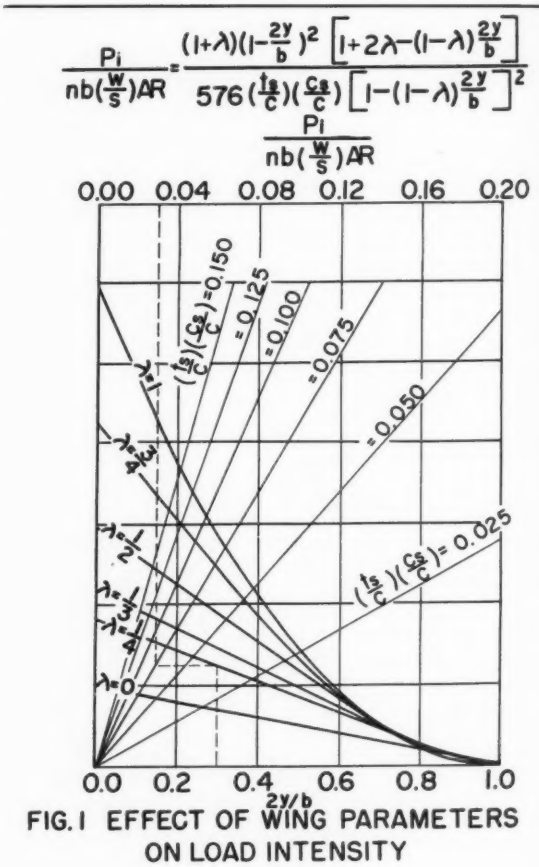

FIG. 1 EFFECT OF WING PARAMETERS ON LOAD INTENSITY

$$\frac{F_{ult.}\,W_{sw}}{nDb^3\left(\frac{W}{S}\right)} = \frac{1}{3\left(\frac{F_{all.}}{F_{ult.}}\right)\left(\frac{t_s}{c}\right)}\left[\frac{1-9\lambda^2+8\lambda^3-6\lambda^3\ln\lambda}{(1-\lambda)^3}\right]$$

$$\frac{F_{ult.}\,W_{sw}}{nDb^3\left(\frac{W}{S}\right)}$$

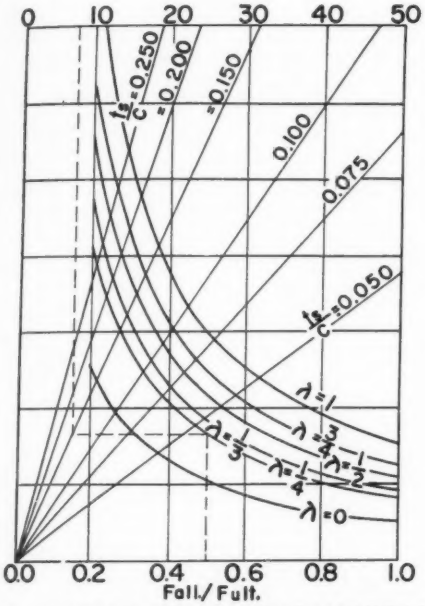

FIG.2 EFFECT OF WING PARAMETERS ON WING WEIGHT

W/S = wing loading (lbs. per sq.ft.)
A.R. = structural aspect ratio = b^2/S
n = effective wing load factor (correct airplane load factor for tail load and wing dead weight)
c = chord
t_s/c = effective structural thickness ratio
c_s/c = effective structural chord ratio
P_i = load intensity (lbs. per in.) on upper or lower surface of wing

Fig. 1 shows a nondimensional chart of $P_i/nb(W/S)$A.R. against $2y/b$ with λ and $t_s c_s/c^2$ as parameters.

Since the equivalent thickness of the structural upper or lower wing skins is $P_i/F_{all.}$, the weight S_{sw} of the structural part of the wing to take the loads P_i (i.e., the beam bending moments) can be expressed in terms of the wing parameters

$$W_{s_w} = 4D\int_0^{b/2}\frac{P_i}{F_{all.}}\,c_s\,dy \qquad (4)$$

where

P_i = P_i in Eq. (3)
c_s = structural chord
D = material density (lbs. per cu.in.)
$\frac{1}{F_{all.}} = \frac{1}{2}\left(\frac{1}{F_{all._u}} + \frac{1}{F_{all._c}}\right)$
$F_{all._u}$ = allowable stress (lbs. per sq.in.) in upper surface
$F_{all._c}$ = allowable stress (lbs. per sq.in.) in lower surface
W_{s_w} = structural weight of wing (lbs.)

The total wing weight will include another component for the nonstructural wing items, for the internal support structure (as ribs), and for any webs to take the shear and torque loads. Eq. (4) gives upon integration

$$W_{s_w} = \frac{nDb^3\left(\frac{W}{S}\right)}{3F_{all.}\left(\frac{t_s}{c}\right)}\,\frac{1-9\lambda^2+8\lambda^3-6\lambda^3\ln\lambda}{(1-\lambda)^3} \qquad (5)$$

Fig. 2 shows a nondimensional chart of $F_{ult.}W_{s_w}/nDb^3(W/S)$ against $F_{all.}/F_{ult.}$ with λ and t_s/c as parameters. Here, $F_{ult.}$ is the ultimate tensile stress of the material.

The Basic Theorems in the Plastic Theory of Structures

P. S. Symonds
Engineering Laboratory, Cambridge University, England (on leave from Brown University)
July 26, 1950

THE TWO THEOREMS DISCUSSED RECENTLY in the JOURNAL OF THE AERONAUTICAL SCIENCES by Neal[1] have been applied mainly to framed structures of mild steel whose members are assumed to exhibit the "limited strain hardening" characteristic, as it was termed by the author. Thus, the bending moment is assumed to be in the range between a "fully plastic moment" M_p for positive bending and a corresponding value M_p' for negative bending. At either of these values the entire cross section would be flowing plastically, with the material at the yield stress either in tension or compression. Based on this hypothesis the so-called "plastic methods" of analysis and design have been developed,[2-5] which have attractive features in their simplicity and deal directly with failure conditions of a structure. Thus, they eliminate some of the uncertainty in the choice of safety factor and make for greater economy in use of material.

Although most of the applications have been to steel structures, it should be possible to apply the plastic methods to frames composed of certain of the light alloys. The basic hypothesis that the bending moment cannot exceed a certain magnitude (in one sense or the other), at which large changes in curvature occur at constant moment, is not strictly valid but would seem to be accurate enough for some alloys to allow useful results to be obtained from the theory based on it. The differences in behavior between frames of steel and those of certain light alloys are probably matters of degree rather than of kind. The fact that the light alloys do not exhibit the flat yield characteristic of mild steel is not of major significance; the strain hardening at large strains which is neglected in the theory actually plays an important role in the behavior of steel frames[2] loaded to failure in the sense of the plastic theory. However, a number of problems must be investigated, such as those of stability and of possible failure by rupture, before the plastic methods can be accepted as fully valid for framed structures of light alloys.

The writer has been especially interested in problems in which a number of loads on a structure may be repeatedly applied in a more or less independent manner. The criterion of safety here is taken to be that the structure is capable of "shaking down" to some state (when loads are removed) with residual stresses and permanent strains such that the further application of any combination of loads in their prescribed ranges produces no additional plastic flow.

The basic theorem governing this type of problem proved by the author can be put in a different form, which greatly facilitates the numerical work in solving a particular problem and also clarifies its physical significance. The author showed that necessary and sufficient conditions for a structure to shake down are that

residual moments $\bar{m}_i$ and parameters M_i^* exist such that

$$\mathfrak{M}_i^{max.} + \bar{m}_i \leqslant M_i^* + (M_Y)_i \quad (1a)$$

$$\mathfrak{M}_i^{min.} + \bar{m}_i \geqslant M_i^* + (M_Y')_i \quad (1b)$$

$$M_i^* \leqslant (M_p)_i - (M_Y)_i \quad (1c)$$

$$M_i^* \geqslant (M_p')_i - (M_Y')_i \quad (1d)$$

In these inequalities the subscript i specifies the location of a typical cross section of the structure; $\mathfrak{M}_i^{max.}$ and $\mathfrak{M}_i^{min.}$ are the maximum and minimum bending moments at the ith section which the given set of loads could produce if the frame behaved wholly elastically; $(M_Y)_i$ and $(M_Y')_i$ are initial yield moments for positive or negative bending, respectively; and M_i^* is a parameter that depends on the previous straining history and is defined so that yield begins in positive bending when

$$M_i = M_i^* + (M_Y)_i$$

or in negative bending when

$$M_i = M_i^* + (M_Y')_i$$

A simpler form of the inequalities (1) can be obtained by eliminating the parameter M_i^* from them. Consider, for example, inequalities (1a) and (1b). These can be rearranged as follows:

$$\mathfrak{M}_i^{max.} + \bar{m}_i - (M_Y)_i \leqslant M_i^* \leqslant \mathfrak{M}_i^{min.} + m_i - (M_Y')_i \quad (2)$$

When written in this form it is obvious that these two inequalities can be satisfied if, and only if, the left-hand member of inequalities (2) does not exceed the right-hand member and, hence, if

$$\mathfrak{M}_i^{max.} - \mathfrak{M}_i^{min.} \leqslant (M_Y)_i - (M_Y')_i \quad (3)$$

Similar consideration of inequalities (1a) and (1c) leads to

$$\mathfrak{M}_i^{max.} + \bar{m}_i \leqslant (M_p)_i \quad (4a)$$

while consideration of inequalities (1b) and (1d) yields

$$\mathfrak{M}_i^{min.} + \bar{m}_i \geqslant (M_p')_i \quad (4b)$$

The only other pair of the original inequalities which can be combined in this manner are (1c) and (1d). These require the inequality

$$(M_Y)_i - (M_Y')_i \leqslant (M_p)_i - (M_p')_i$$

to be satisfied. This is automatic in view of the definitions, and, hence, this result is of no further interest.

Thus, the necessary and sufficient conditions for shake-down are seen to be the existence of residual moments satisfying the inequalities (4a) and (4b) and the satisfaction of inequalities (3), which depend only on the extreme values of the external loads and on the elastic moment range for each member. These systems of inequalities are simpler than the author's, and they can be used without difficulty in the numerical solution of specific problems.[5]

The physical interpretation of the new inequalities is of particular interest.

There are two different and independent phenomena of continuing plastic flow when shake-down does not occur.[5, 6] The first and most obvious is that in which plastic flow in some regions is made to occur alternately in one sense and in the other, as appropriate load cycles are applied. (This would be a severe type of fatigue loading condition.) The second type of continuing plastic flow is that in which definite amounts of plastic deformation recur *always in the same sense*, as certain load cycles are repeated. Thus, if a sufficient number of cycles were applied, deflections of arbitrarily large magnitude could be produced (under the hypotheses of the theory) without increasing the extreme values of the external loads. In practice, the unlimited growth of deflections is halted mainly by strain-hardening, but recent tests show that the theoretical critical load limits have very real physical significance.

These two distinct types of continuing plastic flow are governed, respectively, by the sets of inequalities (3), (4a), and (4b). Thus, if loads are such that inequalities (3) are not satisfied, then plastic flow alternating in sense can be made to continue indefinitely. On the other hand, if residual moments satisfying inequalities (4a) and (4b) (and the equilibrium equations) cannot be found, then deflections of large magnitude can be produced by sufficiently many repetitions of certain loading cycles.

References†

[1] Neal, B. G., *Plastic Collapse and Shake-Down Theorems for Structures of Strain-Hardening Material*, Journal of the Aeronautical Sciences, Vol. 17, No. 5, p. 297, May, 1950.

[2] Baker, J. F., *The Design of Steel Frames*, The Structural Engineer, Vol. 27, p. 397, October, 1949.

[3] Baker, J. F., and Heyman, J., *Tests on Miniature Portal Frames*, The Structural Engineer, Vol. 28, p. 139, June, 1950.

[4] Neal, B. G., and Symonds, P. S., *The Calculation of Collapse Loads for Framed Structures*, J. Instn. Civil Engrs., Vol. 35, 1950–1951 (in press).

[5] Symonds, P. S., and Neal, B. G., *The Calculation of Failure Loads on Plane Frames Under Arbitrary Loading Programs*, J. Instn. Civil Engrs., Vol. 35, 1950–1951 (in press).

[6] Horne, M. R., *The Effect of Variable Repeated Loads in the Plastic Theory of Structures*, Research Engineering Structures Supplement (Colston Papers, Vol. 2) p. 141, 1949.

† References 2–6 are cited as representative of papers published since the preparation of reference 1; they are by no means exhaustive.

Note on Plastic Column Behavior

George Gerard

Guggenheim School of Aeronautics, College of Engineering, New York University

July 3, 1950

Several discussions of the stability of a plastic column which have been concerned with a model of the stress distribution in the cross section at buckling have appeared in the recent literature. The most recent paper by Duberg and Wilder (Journal of the Aeronautical Sciences, Vol. 17, No. 6, pp. 323–327, June, 1950) attempts to go further by redefining the critical load for a plastic column "...based on the behavior of a slightly bent column as the initial lack of straightness vanishes." This new redefinition of the critical load appears to be a necessary consequence of accepting the tangent modulus stress distribution model as valid for the plastic perfect column.

The tangent modulus model requires that during buckling the load be permitted to *increase* simultaneously with bending. If this model were applied to the elastic perfect column, however, its stability limit could not be determined, since the commonly accepted definition of the critical load is the load at which an exchange of equilibrium configurations occurs with *no increase* in axial load. Thus, it appears necessary to examine critically column behavior in both the elastic and plastic range to determine whether plastic column behavior fits within the framework accepted for the elastic column or if a new definition is required.

It is the purpose of this note to indicate that both elastic and plastic column behavior fit within the same framework, permitting a consistent treatment of the column problem throughout the entire stress range.

Elastic Column

The stability problem of the perfect elastic column is characterized by the following features: It is an eigenvalue problem, the solution of which determines the point at which an exchange of stable equilibrium configurations occurs. The important detail to note is that the equilibrium change occurs at a fixed value of axial load. Since the solution is for one point only, the value of central deflection remains indeterminate.

The problem of the initially imperfect column is not one of stability at all, since only the initially bent form is stable. The value of central deflection is known for all values of load, and it is found that, in a region below the buckling load of the perfect elastic column, the central deflection of the imperfect column grows rapidly. To define the buckling load for the latter if it were a perfect column, the Southwell method may be used.

For an elastic column the postcritical behavior of the perfect and imperfect column is essentially the same in the region where bending predominates. In this region, the failing load of the imperfect column is little influenced by small initial imperfections and approximately coincides with the Euler load for the perfect column within close limits. Thus, the Euler Formula can be used to predict the failing load of the imperfect column for engineering purposes.

Plastic Column

The stability theory for the plastic column is considerably more complex than in the elastic case because it is necessary to postulate various models of stress distribution at the critical load to determine the bending stiffness in the plastic region. In particular, since the behavior in the region of the critical load vitally affects the failing load, which was not the case for the elastic column, the buckling model assumes great importance in the case of plastic buckling.

To solve the stability problem for the plastic column, the von Kármán strain reversal model must be considered valid, since it is the only one at which an exchange of equilibrium configurations occurs at the same value of load. This model results in a critical load that is consistent with the stability definition accepted for the elastic column.

For the imperfect column, which is not a stability problem, it appears reasonable to assume a model such as the tangent modulus model. It is to be noted that the tangent modulus model cannot be used for the stability problem, since this model requires an increase in load as bending becomes large. Thus, the conclusion is drawn that the strain reversal model is valid for the perfect column, whereas the tangent modulus model may be valid for the imperfect column. The critical load for an imperfect plastic column may be determined by use of the modified Southwell method as proposed by Wang.

To determine the failing load for a plastic column, it is necessary to construct a model of the failure mechanism. It appears reasonable to hypothesize that failure occurs when, or shortly after, the condition of strain reversal is reached. Thus, for the perfect plastic column, the buckling load and failing loads should coincide. The failing load of the imperfect column, however, is governed by the magnitude of the initial imperfections, since strain reversal occurs in a region where axial loading and bending proceed simultaneously. Thus, we can expect the failing load of the plastic imperfect column to vary within rather wide limits, depending upon the initial imperfection with the reduced modulus load as the upper limit for the case of vanishing imperfections.

Some Relations Between Harmonic and Transient Loading of Airfoils

John W. Miles
Associate Professor, Department of Engineering, University of California at Los Angeles
June 20, 1950

The well-known duality between the responses of a linear system to harmonic and step function excitations and the associated duality between the Fourier and Duhamel methods of superposition, respectively, can be used to establish some rather useful theorems relative to the transient loading of a thin airfoil. Let $f_{0,\,1,\,2}$ denote (operationally) the responses to the normal (at the airfoil) velocity distributions $w_{0,\,1,\,2}$ in accordance with

$$w_0(x, y) = \alpha(x, y) \rightarrow f_0\{\alpha(x, y)\} \tag{1}$$

$$w_1(x, y) = \alpha(x, y) \exp(ikt) \rightarrow f_1\{k, \alpha(x, y)\} \exp(ikt) \tag{2}$$

$$w_2(x, y) = \alpha(x, y)\mathbf{1}[t - t_0(x, y)] \rightarrow f_2\{t, t_0(x, y), \alpha(x, y)\}\mathbf{1}(t) \tag{3}$$

where t is a dimensionless time obtained by multiplying the true time by the quotient of a characteristic velocity and a characteristic length, k is a dimensionless frequency obtained by dividing the true (angular) frequency by this same quotient, (x, y) are coordinates in the plane of the airfoil, and t_0 is the time at which the normal velocity arises at (x, y). We assume t_0 to be positive, definite and bounded. Then, it follows directly from the aforementioned duality that

$$\lim_{t\rightarrow\infty} f_2\{t, t_0, \alpha\} = f_1\{0, \alpha\} = f_0\{\alpha\} \tag{4}$$

$$f_2\{0, t_0, \alpha\} = \lim_{k\rightarrow\infty} f_1\{k, \exp(-ikt_0)\alpha\} \tag{5}$$

In connection with Eq. (5), we remark that linearized theory is not reliable for large k, since terms of order $(kM\delta)^2$ are neglected, δ being the airfoil thickness parameter.[1]

$$\int_0^\infty f_2\{t, t_0, \alpha\}\, dt = \lim_{k\rightarrow 0} (ik)^{-1} f_1\{k, \exp(-ikt_0)\alpha\} \tag{6a}$$

$$\int_0^\infty [f_2\{t, t_0, \alpha\} - f_0\{\alpha\}]\, dt = \left[\frac{\partial}{\partial(ik)} f_1\{k, \alpha\}\right]_{k=0} - f_0\{t_0\alpha\} \tag{6b}$$

The integral in Eq. (6a) exists only if $f_0\{\alpha\} = 0$; otherwise, Eq. (6b) is to be used. In connection with Eq. (6), we remark that the time required to attain the steady state after a suddenly imposed disturbance is $M(M-1)^{-1}$ for a supersonic airfoil if the maximum chord is taken as the characteristic length.

Eq. (5) may be used to establish the initial lift coefficient (referred to the product of dynamic pressure and wing area) of an airfoil under transient loading as

$$(C_{L_0})_{t=0} = (4/M)\,\overline{(\alpha)}_{t_0=0} \tag{7}$$

where M is the free-stream Mach Number, and $\bar{\alpha}$ is the average value of α over that portion of the airfoil for which $t_0 = 0$. This is a generalization of a result obtained by Heaslet and Lomax[2] and is valid at both subsonic and supersonic speeds. Also, the initial lift acts through the centroid of the initial distribution of α.

A result that is useful in connection with Eq. (6) is[3]

$$\phi_1\{k, \alpha\} = \phi_0\{\alpha\} + ikM^2(M^2-1)^{-1} \times [\phi_0\{x\alpha\} - x\phi_0\{\alpha\}] + 0(k^2) \tag{8}$$

where ϕ is the velocity potential for an airfoil whose trailing edge is everywhere supersonic.

If the results of Eqs. (6) and (8) are applied to the penetration of a uniform, sharp-edged gust by a supersonic, rectangular airfoil of effective aspect A, we find

$$\overline{C_{L_1}} = \left[1 - \frac{1}{3}\left(\frac{M}{M+1}\right)\left(\frac{3A-2}{2A-1}\right)\right] C_{L_0} \tag{9}$$

$$C_{L_0} = 4(M^2-1)^{-1/2}\,[1 - (2A)^{-1}] \tag{10}$$

$$\overline{C_{M_1}} = \left(\frac{M}{M+1}\right)\left[\frac{6A^2 - 6A + 1}{9(M^2-1)^{1/2}A(2A-1)}\right] \tag{11}$$

$$A = (M^2-1)^{1/2}\,\text{A.R.} \geq 1 \tag{12}$$

where $\overline{C_{L_1}}$ and $\overline{C_{M_1}}$ are the average (incremental) lift and moment (with respect to the *final* center of pressure) coefficients over the transient period, C_{L_0} is the final lift coefficient (increment), and the chord is chosen as the characteristic length. Similarly, for a delta airfoil of apex angle 2γ entering a sharp-edged gust, we find

$$\overline{C_{L_2}} = \left\{1 - \left[\frac{(2M^2 + 1) - 2(f_1/f_0)}{3M(M + 1)}\right]\right\} C_{L_0} \tag{13}$$

$$C_{L_0} = 4(M^2 - 1)^{-1/2} f_0 \tag{14}$$

$$\overline{C_{M_2}} = \frac{(2M^2 + 1)f_0 - 2f_1}{9M(M + 1)\,(M^2 - 1)^{1/2}} \tag{15}$$

$$f_0 = \pi\sigma/2E'(\sigma), \quad \sigma \leq 1 \tag{16a}$$

$$\equiv 1, \quad \sigma \geq 1 \tag{16b}$$

$$f_1 = (3\pi/4)\,\sigma(1 - \sigma^2)[(1 - 2\sigma^2)E'(\sigma) + \sigma^2 K'(\sigma)]^{-1}, \quad \sigma \leq 1 \tag{17a}$$

$$\equiv 1, \quad \sigma \geq 1 \tag{17b}$$

$$\sigma = (M^2 - 1)^{1/2} \tan \gamma \tag{18}$$

where $K'(\sigma)$ and $E'(\sigma)$ are *complementary*, complete, elliptic integrals of the first and second kinds, respectively.

Similar results may be established concerning the response of an airfoil to an impulsive (delta function) gust, since this response may be represented as the time derivative of the response to a uniform, sharp-edged gust.

All of the foregoing results are, of course, subject to the usual restrictions imposed in the linearization of the hydrodynamical equations.[1]

References

[1] Lin, C. C., Reissner, E., and Tsien, H. S., *On Two-Dimensional Non-Steady Motion of a Slender Body in a Compressible Fluid*, J. Ma. and Ph., Vol. 27, pp. 220–231, 1948.

[2] Heaslit, M. A., and Lomax, H., *Two-Dimensional Unsteady Lift Problems in Supersonic Flight*, N.A.C.A. T.N. No. 1621, 1948.

[3] Miles, John W., *On Harmonic Motion at Supersonic Speeds*, Readers' Forum, Journal of the Aeronautical Sciences, Vol. 16, No. 6, pp. 378-379, June, 1949.

The Quasi-Steady Air Forces for Use in Low-Frequency Stability Calculations

(*Continued from page 608*)

The Laplace transform for $F(\tau)$ is readily shown to be, using the notation of Carslaw and Jaeger,[15]

$$\bar{F}(p) = \kappa(p) + j\lambda \frac{\kappa(p)}{p - j\lambda} = \frac{p\kappa(p)}{p - j\lambda} \tag{A4}$$

The *steady-state* air forces, which proceed according to $e^{j\lambda\tau}$, are evidently given by the portion of the inverse transform of $\bar{F}(p)$ which corresponds to the pole $p = j\lambda$—i.e.,

$$F_s(\tau, \lambda) = j\lambda[\kappa(j\lambda)]e^{j\lambda\tau} \tag{A5}$$

Eq. (A5) obviously holds equally well for both real and complex values of the parameter λ and thus leads to the desired conclusion: *The circulatory steady-state air forces for nonharmonic motions of the kind contemplated here can be derived simply by replacing the parameter k by λ in the expressions for the harmonic air forces.*

Regarding the noncirculatory air forces, it can be shown without difficulty that the previous conclusion continues to hold in these cases as well.

It is to be noted that a stability study based on the steady-state air forces, which is the conventional approach to the problem, does not necessarily describe the stability of the system immediately after a disturbance during the period when aerodynamic starting transients are still effective. The starting transients, which are defined by the remaining poles in Eq. (A5), are all heavily damped aperiodic forces; hence, their presence will only affect the stability of aircraft with heavily damped stability modes, in cases where the stability motions die away in times commensurate with the decay times of the transients. The heavy mode damping required for this situation to exist causes the question to be of academic interest only, and the use of the steady-state air forces alone for stability analyses is thus justified.
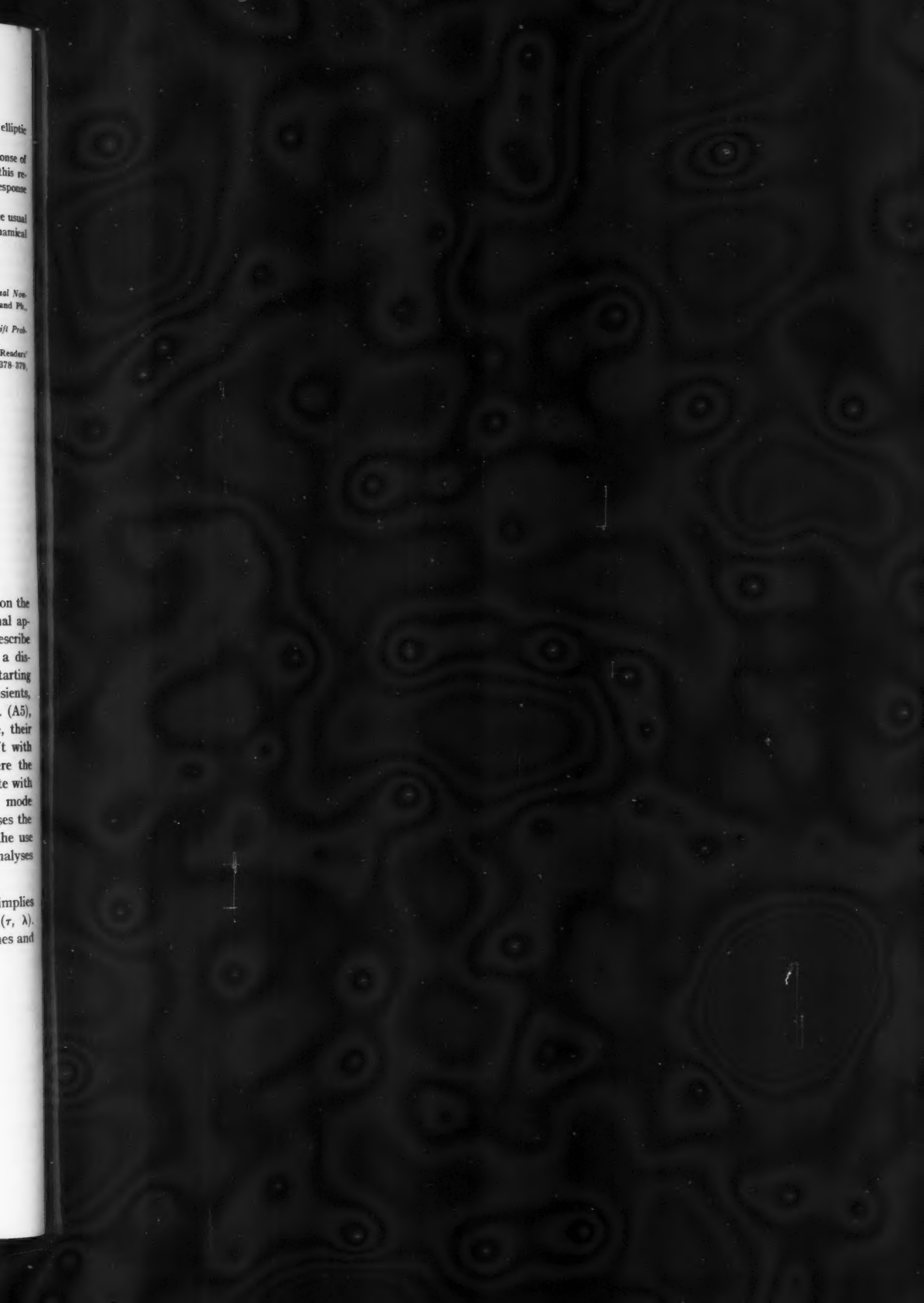
It is of further interest to note that Eq. (A5) implies a transform relationship between $\kappa(\tau)$ and $F_s(\tau, \lambda)$. This matter has been fully explored by R. T. Jones and W. R. Sears, as well as other investigators.